Tempering of martensitic steel for fasteners

Effects of micro-alloying on microstructure and mechanical property evolution

Proefschrift

ter verkrijging van de graad van doctor
aan de Technische Universiteit Delft,
op gezag van de Rector Magnificus prof. ir. K.C.A.M. Luyben;
voorzitter van het College voor Promoties,
in het openbaar te verdedigen op
vrijdag 18 september, 2015 om 12:30 uur

Door

Carin Emmy Ingrid Christersdotter ÖHLUND
Master of Science in chemical engineering with engineering physics,
Chalmers University of Technology
geboren te Alnö, Sweden

This dissertation has been approved by the

promotor: Prof. dr. ir. J. Sietsma and
copromotor: Dr. ir. S.E. Offerman

Composition of the doctoral committee:

Rector Magnificus
Prof. Prof. dr. ir. J. Sietsma promotor
Dr. ir. S.E. Offerman copromotor

Independent members:

Prof. dr. ir. L.A.I. Kestens	MSE, TU Delft
Prof. dr. T. Ohmura	Nat. Inst. For Materials Science
Prof. dr. ir. R. H. Petrov	University of Gent
Prof. dr. J. Ågren	Kungliga Tekniska Högskolan
Dr. ir. P.J. van der Wolk	Tata Steel

The research described in this thesis was performed in the department of Materials Science and Engineering, of the Delft University of Technology, Delft, the Netherlands. This research was fully funded by Koninklijke Nedschroef Holding B.V.

ISBN/EAN: 978-94-6186-519-9

To my parents,
who raised me to believe that
I can become anything I want

Table of Contents

List of abbreviations

A is a constant used in the generalized creep model
A_N is a constant used for dislocation creep
A_p is the projected contact area for nano-indentation
A_i is the interface area of the i^{th} interface
a is the interatomic distance
b is the Burgers vector
C_i is the concentration of element i
D is the diffusivity
D_0 is the pre-exponential factor for diffusivity
D_L is lattice diffusivity
D_P is pipe diffusivity in dislocations
$d_g$is the grain size
d_p is the diameter of a precipitate
E_i is the Young's modulus for material or component i
F is load
F_i is the force in component i
F_f friction force between the clamped parts
f is the volume fraction of precipitate phase
G is the shear modulus
ΔG_V is the formation energy of vacancies
ΔG^* is the activation energy for nucleation
g is the cross sectional area of dislocation pipe per unit area of matrix
Δg_s is the misfit strain energy
Δg_d is the change in free energy related to defects in the parent phase, which are annihilated during the nucleation of the phase β
Δg_v is the driving force for nucleation
h is the indentation depth during nano-indentation
h_c is the contact depth during nano-indentation
k_B is Boltzmanns constant
k_i is the spring constant/stiffness of component i
k_D is the Hall-Petch term
K_i is a proportionality constant for the i^{th} element in solid solution
K_s is the solubility product
k' is a constant that depends on the geometry of the indenter for nano-indentation
L is the distance between pinning points in the lattice
L_c, is the clamp length of a bolted joint
Δl_{bolt} is the elongation of the bolt

Δl_{base} is the compression of the clamped parts
M is the Taylor factor
N is the density of potential nucleation sites
N_j is the number of atoms that are within one atomic jump distance to the nuclei
n is an exponent of stress
n_a is the number of atoms in the nucleus
n_a^* is the number of atoms in the critical nucleus
n_s is an exponent used for solid solution strengthening
P_{max} is the maximum applied load during nano-indentation
p is an exponent used for grain size dependence of creep
Q_C is the activation energy for the creep
Q_D is the activation energy for diffusion
R is the universal gas constant
R_n is the radius of a growing precipitate
R_m is the ultimate tensile strength
$R_{p0,2}$ is the yield strength
r_c is the capture radius of a dislocation
r_p is the radius of a precipitate
S is the contact stiffness of nano-indentation
$S*$ is the surface of the nuclei
T is the temperature
T_m is the melting temperature
t is the time
t_s is the moment of nucleation
U_a is the activation energy for recovery
V_a is the and activation volume for recovery
V_β is the volume of the new phase β
$\Delta\mathbb{v}$ is the volume difference between matrix and solute atoms
X_V^e is the mole fraction of vacancies
Z is the non-equilibrium Zeldovich factor
Z_s is the settlement in the bolted joint
α is an empirical parameter
α_j is the number of atoms that are within one atomic jump distance to the nuclei
β^* is the frequency factor
γ_i is the area and energy of the i^{th} interface
ε is strain
$\dot{\varepsilon}$ is strain rate
ρ is the dislocation density
σ_C is the characteristic stress during nano-indentation

σ_l is the lattice friction

σ_{ss} is solid solution strengthening

σ_{gb} is grain boundary strengthening

σ_d is dislocation strengthening

σ_p is precipitation strengthening

τ is the incubation time

v is the growth rate of spherical precipitates

ν_d is Debye frequency

Φ is the stiffness relationship between the bolt and the base material

Γ is the atomic jump frequency

Summary

The research presented in this thesis aims to deepen our understanding of the effect of micro-alloying on the microstructure and mechanical property evolution during tempering of martensitic steel for fasteners. The ongoing trend of engine down-sizing has led to the need for stronger and more temperature resistant fasteners than currently available according to international standards. A new martensitic fastener steel called KNDS4 has been developed, that combines higher strength with improved resistance to hydrogen embrittlement. The higher strength is the result of the addition of small amounts of alloying elements such as Ti, V and Mo that can form alloy carbides. The improved resistance to hydrogen embrittlement is ascribed to the presence of nano-sized alloy carbides. However, in addition to enhancing strength and resistance to hydrogen embrittlement, alloy carbides are also able to improve the creep resistance of steels via pinning of dislocations at elevated temperature. It might therefore be possible to use the new fastener steel at higher service temperatures than the current high-strength fasteners. In order to optimize the properties of the new fastener steel, a fundamental understanding is needed of the relationship between the evolution of the microstructure and the hardness/strength during heat treatment. The research questions of the research are: (i) To which extent do different hardening mechanisms contribute to the strength of martensitic fastener steels? (ii) How do the different hardening mechanisms evolve as a function of time during annealing? (iii) What are the effects of a strong carbide forming element such as titanium on the microstructure and hardening mechanisms of martensitic fastener steel? (iv) Can the strength and temperature resistance of a martensitic fastener steel be improved by addition of carbide forming elements?

The initial part of the research is based on a model alloy without the presence of any carbide forming elements that is compared to a model alloy with only one carbide forming element, Ti, in order to study the influence of a single alloy carbide on the microstructure and properties. Thereafter, industrial fastener steels, with multiple carbide forming elements, are studied, where complex alloy carbides form.

Chapter 2 describes the industrial context that lead to the research described in this PhD-thesis. This background chapter consist of three main sections.

Section 2.1 gives an introduction on bolted joints in the automotive industry. The bolted joint is defined as the system consisting of the bolt itself, and the components that are held together by the bolt. The purpose of the bolt, to keep the assembled components together by compression via a clamp force, is discussed and the distribution of external forces into the bolted joint is reviewed for different load cases. The influence of settlement (loss of clamping force due to localized plastic deformation in the joint after assembly) is reviewed and the fatigue properties of the bolt in a bolted joint are briefly discussed, in terms of distribution of an alternating external load into the bolted joint. The chapter ends with a

review of the key mechanical properties of engine fasteners and an explanation of how current fastener steels are chosen.

Section 2.2 introduces the concept of strength and hardness and temperature resistance of metals. The theory of dislocations and dislocation movement is briefly explained and the mechanisms behind different types of dislocation movements are presented. The link between dislocation movement and strength of metals is explained and the different microstructure components that contribute to the total strength and hardness of a metal are reviewed. Equations for quantification of the strengthening mechanisms are presented and literature values related to steel are given. The (nearly) instantaneous and time-dependent (creep) effects of an external load at elevated temperature on the strength and deformation of steel are described. Creep is the time-dependent and permanent deformation of a metal under constant external loading. The mechanical behavior during the different stages of creep is discussed and the microstructural mechanisms behind creep are reviewed. Expressions for different mechanisms of creep are given. Section 2.2 ends with a review of different methods to measure creep, with special focus on the indentation creep method, since this method was used for the research of this Ph.D. study.

Section 2.3 presents martensite formation and precipitation-strengthening of martensite. The Fe-C phase diagram and the theory of martensite formation, according to the Bain theory, is discussed. The crystallography of lath martensite is presented and related to the strength via the hardening mechanisms presented in section 2.2. The evolution of the microstructure which takes place during tempering of martensite is summarized. Nucleation of precipitates, according to the classical nucleation theory, is presented and the energy terms which influence the nucleation of new phases are reviewed. The mechanisms of diffusion- and interface-controlled growth are presented. The Zener or diffusional growth is reviewed in more detail. Section 2.3 ends with a summary of the characteristics of TiC precipitates and the kinetic data related to the nucleation and growth of TiC in steel, since this precipitate type is specifically studied in the thesis.

Chapter 3 is an experimental study of the evolution of the hardness and microstructure in Fe-C-Mn martensite (that is free of alloy carbides) during isothermal annealing at 300°C. The hardness near martensite block boundaries is significantly higher than the hardness inside the block matrix, due to a higher dislocation density in the regions adjacent to the block boundaries (called boundary regions). The boundary regions soften with increasing tempering time, whereas the nano-hardness of the tempered matrix remains approximately constant with increasing tempering time. The softening kinetics of Fe-C-Mn martensite can be described by three stages, which are related to the evolution of the microstructure: Stage I (0-5 min) is characterized by fast macroscopic softening kinetics that is strongly related to: (a) fast and simultaneous softening and reduction in area fraction of boundaries regions (b) fast reduction in area fraction of non-tempered matrix regions. Stage II (5-10 min) is characterized by slow macroscopic softening kinetics that is related to slow softening and reduction in area fraction of the boundaries regions. Stage III (10-60 min) is characterized by very slow softening kinetics that is related to very slow softening and reduction in area fraction of boundary regions.

Chapter 4 is an experimental study of the influence of the addition of 0.042wt% Ti on the evolution of the microstructure and hardness of Fe-C-Mn steel during isothermal annealing at 300°C and at 550°C. The macroscopic hardness of Ti-containing and Ti-free Fe-C-Mn steel reduces rapidly during the first 5 minutes of tempering, due to (i) the redistribution of interstitially dissolved carbon into cementite and (ii) rapid recovery. The macroscopic hardness thereafter remains stable during continued annealing for the Ti-free steel, but the Ti-containing steel increases in hardness after 30 minutes of annealing at 550°C. The hardness increase of Ti-containing Fe-C-Mn-Ti steel is related to the formation of TiC-precipitates at 550°C. Nucleation of TiC-precipitates starts in the regions close to the martensite block boundaries (between 5-10 minutes) and subsequently nucleates in the block matrix (between 10-30 minutes) due to the higher dislocation density in the regions close to the block boundaries. The formation of TiC-precipitates slows down the recovery in the regions close to the martensite block boundaries, especially between 5 and 10 minutes of annealing. The growth of TiC-precipitates in martensite is simulated in good agreement with experimental observations with a model that takes capillarity effects, the overlap of the titanium diffusion fields and the effects of pipe diffusion of titanium atoms into account.

Chapter 5 is a computational study on the evolution of the hardening mechanisms in Fe-C-Mn-Ti steel during isothermal annealing. The hardness of martensite is simulated as a linear addition of multiple strengthening mechanisms. This hardness model is combined with a microstructural model based on the Kampmann-Wagner-Numerical (KWN) approach for a multi-component and multi-phase system to simulate the nucleation and growth of TiC-precipitates. The model is fitted to experimental results and used to simulate the hardness contribution of different microstructure components as a function of annealing time. The two microstructural components which contribute most to the overall hardness of the investigated Fe-C-Mn-Ti steel are Fe_3C precipitates (88 HV) and dislocations (54 HV) on a total of 284 HV. Both contributions decrease rapidly during the initial stages of annealing and stabilise after 10 minutes of annealing. The addition of titanium to the steel gives a minor hardness contribution via Ti-atoms in solid solution and TiC precipitates. Ti atoms in solid solution give a hardness contribution which increases slightly during the first few minutes of annealing and then remains stable (at 25 HV). The direct contribution of TiC precipitates to the overall hardness is limited (3.5 HV). However, TiC-precipitates also contribute to the overall hardness by pinning of dislocations during the recovery that takes place during the tempering. The model predicts that only a small volume fraction of TiC-precipitates forms during isothermal annealing at 550°C due to the large misfit strain (1.34 GJ/m^3) and the low density of potential nucleation sites.

Chapter 6 presents a comparative study of the evolution of mechanical properties at elevated temperature and the underlying microstructural mechanisms of ultra-high-strength and conventional high-strength steels for fasteners. The mechanical properties of the ultrahigh-strength steel KNDS4 of fastener grade 14.9 (strength 1400 MPa, yield-to-strength ration 0.9) and of conventional, high-strength steels 34Cr4 of fastener grade 12.9 (strength 1200 MPa, yield-to-tensile-strength ration 0.9) and 33B2 of grade 10.9 (strength 1000 MPa, yield-to-tensile-tensile-strength ration 0.9) are measured at room temperature and at elevated temperature. The alloy carbides in the steels are examined in order to investigate the underlying microstructural mechanisms that give rise to the different properties of the three fastener steels. KNDS4 steel has a higher yield strength ratio than both conventional high strength steels at 500°C, which have similar yield strength ratios at 500°C. Increasing the soaking time from 5 seconds up to 100 hours at elevated temperatures does not have an impact on the yield strength ratio. The nano-indentation creep rate shows a weak trend in which the tendency for deformation during constant load nano-indentation is lower in KNDS4 than in the 34Cr4 and 33B2 steels. This is measured both at similar indent depths and at the same indent time. The improved mechanical properties of the KNDS4 steel compared to the conventional high-strength steels are related alloy carbides in the microstructure that hinder dislocation movement. The alloy carbides in KNDS4 are smaller than the alloy carbides in 34Cr4 steel, and the properties are therefore better. Changing the standard industrial heat-treatment from an austenitization temperature of 940 to 1350°C can increase the hardness of KNDS4 by 8%. The increase stems from more effective dissolution of mainly Ti during the austenitization treatment. Titanium in solid solution enables nucleation and growth of precipitates, which generates precipitation strengthening during subsequent tempering. However, the standard industrial heat treatment results in a smaller martensite block size, which might be more beneficial for the toughness of the steel.

The study of martensitic model alloys showed that the martensite block structure remain stable at temperatures up to 550°C, whereas the redistribution of alloying elements such as carbon is rapid and cannot be prevented. The study of the model alloys furthermore confirmed that addition of a strong carbide forming element, such as Ti, results in nucleation of a fine dispersion of alloy carbides that prevents recovery and thereby adds both precipitation strengthening and dislocation strengthening to the steel. Our study of the industrial fastener steels thereafter confirmed that alloy carbides in martensite increases the temperature resistance of the steel, by maintaining a high yield strength at elevated temperatures. The study of the industrial steels furthermore showed that the tendency to material creep at room temperatures is reduced in steels with alloy carbide precipitates.

Development of more temperature resistant high strength steels for fasteners shall therefore be based on the strengthening mechanisms of grain boundaries and on alloy carbide precipitates. Our research furthermore showed that there is a need for further studies of traditional, axial creep testing, to fully understand and evaluate the beneficial effects of alloy carbides in martensitic steels.

For the application of the existing KNDS4 steel we find that, independent of the heat treatment, the mechanical performance of KNDS4 fasteners at elevated temperature and the low nano-indentation creep rates are two strong indicators that fasteners made from KNDS4 steel might be used at higher service temperatures than traditional high strength fasteners, due to the presence of small alloy carbides in the microstructure of KNDS4. Higher strength of a fastener steel enables development of smaller, but stronger fasteners. These fasteners can be used in critical applications inside the engine, to down-size e.g. connecting rods, which will make it possible to significantly reduce the size and weight of modern combustion engines. Furthermore, the improved temperature resistance of new martensitic fastener steels will allow using the fastener at elevated service temperatures. These fasteners can therefore be used in applications where the temperature exceeds the recommended service temperature of 150°C (with the maximum upper boundary of 300°C) as stated in ISO898-1. This make is possible to reduce the use of highly alloyed high temperature fasteners (which are designed for service temperatures of 500°C or more) that are used in engines today due to the lack of cost efficient, resource-efficient, micro-alloyed fastener steels suitable for service at 300-500°C.

Samenvatting

Het onderzoek in dit proefschrift is er op gericht om onze kennis te verdiepen over het effect van kleine hoeveelheden legeringselement op de ontwikkeling van de microstructuur en de mechanische eigenschappen tijdens het ontlaten van martensitisch staal dat wordt gebruikt voor de productie van schroeven voor de automobielindustrie. De aanhoudende trend van het verkleinen van de motor van auto's heeft geleid tot de vraag naar sterkere en meer temperatuurbestendige schroeven dan momenteel beschikbaar zijn volgens de internationale normen. Hiervoor is een nieuw martensitisch staal ontwikkeld dat KNDS4 wordt genoemd. Dit staal combineert een hogere treksterkte met een verbeterde weerstand tegen waterstofbrosheid, door toevoeging van carbidevormende elementen zoals Ti, V, Cr en Mo. Behalve voor een hogere treksterkte en een verbeterde weerstand tegen waterstofbrosheid, kunnen deze carbiden, door het (tijdelijk) vasthouden van dislocaties bij verhoogde temperatuur, ook de kruipweerstand van stalen verbeteren. Daarom is het wellicht mogelijk om dit nieuwe staal bij hogere temperaturen te gebruiken dan wat mogelijk is met de huidige staalsoorten die gebruikt worden voor hogesterkte verbindingselementen. Om de eigenschappen van de nieuwe staalsoort te optimaliseren, is een fundamenteel begrip van het verband tussen de veranderingen van de microstructuur en het verloop van de hardheid/treksterkte tijdens de warmtebehandeling nodig. De onderzoeksvragen behorende bij dit proefschriftzijn: (i) in welke mate verschillende microstructurele mechanismen bijdragen aan de sterkte van martensitische staalsoorten voor bouten? (ii) Hoe evolueren de verschillende verstevigingsmechanismen tijdens het ontlaten van het staal? (iii) Wat zijn de effecten van een sterk carbide-vormend element, zoals titanium, op de microstructuur en verstevigingsmechanismen van martensitische staal? (iv) Kan de sterkte en temperatuurbestendigheid van een martensitische staal voor bouten worden verbeterd door toevoeging van carbidevormende elementen?

De eerste stap in dit onderzoek is het bestuderen van een modellegering zonder enige carbidevormende elementen, die vervolgens vergeleken wordt met een modellegering met slechts één carbidevormend element: Ti. Hiermee wordt de invloed van één enkel type carbide op de ontwikkeling van de microstructuur en de eigenschappen bestudeerd tijdens het ontlaten van martensitisch staal. Daarna worden voor bevestigingselementen gebruikte industriële staalsoorten met meerdere carbidevormende elementen, waaronder complexe carbiden, onderzocht.

Hoofdstuk 2 geeft een samenvatting van de industriële context waaruit dit PhD onderzoek is ontstaan. Dit hoofdstuk bestaat uit drie secties. Sectie 2.1 geeft een inleiding op boutverbindingen in de automobielindustrie. Een boutverbinding wordt gedefinieerd als het systeem van een bout en de onderdelen die erdoor bijeen worden gehouden. Het doel van de bout bestaat uit het samenhouden van geassembleerde componenten middels een klemkracht. De invloed van externe krachten op de boutverbinding voor verschillende belastingen, de invloed van het zetgedrag van de verbinding (dit is het verlies van klemkracht als gevolg van lokale plastische vervormingen in de contactoppervlakken van de boutverbinding na de montage) en de invloed van een wisselende externe belasting op het vermoeiingsgedrag van de bout in een geassembleerde boutverbinding worden besproken. Het hoofdstuk eindigt met een overzicht van de belangrijkste mechanische eigenschappen van verbindingselementen die in de motor worden gebruikt en een uitleg hoe de huidige staalsoorten voor verbindingselementen zijn gekozen.

Sectie 2.2 introduceert het concept van sterkte en temperatuurbestendigheid van metalen. De theorie van dislocaties en dislocatiebeweging wordt kort uitgelegd en de mechanismen achter verschillende soorten dislocatiebewegingen worden geëvalueerd. De relatie tussen dislocatiebeweging en de sterkte van metalen wordt toegelicht. De verschillende microstructuurcomponenten die bijdragen aan de sterkte van een metaal wordt uitgelegd. Wiskundige vergelijkingen voor het kwantificeren van de verstevigingsmechanismen in metalen worden gepresenteerd en literatuurwaarden voor verschillende staalsoorten worden gegeven. De momentane en de tijdafhankelijke invloed van een temperatuurverhoging op de verschillende microstructuren wordt onderzocht. Vervolgens komt kruip van metalen aan bod. Kruip is de tijdafhankelijke plastische vervorming van een metaal onder een externe belasting. Het mechanische gedrag van de verschillende stadia van kruip en de microstructurele mechanismen achter kruip worden besproken. Ook worden er vergelijkingen voor verschillende mechanismen van kruip gegeven. Sectie 2.2 eindigt met een overzicht van verschillende methoden om kruip te meten, met speciale aandacht voor de methode om kruip middels een nano-indrukking te meten aangezien deze methode gebruikt wordt in het onderzoek van dit proefschrift.

Sectie 2.3 presenteert de versterking van martensiet middels precipitaten. Het Fe-C-diagram en theorieën met betrekking tot martensietvorming - waaronder die van Bain - worden besproken. De kristallografie van lath martensiet is onderzocht en gekoppeld aan de verstevigingsmechanismen van sectie 2.2. Daarnaast is een samenvatting toegevoegd met de microstructuurprocessen die plaatsvinden tijdens het ontlaten van het martensiet. De kinetische theorie achter vaste-stof nucleatie en groei van legeringscarbiden wordt uitgelegd. Nucleatie volgens de klassieke nucleatietheorie en de energetische factoren die de nucleatie van nieuwe fasen beïnvloeden worden besproken. De groeimechanismen achter diffusie- en grensvlakgecontroleerde groei, worden gepresenteerd. Zener-groei wordt in meer detail uitgelegd. Het hoofdstuk eindigt met een samenvatting van de kenmerken van TiC-precipitaten, de thermodynamische gegevens achter nucleatie en de groei van TiC in staal, omdat dit type precipitaten specifiek in dit proefschrift worden bestudeerd.

Hoofdstuk 3 is een experimentele studie naar het verloop van de hardheid en de microstructuur in Fe-C-Mn martensiet (deze is vrij van legeringscarbiden) tijdens het ontlaten op 300°C. De hardheid van het grensvlak tussen de martensiet blokken is aanzienlijk hoger dan de hardheid in de kern van het blok, als gevolg van een hogere dislocatiedichtheid rondom het grensvlak tussen de martensietblokken (deze regio’s worden blokgrensvlak-regio’s genoemd). Tijdens het ontlaten wordt de hardheid rondom het grensvlak tussen de blokken meer gereduceerd dan in de kern van het blok. De kinetiek van het ontlaten van Fe-C-Mn martensiet kan worden beschreven door drie stadia waarin de microstructuur verandert. Deze stadia/fasen zijn: Fase I (0-5 min) wordt gekenmerkt door een snelle macroscopische hardheidsverlagende kinetiek, die sterk gerelateerd is aan (a) snel en gelijktijdig verlagen van de hardheid en vermindering van het aandeel van blokgrensvlak-regio'st en (b) snelle vermindering van het aandeel gebieden dat niet is ontlaten in de kern van het martensiet blok. Fase II (5-10 minuten) wordt gekenmerkt door een trage macroscopische hardheidsverlagende kinetiek, die wordt bepaald door een langzame hardheidsverlaging en een vermindering van het aandeel van blokgrensvlak-regio's. Fase III (10-60 minuten) wordt gekenmerkt door een zeer trage hardheidsverlagende kinetiek, bepaald door een zeer langzame hardheidsverlaging van en een vermindering van de blokgrensvlak-regio's.

Hoofdstuk 4 is een experimentele studie naar de invloed van een toevoeging van 0.042wt% Ti op het verloop van de microstructuur en de hardheid van Fe-C-Mn staal tijdens het ontlaten op 300°C en 550°C. De macroscopische hardheid van Ti-houdend en Ti-vrij staal vermindert snel tijdens de eerste 5 minuten van het ontlaten als gevolg van (i) herverdeling van interstitieel opgelost koolstof tot de vorming van cementiet en (ii) snel herstel. De macroscopische hardheid van Ti-vrij staal blijft daarna stabiel tijdens aanhoudend ontlaten. In tegenstelling hiertoe toont Ti-houdend staal een hardheidsstijging na 30 minuten ontlaten bij 550°C. De verhoging van de hardheid van Ti-houdend Fe-C-Mn-Ti staal is gerelateerd aan de vorming van TiC-precipitaten bij 550°C. Nucleatie van TiC-precipitaten begint dicht bij het blokgrensvlak (na 5-10 minuten) en vervolgens in de kern van het blok (na 10-30 minuten). De oorzaak hiervan is de hogere dislocatiedichtheid dicht bij het blokgrensvlak. De vorming van TiC-precipitaten vertraagt het herstel dicht bij het blokgrensvlak na 5 tot 10 minuten ontlaten. Het is mogelijk om de groei van TiC-precipitaten in martensiet te simuleren met behulp van een model dat rekening houdt met capillaire werking, het overlappen van de titaan-diffusievelden en de effecten van pijpdiffusie van titaanatomen.

Hoofdstuk 5 is een theoretische studie naar het verloop van de verschillende versterkingsmechanismen in Fe-C-Mn-Ti staal tijdens isotherm ontlaten. De hardheid van martensiet wordt gesimuleerd als een lineaire superpositie van meerdere versterkingsmechanismen. Dit hardheidsmodel wordt gecombineerd met een microstructureel model, gebaseerd op een Kampmann-Wagner-Numerical (KWN) model, om de nucleatie en groei van TiC-precipitaten binnen een multi-component en multi-fase systeem te simuleren. Het model is wordt gevoed met experimentele resultaten en gebruikt de hardheidsbijdrage van de verschillende microstructurele componenten om de ontlaattijd te simuleren. De twee microstructurele componenten die het meest tot de totale hardheid van het onderzochte Fe-C-Mn-Ti staal bijdragen zijn Fe_3C-precipitaten (88 HV) en dislocaties (54 HV) vanuit een total hardheid van on 284 HV. Beide bijdragen verminderen snel tijdens de eerste stadia van het ontlaten en stabiliseren na 10 minuten. De toevoeging van titanium aan het staal geeft een kleine hardheidsbijdrage, via Ti-atomen in vaste oplossing en via TiC-precipitaten. Ti-atomen in vaste oplossing geven een hardheidsbijdrage die iets toeneemt tijdens de eerste minuten van het gloeien en daarna stabiel blijft (op 25 HV). De directe bijdrage van TiC-precipitaten tot de totale hardheid is beperkt (3,5 HV). Maar TiC-precipitaten dragen ook aan de totale hardheid bij door het (tijdelijk) vasthouden van dislocaties zodat minder herstel plaatsvindt tijdens het ontlaten. Het model voorspelt dat slechts een kleine volumefractie TiC-precipitaten gevormd wordt tijdens ontlaten op 550°C als gevolg van een hoge “misfit strain energy” (1,34 GJ/m^3) en een lage dichtheid van potentiële kiemplaatsen.

In hoofdstuk 6 wordt een vergelijkende studie gepresenteerd van de mechanische eigenschappen bij verhoogde temperatuur en de microstructurele mechanismen tussen ultra-hogesterkte en conventionele hogesterktestaalsoorten die gebruikt worden voor verbindingselementen. De mechanische eigenschappen van verbindingselementen gemaakt van het nieuwe ultra-hogesterkte staal KNDS4 met sterkteklasse 14.9 (treksterkte 1400 MPa en een rekgrensverhouding van 0,9), het conventionele hogesterkte staal 34Cr4 met sterkteklasse 12.9 (treksterkte 1200 MPa en een rekgrensverhouding van 0,9) en 33B2 met sterkteklasse 10.9 (treksterkte 1000 MPa en een rekgrensverhouding van 0,9) worden bij kamertemperatuur en bij verhoogde temperatuur gemeten. De legeringscarbiden in de stalen worden onderzocht om de onderliggende microstructurele mechanismen die leiden tot de verschillende mechanische eigenschappen van de drie materialen te kunnen verklaren. KNDS4 heeft een hogere verhouding tussen de vloeispanning op 500°C en de vloeispanning op kamertemperatuur dan conventionele hogesterkte staalsoorten. De twee conventionele staalsoorten hebben een soortgelijke verhouding tussen de vloeispanning op 500°C en de vloeispanning op kamertemperatuur bij. Deze verhouding blijkt voor alle drie de stalen niet te veranderen als de tijd wordt verlengd van 5 seconden naar 100 uur waarop het staal op hoge temperatuur wordt gehouden. De kruip, zoals gemeten door nano-indrukking, toont een zwakke trend richting een geringere deformatie tijdens nano-indrukking met constante kracht in KNDS4 dan in 34Cr4 en 33B2. De betere mechanische eigenschappen van KNDS4 worden veroorzaakt door de aanwezigheid van legeringscarbiden - die dislocatiebewegingen belemmeren - in de microstructuur. De legeringscarbiden in KNDS4 zijn kleiner dan de legeringscarbiden in 34Cr4 en de eigenschappen zijn daarom beter. Wijzigen van de standaard industriële warmtebehandeling met een austeniteertemperatuur van 940°C naar een austeniteertemperatuur van 1350°C kan de hardheid van KNDS4 met 8% verhogen. Deze stijging komt door het meer effectieve oplossen (i.p.v. vergroven) van bestaande TiC-precipitaten tijdens het austenitiseren. Titanium in vaste oplossing kan leiden tot nucleatie en groei van precipitaten, die op hun beurt de versteviging veroorzaken tijdens het ontlaten. Maar de standaard industriële warmtebehandeling resulteert in kleinere martensietblokken die mogelijk gunstig zijn voor de taaiheid van het staal.

De studie van de martensitische modellegering toont aan dat de martensiet blok structuur stabiel blijft bij temperaturen tot 550 ºC, maar dat de herverdeling van legeringselementen, zoals koolstof, snel is en niet verhinderd kan worden. Bovendien heeft de studie van de model-legeringen bevestigd dat toevoeging van een sterk carbide vormend element, zoals Ti, resulteert in nucleatie van een fijne dispersie van TiC precipitaten, hetgeen herstel voorkomt en daardoor versteviging door zowel precipitaten als dislocaties aan het staal toevoegt. Onze studie van de industriële staalsoorten voor verbindingselementen heeft daarna bevestigd dat carbides van legeringselementen in martensiet de temperatuurbestendigheid van het staal verhogen, door het behoud van een hoge vloeispanning bij hoge temperaturen. De studie van de industriële stalen heeft bovendien aangetoond dat de kruip bij kamertemperatuur in stalen met carbides van legeringselementen gereduceerd is.

De ontwikkeling van meer temperatuurbestendige hoge sterkte staalsoorten voor verbindingselementen zal daarom moeten worden gebaseerd op de versterking mechanismen van martensitiche blok grenzen en op carbides van legeringselementen. Ons onderzoek toont bovendien aan dat er is een behoefte aan verdere studies van traditionele, axiale kruip testen, om de positieve effecten van carbides van legeringselementen in martensitische stalen volledig te begrijpen en evalueren.

Onafhankelijk van de gevolgde warmtebehandeling zijn de verbeterde mechanische eigenschappen van KNDS4 bij verhoogde temperatuur en de lage vervorming tijdens nano-indrukkingen twee belangrijke indicaties om KNDS4 voor verbindingselementen te gaan gebruiken. Het is mogelijk om kleinere, maar sterker bouten met hogere strekte staal te ontwikkelen. Deze bouten kunnen gebruikt worden voor kritische toepassingen in de motor, bijvoorbeeld de drijfstangen, waardoor het mogelijk wordt om de grootte en het gewicht van moderne verbrandingsmotoren te verminderen.

Daarnaast kan de verbeterde temperatuurbestendigheid van de nieuwe martensitische staalsoorten mogelijkerwijseen verhoogde gebruikstemperatuur toegestaan. Deze bouten kunnen daarom mogelijk gebruikt worden in toepassingen waar de temperatuur boven de aanbevolen gebruikstemperatuur van 150°C uit komt (met de maximale bovenste grens van 300°C) zoals vermeld in ISO898-1. Dit maakt het mogelijk om hoog-gelegeerde en hoge temperatuur materialen voor bouten (die zijn ontworpen voor een gebruikstemperatuur van 500°C of meer) te vervangen, die vandaag worden gebruikt in motoren door het huidige gebrek aan kostenefficiënte, resource-efficiënte en micro-gelegeerd staalsoorten die geschikt zijn voor temperaturen tussen 300-500°C.

1 Introduction

When you turn the key to the ignition of your car you immediately put a high load on more than 200 fasteners that are located in the combustion engine of your car. If you drive a hybrid the clutch and electrical engine will add approximately 200 fasteners to the combustion engine. When you drive out on the road, you start using an additional 1500-2500 screws, bolts and nuts located in the driveline, the cassis, the body and the interior of your car, depending on which car size and model you drive [1].

Figure 1.1. *Cylinder head and the cylinder head bolts of an Opel Ampera. This vehicle was disassembled at Nedschroef Techno Centre in order to study the fasteners of a modern hybrid car. The cylinder head bolts have a length of 122 mm.*

Screws and nuts are today completely integrated into the everyday life of every modern society, as they are used within engineering products ranging from buildings and infrastructure, to all kinds of transport vehicles, computers and electronics, medicine, furniture and even jewelry.

Nedschroef is the largest supplier of fasteners for the automotive industry in Europe. Nedschroef has produced and developed fasteners since 1896. The company has never before focused so intensely on research and development as it does today. The major influence for the developments of new fasteners comes from the trends and developments of the automotive industry, which is the largest customer of Nedschroef. I therefore choose an example from the automotive industry, the internal combustion engine, in order to describe which development are taking place at Nedschroef.

The first four-stroke combustion engine was invented in the second half of the nineteenth century [2]. This means that the combustion engine and our products are more or less of the same age. Even though the combustion engine is old, the basics of the engines in the latest F1 car are still the same as the original invention. The pistons move inside the cylinders due to the combustion of an air/fuel mixture and thereby generate the rotation of the crank-shaft which is used to drive the cars. This means that most of the developments of the four stroke engine are fine-tuning of existing constructions and concepts. In fact, the high performance of the F1 vehicles is mainly based on extremely specialized materials and coatings for the majority of the components in the engine and on the vehicle itself. The development of modern mass-produced cars follows the same concepts as the F1 industry, although with more focus on cost and resource efficiency. Today, materials Science is the main innovative field for the development of new engines as well as new combustion fasteners.

The reason behind this is that the focus of engine development has changed course during the last decade. The general awareness of climate change and scarce oil and raw material resources have forced large changes upon the automotive industry. Image, which used to be measured in horse powers and fast acceleration, is now measured in low emissions and low fuel consumption instead. Even the F1 industry has introduced restrictions for fuel consumption since the start of the season of 2014 [3]. This development of low-emission drive lines has resulted in smaller but more powerful engines (down-sizing) and the mechanical and thermal loading of the engines are increasing. For us at Nedschroef this means we need to develop fasteners which are stronger and more temperature resistant (but of course, not more expensive).

1.1 The scope and aim of this thesis

The scope of this PhD study is to investigate the possibility to optimize the microstructure, in order to increase *both* the strength and the temperature resistance, of the industrially available ultra-high tensile strength fastener steel KNDS4. The requirements for the current high-strength engine fasteners are listed in the international fastener standard ISO898 [4]. This standard covers fasteners up to class 12.9, which means a nominal strength of 1200 MPa and a yield point of minimum 90% of the ultimate tensile strength. The ISO standards furthermore recommend a maximum service temperature of 150°C. The industrial aim of the presented research is to develop a fastener steel with a tensile strength that exceeds R_m=1200 MPa and that can be used at service temperatures up to 400°C.

There are three main boundary conditions that must be fulfilled for the development of new engine fasteners. The first condition is related to the traditions and standards within the automotive industry; in order for an ultra-high strength fastener (ultimate tensile strength larger than 1200 MPa) to be accepted by the automotive industry, it must be produced and have properties in line with the currently used, high-strength fasteners. This means that the fastener must have a martensitic microstructure and that the heat treatment must be performed with a tempering temperature of minimum 425°C [4].

The second condition is related to cost. In order to keep the production cost low, the fastener must be produced via cold forming from an annealed wire. This means that the chemical composition of the steel must contain low concentrations of alloying elements (preferably maximum 1 wt% per single alloying element), and that the elements themselves must be abundantly available. The background for reducing the concentration of alloying elements in the steel is twofold. Firstly, most alloy additions result in solid-solution strengthening and possible precipitate strengthening of the steel. This can reduce the formability and will increase the forging loads needed during cold forming, thereby leading to higher tool wear, higher risk for material cracking and higher energy consumption. Secondly, lower concentrations of alloying elements means that we can use our natural resources more efficiently.

The third condition is related to the heat-treatment of the fastener. In order to develop products which can be produced in high volumes, the heat treatment must be done in existing industrial quench and temper equipment and the temperature is limited to maximum temperature of 920-940°C for hardening (austenitization) and a maximum temperature of 600°C for tempering. Higher temperatures will lead to increased CO_2-emission, higher energy consumption and a higher need for furnace maintenance.

The strength of martensitic steels, which are used for the current engine fasteners, originates mainly from the following strengthening mechanisms: (i) elements in solid solution, (ii) grain boundaries, (iii) dislocations and (iv) iron carbides [5-6]. Carbides are phases that consist of metal atoms, combined with carbon atoms, to form a second phase. Carbides in steel are formed only by iron and metals that are located to the left of iron in the periodic table of elements. The metals that have high affinity to carbon and to form carbides, are called carbide forming elements. Common strong carbide-forming elements are niobium (Nb), titanium (Ti), vanadium (V), molybdenum (Mo) and chromium (Cr), which are listed in order of increasing affinity to carbon. Iron carbides consist of Fe and C atoms and alloy carbides, as described in this thesis, consist of carbide forming elements and C atoms. The most common iron carbide in tempered steels is cementite (Fe_3C). Cementite tends to coarsen more rapidly in steel at increased temperatures due to increased diffusivity of carbon atoms in steel. Alloy carbides can be of many forms; MC, M_2C, M_3C, M_7C_3, M_6C and $M_{23}C_6$ [7] where M can be a mix of different carbide forming elements [8]. Alloy carbides typically are smaller than cementite and coarsen at a slower rate due to limited solubility and diffusivity of the carbide forming elements in the steel matrix.

The new, ultra-high strength steels that have been developed for stronger fasteners are based on the addition of precipitation strengthening and grain refinement via alloy carbides [9], similar to what is used in HSLA steels [10]. The alloy carbides contain carbide-forming elements such as Ti, V, Mo and Cr. The alloy carbides in the new steel increase the ultimate tensile strength of the fastener above 1200 MPa. The tempering temperature that is required for the nucleation and growth of alloy carbides is in the range of 550°C, which fits with the requirement of ISO 898-1 and the upper limit of industrial tempering furnaces. The low level of alloy additions needed for precipitation strengthening furthermore enables the steel to be cold formed. More importantly, TiC-precipitates have been shown to have the potential to act as hydrogen traps and improve the resistance to hydrogen-induced damage [11-12] during processing and service of the fastener. The original design of the chemical composition for these new high strength fastener steels was merely targeting higher strength levels and resistance to hydrogen embrittlement. However, thermally stable precipitates are also known to improve the creep properties of steels [13-15] and the tensile strength at elevated temperatures [16], by acting as pinning points for dislocation movement. The high thermal stability of TiC precipitates [17] due to low solubility and low diffusivity of Ti in the steel matrix combined with coherent or semi-coherent interfaces between the TiC-precipitates and the steel matrix therefore makes medium-carbon steel with a small addition of Ti an interesting candidate for the development of ultra-high strength martensitic engine fasteners suitable for service temperatures up to 400°C.

The mechanical properties and performance of the next generation of high strength engine fasteners is based upon a martensite microstructure that is further strengthened with alloy carbides. A fundamental understanding of the relation between the evolution of the microstructure and the evolution of the strengthening mechanisms in martensite is required in order to optimize the heat-treatment process and the properties of new engine fasteners. Our hypothesis is that the next generation of high strength fastener steels, which is based on alloy carbides, can reach higher strength levels, as well as improved temperature resistance compared to conventional high-strength steels for fasteners.

This approach requires further knowledge development. The following research questions were answered during this research project:

1- To which extent do different hardening mechanisms contribute to the strength of martensitic fastener steels?
2- How do the different hardening mechanisms evolve as a function of time during annealing?
3- What are the effects of a strong carbide forming element such as titanium on the microstructure and hardening mechanisms of martensitic fastener steel?
4- Can the strength and temperature resistance of a martensitic fastener steel be improved by addition of carbide forming elements

1.2 The outline of this thesis

This thesis consists of a background chapter, which summarizes the industrial context that led to the research described in this PhD-thesis, four chapters that are based on the research performed within this PhD study, and a concluding chapter.

Chapter 2 consist of three background sections. Section 2.1 gives a short introduction to bolted joints and the use of fasteners in the automotive industry. The key mechanical properties of a fastener are reviewed and the choice of traditional fastener steels is briefly explained. Section 2.2 describes the strength and temperature resistance of metals. The microstructural components that contribute to the strength of metals are discussed and equations for calculating the strength contribution of each hardening mechanism is given. The influence of elevated temperatures on each microstructural feature is reviewed. The phenomena and mechanisms are explained that are behind the creep of metals and different methods to measure creep. Section 2.3 presents martensite formation and precipitation-strengthening of martensite. The basics of martensite formation and the crystallography and microstructure of martensite is discussed. The different strengthening mechanisms of martensite are reviewed and the microstructural processes that take place during tempering of martensite are explained. The kinetic theory behind nucleation and growth of precipitates is presented and the data needed for describing precipitation strengthening based on TiC is summarized, since this precipitate type is studies during the PhD research.

Chapter 3 is based on an experimental study focusing on the evolution of the hardness and microstructure of Fe-C-Mn martensite (without precipitation strengthening of TiC) during tempering at two different temperatures. The results presented give a reference level for the research on the Ti-containing martensite.

Chapter 4 is an experimental study which examines the influence of adding 0.04wt.% of Ti on the evolution of the microstructure and hardness of a Fe-C-Mn steel during tempering. The research confirmed that the precipitation of TiC results in a macroscopic hardness increase of the martensite and that the high dislocation density of martensite significantly increases the rate of TiC growth in martensite.

Chapter 5 is a computational study of TiC nucleation and growth and the evolution of the hardness of martensitic steel during tempering. A multiphase, multi-component hardness model is combined with a Kampmann-Wagner-Numerical (KWN) model for the nucleation and growth of precipitates. The models are subsequently fitted to the experimental results of chapter 4.

Chapter 6 is a comparative study of the mechanical properties at room temperature and elevated temperatures of the new ultra-high tensile strength fastener steel KNDS4 (containing strong carbide forming elements) and conventional high strength fastener steels.

The difference in mechanical properties is explained on the base of the underlying microstructural mechanisms and potential alternative heat treatments of KNDS4 are explored, to further improve the mechanical behaviour.

1.3 References

[1] Statistics based on a tear-down project of an Opel Ampera, performed at Nedschroef Technocentre, 2013
[2] E. Eckerman: World history of the automobile, Society of Automotive Engineers, Warrendale, USA, 2001
[3] http://www.formula1.com/inside_f1/rules_and_regulations/sporting_regulations/12877/
[4] ISO898-1, Mechanical properties of fasteners made of carbon steel and alloy steel-Part 1. Fifth edition, Switzerland, 2013
[5] T. Gladman: The physical metallurgy of microalloyed steels, The University press, London, UK,1997
[6] G. Krauss: Mater. Sci. Eng., A273-275(1999), 40-57
[7] DA. Porter and KE. Easterling: Phase transformations in metals and alloys, Van Norstrand Reinhold, New York, USA, 1981
[8] ADB. Gingell, HKDH. Bhadeshia, DG. Jones and KJA Mawella: J. Mater. Sci., 32(1997), 4815-4820
[9] Y. Namimura, N. Ibaraki, W. Urushihara and T. Nakayama: Wire J. Int., January(2003), 62-67
[10] CY. Chen, HW. Yen, FH. Kao, WC. Li, CY. Huang, JR. Yan and SH Wang: Mater. Sci. Eng. A., 499(2009), 162-166
[11] F-G. Wei, T. Hara, T. Tsuchida and K. Tsuzaki: ISIJ Int., 43(2003), 539-547
[12] J. Takahashi, K. Kawakami, Y. Kobayashi and T. Tarui: Scripta Mater., 63(2010), 261-264
[13] RL. Klueh, N. Hashimoto, FR. Buck and MA. Sokolov: J. Nuclear Mater., 283-287(2000), 697-701
[14] RL. Klueh, N. Hashimoto and PJ. Maziasz: J. Nuclear. Mater., 367-370(2007), 48-53
[15] K. Maruyama, K. Sawada and J-I. Koike: ISIJ Int., 41(2001), 641-653
[16] P. Michaud, D. Delagnes, P. Lamesle, MH. Masthon and C. Levaillant: Acta Mater., 55(2007), 4877-4889
[17] M. Taneike, N. Fujitsuna and F. Abe: Mater. Sci. Tech., 20(2004), 1455-1461

2 Background

This background chapter describes the industrial context that led to the research described in the subsequent chapters in this PhD-thesis. Chapter 2 consist of three main sections: Section 2.1 gives an introduction to fasteners for the automotive industry, which describes forces acting on bolted joints and the required material properties of fasteners that are used in the automotive industry. Section 2.2 zooms into the underlying mechanisms that give strength and temperature resistance to metals, which are two important material properties for automotive fasteners. Section 2.3 describes the relation between the processing, properties and microstructure of martensite that is strengthened with precipitates, which could potentially give the desired combination of strength and temperature resistance to automotive fasteners.

2.1 Fasteners for the automotive industry

2.1.1 Introduction

Fasteners have been used to join automotive components since the very first production of automotive vehicles for human transport (steam powered), in the eighteenth century [1]. The threaded fastener joining method has a major advantage over other joining methods such as welding, brazing, and gluing; the joint can easily be disassembled at any time. For modern cars, where the life cycle of the vehicle is expected to be followed by sorting and recycling of all vehicle components, bolted joints are therefore the key fastening method applied. The fasteners which are used for modern, mass produced cars, are strictly regulated via international standards that stipulate the material, the microstructure and the mechanical properties of the fastener.

2.1.2 Definition and purpose of a bolted joint

A fastener is an element that is used to join two or more components together. Examples of fasteners are a screw, a clip and a rubber band. The work that is described in this thesis is related to screws and bolts. A bolted joint consists of a bolt or a screw, the components that are joined by the bolt/screw and in some cases a nut. The components that are joined are commonly referred to as the clamped parts or the base material. The female thread (which the bolt/screw is assembled into) is present in the form of either a nut or as a threaded hole in one of the clamped parts. The distance measured from under the bolt head to the first engaged thread is called the clamp length, L_c, as shown in Figure 2.1.

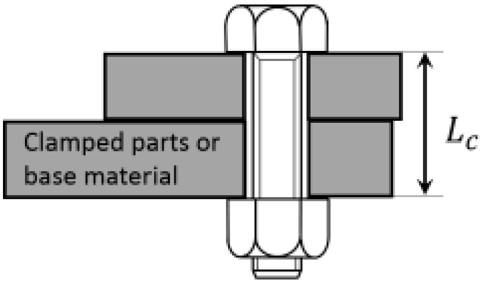

Figure 2.1 *Schematic drawing of a bolted joint, showing the clamp length, L_c, the clamped parts (or base material), the bolt and the nut (at the bottom of the drawing.*

The working principle of a bolted joint is based on the creation of a traction force over the clamped parts, which hold the clamped parts together. This traction force is called the clamp force (F_c). Figure 2.2 shows (a) a properly assembled bolted joint, and (b) an insufficiently assembled bolted joint. The clamp force F_c is illustrated by blue arrows, the force in the bolt (F_{bolt}) is illustrated by green arrows, the external force acting on the joint (F_e) is illustrated by the red arrows and the friction force between the clamped parts (F_f) is illustrated by orange arrows. The clamp force is created by tightening the bolt.

The purpose of the clamp force is to compress the clamped parts so that relative movement or separation of the clamped components is prevented, when external forces are applied to the joint. The task of the fastener is thus to transfer and absorb the forces applied to the joint rather than to act as a "stopping-pin" as demonstrated in Fig. 2.2(b).

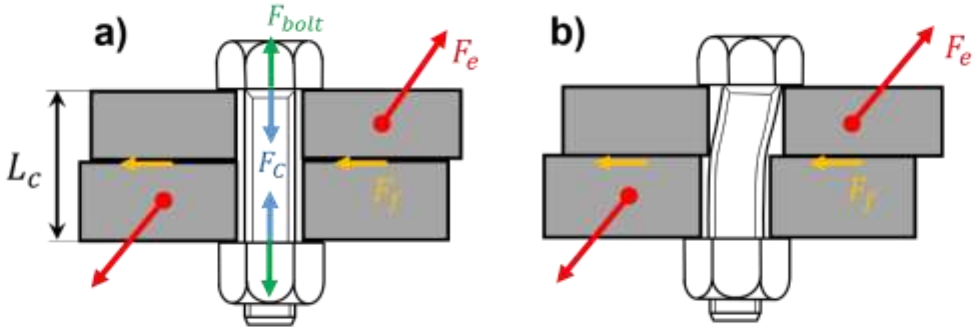

Figure 2.2 *Schematic drawing of bolted joints showing a) a properly assembled bolted joint in which the clamp length (L_c) the clamping force (F_c) and the external forces acting on the joint (F_e) are indicated and b) a bolted joint with insufficient clamping force. Panel b shows that the external forces create unwanted slip at the interface between the clamped parts, because the frictional forces, F_f, are too low to prevent movement of the clamped parts.*

2.1.3 Force distribution in a bolted joint

This section based on the guideline VDI2230 [2], the thesis by G. Toth [3] and the instructions for design of screw joints used by Volvo Cars [4]. The VDI is developed by the German automotive industry and is the most widely applied standard for calculations related to the design of bolted joints that is used within the automotive industry.

The relationship between the bolt elongation, the compression of the clamped parts, the clamp force and external forces in a bolted joint is commonly illustrated in a so called joint-diagram. A joint diagram can be created from a force/elongation diagram, and is a useful tool to understand the distribution of forces in a bolted joint during external loading.

The joint diagram describes the bolted joint as a system of two springs; (i) the screw which acts as a tension spring and (ii) the base material which acts as a compression spring. The stiffnesses of the two springs are of interest as they influence the distribution of external loads between the screw and the base material.

2.1.3.1 Assembled condition

During assembly of a bolt, the section of the bolt that is within the clamp length is elongated by the length of one thread pitch, minus the elastic compression of the clamped parts, for every 360° rotation of the bolt head. The elastic elongation of the section of the bolt that is within the clamp length, creates a tensile force $\vec{\mathrm{F}}_{\mathrm{bolt}}$ in the bolt and a compressive force $\vec{\mathrm{F}}_{\mathrm{base}}$ in the clamped parts or base material in accordance to Hooke's law. Without the presence of external loads on the joint, the tensile force of the bolt will be equal in magnitude and opposite in direction to the compressive force exerted on the clamped parts: $\vec{\mathrm{F}}_{\mathrm{bolt}} = -\vec{\mathrm{F}}_{\mathrm{base}}$. Note that the clamp length of the joint will decrease slightly during tightening, due to elastic (and sometimes plastic) stresses in the base material.

Figure 2.3 illustrates the tensile force of the bolt, F_{bolt} (N), the elongation of the bolt, Δl_{bolt} (m), the compressive force on the clamped parts, F_{base} (N), and the compression of the clamped parts Δl_{base} (m) in a Force/Elongation diagram.

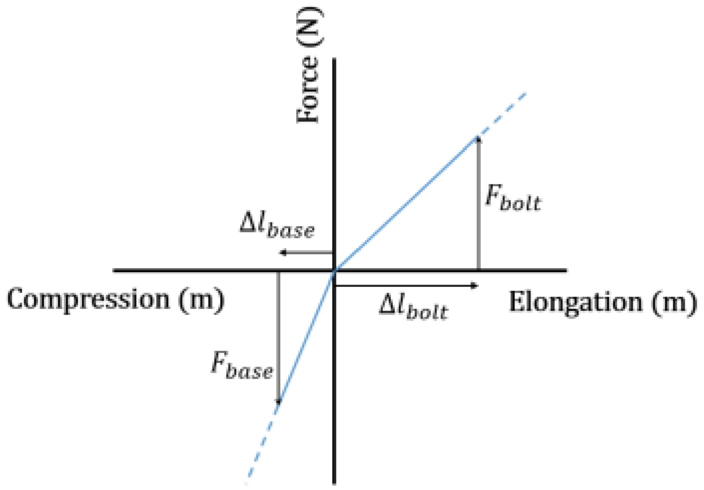

Figure 2.3 *Force distribution during assembly*

Since the bolted joint is described as a system of springs, Hooke's law can be used to define the elongation and compression of the bolt and the base material according to the following basic relationship between forces and elastic deformation:

$$F_{bolt} = k_{bolt}\Delta l_{bolt}, \qquad \textbf{Equation 2.1}$$

$$F_{base} = k_{base}\Delta l_{base}, \qquad \textbf{Equation 2.2}$$

where k_{bolt} and k_{base} are the spring constants of the bolt and the clamped parts respectively. The spring constants describes the stiffness of the bolt and base material.

Figure 2.4 shows the resulting joint diagram which is created from the curves in Fig. 2.3. The joint diagram is made by rotating and mirroring the characteristic line for the clamped parts onto the characteristic line for the bolt, so that they intersect at point A.
The clamp force of the joint, F_c, is measured at the intersection of the curves. In the absence of external forces; $\vec{\mathrm{F}}_{\mathrm{c}} = \vec{\mathrm{F}}_{\mathrm{base}} = -\vec{\mathrm{F}}_{\mathrm{bolt}}$.

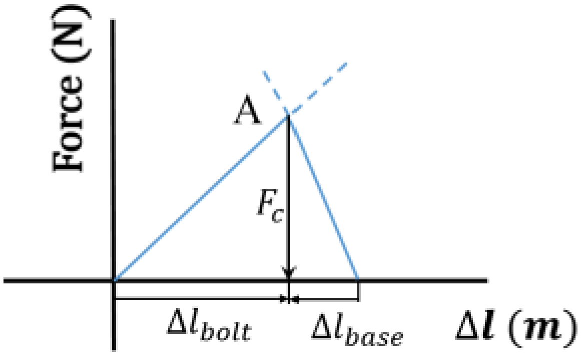

Figure 2.4 *Joint diagram showing the clamping force* $\overrightarrow{\mathrm{F}_c}$ *in an assembled joint.*

The stiffness of the bolt, k_{bolt}, is equal to the slope of the characteristic line of the bolt and can be expressed as:

$$k_{bolt} = A_{bolt}E_{bolt}/L_C, \qquad \textbf{Equation 2.3}$$

where A_{bolt} is the stress area of the bolt, E_{bolt} is the Young's modulus of the bolt material and L_c is the clamp length of the bolt. However, since the bolt head, the bolt shank and the threaded section of the bolt (with stiffnesses k_{bh}, k_{bs} and k_{bt}) will be affected individually by the loading, the stiffness of the bolt consist of several springs, arranged in series, due to which the bolt stiffness can be expresses as:

$$\frac{1}{k_{bolt}} = \frac{1}{k_{bh}} + \frac{1}{k_{bs}} + \frac{1}{k_{bt}} \qquad \textbf{Equation 2.4}$$

The stiffness of the base material, k_{base}, is equal to the slope of the characteristic line of the base material and can be expressed as:

$$k_{base} = A_{base}E_{base}/L_C, \qquad \textbf{Equation 2.5}$$

where L_c is the clamp length and E_{base} is the Young's modulus of the compressed parts. The area of the compressed section of the base material depends on the design of the clamped parts, and the diameter of the hole where the bolt is fitted. If the joint consist of two or more clamped parts the resulting stiffness of the base material shall be calculated as a series of springs, similar to the stiffness of the bolt;

$$\frac{1}{k_{base,total}} = \sum_i \frac{1}{k_{base,i}} \quad , \qquad \textbf{Equation 2.6}$$

where the index i refers to the number of clamped parts.

2.1.3.2 External loading

Most bolted joints in an automotive vehicle are subjected to external loads. An external load (force) can be illustrated as a vertical line in the joint diagram, according to Fig. 2.5. External loads are applied to the bolted joint in the assembled condition. The origin of the external force is therefore the intersection of the lines for the bolt and the clamped parts. If the external load is acting to separate the clamped parts, acting in positive direction of Y-axis, the bolt will experience this as a continued elongation of the clamp length (continue the characteristic line of the bolt). The external load is at the same time acting to reduce the compression of the clamped parts.

Figure 2.5 shows the force distribution in a bolted joint where an external force, F_e, is acting to separate the clamped parts (the external force is applied symmetrically around the center line of the joint, directly under the bolt head). The external load has a positive direction (see the red arrow in Fig. 2.5) and will act to further elongate the bolt. The characteristic line of the bolt is therefore extended (see the blue dotted extension of the bolt line in Fig. 2.5). The external force is fitted to the magnitude of the force between the extended characteristic line of the bolt and the original characteristic line of the clamped parts, originating from point A.

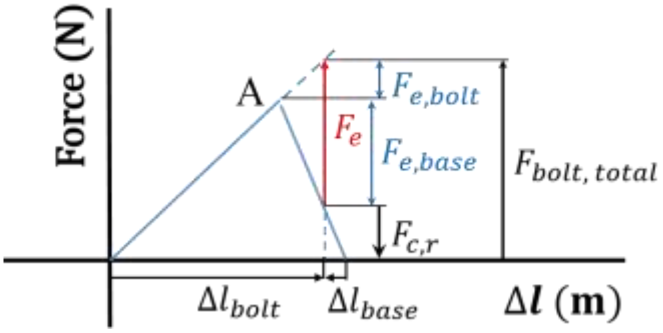

Figure 2.5 *Joint diagram showing the force distribution of an axial external force applied to a bolted joint*

The distribution of the external force into the bolt resp. the base material of the joint can then be illustrated as the blue double headed arrows, $F_{e,bolt}$ and $F_{e,base}$ respectively. The distribution of the external load into the bolt and into the base material is proportional to the stiffness relationship between the bolt and the base material, Φ, which is given by

$$\Phi = \left|\frac{k_{bolt}}{k_{base}}\right| \qquad \text{Equation 2.7}$$

The load increase in the bolt becomes ΦF_e and the load decrease in the base material becomes $(1 - \Phi)F_e$. The remaining load in the bolt and the base material of the externally loaded joint becomes:

$$F_{bolt,r} = F_{bolt} + \Phi F_e \qquad \textbf{Equation 2.8}$$

$$F_{base,r} = F_{base,} - (1 - \Phi)F_e \qquad \textbf{Equation 2.9}$$

In Fig. 2.5, the base material has a higher stiffness than the bolt material. The result of an external load is an increase of the elongation of the bolt and a reduction of the compression of the clamped parts (unloading of the clamped parts by the magnitude of $F_{e,base}$). The remaining clamp force in the joint is $F_{c,r}$. Note that this remaining clamp force must be large enough to prevent relative movements in the joint , via the friction forces (see Fig. 2.2) in case also shear forces are applied.

Figure 2.6 shows an example of an external load which is increased to the point where the base material is completely unloaded, $F_{c,r}$ =0. The remaining clamp force is now reduced to zero and the complete external load is distributed into the bolt. In the case that the clamp force is reduced to zero, relative movements of the clamped parts cannot be prevented.

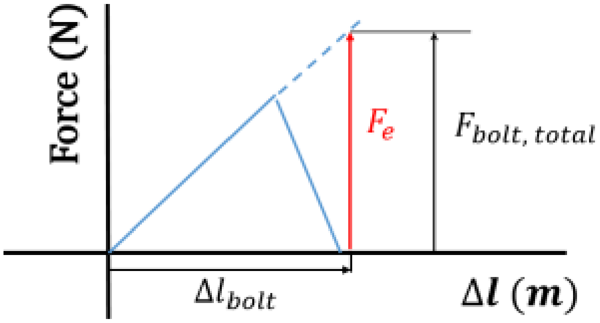

***Figure 2.6** Joint diagram showing complete loss of clamp force due to overload.*

2.1.3.3 Settlement

Any process which reduces the elastic elongation of the bolt in a bolted joint is called settlement. Settlement can occur in all contact surfaces of the joint, including the threads. The parameters which determine the extent of the settlement are surface roughness, surface hardness and parallelism of clamped parts and the fastener. Clamp force losses due to creep can also be included in settlements.

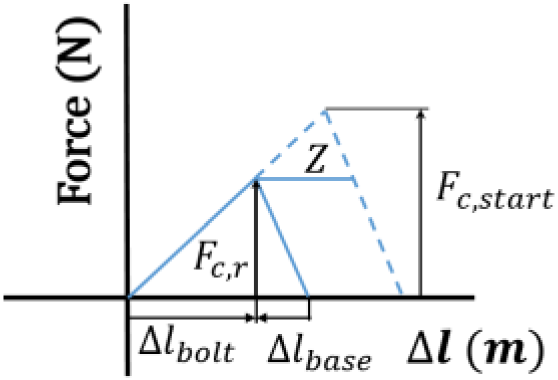

Figure 2.7 *Joint diagram showing the impact of settlement Z in a bolted joint.*

Figure 2.7 shows how settlements can be visualized in the joint diagram. Settlement is measured in distance (m) and is commonly given the name Z in joint diagrams. Z can be visualized by a horizontal line (along x-axis) with a length equal to the sum of the reduction of bolt elongation and the base material compression, due to settlements. The starting point for Z in the joint diagram is the intersection of the two characteristic lines of the bolt and the clamped parts after assembly. Settlements will lead to a reduction of the clamp force and is therefore fitted (given in magnitude along the X-axis) between the characteristic lines for bolt and clamped parts, below their intersection point. After fitting the Z-line, a new characteristic line for the base material can be drawn (with the same slope as the old line) from the intersection of Z and the characteristic line of the bolt, see the new solid line for the base material. The remaining clamp force in the joint can then be shown as $F_{c,r}$. The elongation of the bolt is reduced, as well as the compression of the clamped parts.

2.1.3.4 Fatigue

Fatigue is failure, at relatively low stress levels, of structures that are subjected to fluctuating and cyclic stresses. Failure of the material by fatigue is characterized by three distinct steps. The first step is the initiation of small cracks that form at high stress concentrations at the surface or internal flaws. Secondly, the crack slowly propagate with each stress cycle during which the crack advances incrementally. Thirdly final failure occurs very rapidly once the advancing crack has reached critical size. A greater applied stress range (load amplitude) results in a higher crack growth and therefore sooner fracture of the structure (short fatigue life).

The distribution of an altering load in a bolted joint will follow the same principle as discussed in section 2.1.3.2. The part of the external load that is distributed into the bolt will determine the amplitude of the cyclic loading that acts upon the bolt. The fatigue life of the fastener is therefore very dependent on the stiffness relationship between the bolt and the base material. The methods to improve fatigue life of the fastener itself include avoiding surface damages and assuring a large radius of curvature under the bolt head and in the thread roots in order to minimize stress concentrations. Additional improvements of fatigue life of threaded fasteners can also be achieved by producing the threads on the bolt via deformation (rolling) after the heat treatment, thereby introducing compressional stresses on the thread surface, and by the choice of the material (and microstructures) with good fatigue properties.

2.1.4 Mechanical properties of a fastener

2.1.4.1 Tensile strength

The tensile strength of the fastener material (together with the diameter of the fastener) determines the maximum clamp force which can be achieved in a bolted joint. As described in section 2.3.1 the clamp force in the joint is generated by an elongation of the section of the bolt, within the clamp length of the joint, during tightening (see Figs. 2.3 and 2.4). However, the assembly torque that is applied in order to rotate the bolt head and elongate the bolt will generate both axial and torsional stresses in the bolt material, as shown in Fig. 2.8. If the friction between the bolt and the female threads in the joint is high during assembly, the torsional stresses will be high. The outer diameter of the bolt, in the section within the clamp length of the joint, experiences the highest stresses (a combination between axial and torsional stress) and yielding of the bolt material starts here, if the combined stresses becomes too high during assembly. As soon as the assembly torque is removed, the majority of the torsional stresses disappear (with the exception for bolts with very long clamp length).

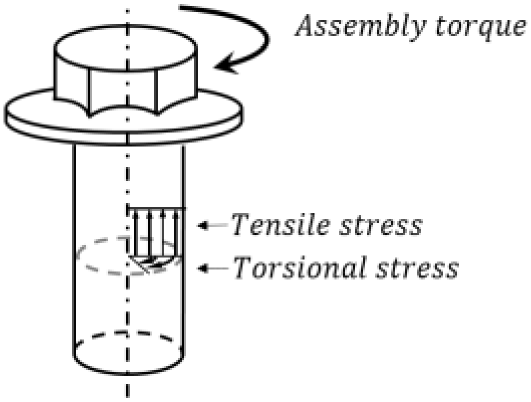

Figure 2.8 *Stresses in a fastener during tightening, redrawn after ref. [4].*

Tightening a fastener to a point close to or over the ultimate tensile strength of the fastener should be avoided as this will lead to changes of the thread pitch (of the threads which are present in the clamp length section of the bolt), work hardening of the material in the clamp length section of the bolt, possible necking of the bolt and the risk of elongating the bolt beyond the design of the joint. With respect to the strenght of the joint, once the yield point of the bolt material is reached, extended deformation of the bolt will only lead to a marginal increase of clamp force. A high yield point in relation to the ultimate tensile strength is therefore preferred, as this will make it possible to achieve a higher clamp force without deforming the bolt plastically.

2.1.4.2 Stiffness

The stiffness of the bolt (in relation to the stiffness of the clamped parts) will determine how the external forces are distributed in the bolted joint. A low bolt stiffness compared to the stiffness of the clamped parts is desirable as this will generate a small Φ according to Eq. 2.7 and therefore limit the distribution of external forces into the bolt. If a smaller portion of the external loads is distributed into the bolt, the fatigue life of the bolt will improve, since the amplitude of the dynamic load is reduced.

In addition to low material stiffness, a long clamp length of the fastener is desirable as this reduces the stiffness of the bolt itself according to Eq. 2.3. A long clamp length will furthermore enable a longer distance that can be elongated elastically, thereby making the joint more robust for settlements (see Fig. 2.7).

2.1.4.3 Toughness

The toughness of a fastener material can affect both impact behavior and fatigue life of a bolted joint. Engine fasteners are in most cases subjected to dynamical loading from the rotation speed of the engine, as well as vibrations from driving conditions. High toughness is therefore desirable, as this can improve fatigue life.

Furthermore, the fastener material needs to have a high impact toughness, in order to be able to absorb large amounts of energy during loading peaks originating from driving conditions (pot holes in the road) or in the worst case during crash.

In addition to this, high toughness of the fastener material will contribute to improved resistance to hydrogen embrittlement, which might occur in service environments that can generate hydrogen (such as corrosion).

2.1.4.4 Creep

The result of creep of a fastener material during service is a reduction of the clamp force of the joint. The decrease will manifest itself as a settlement, as described in section 2.1.3.3. High creep resistance of fastener materials is therefore desirable. As the clamp length of a joint seldom changes during service (with the exception of high temperature joints, where thermal expansion of all components will change the conditions), creep of fastener materials will lead to stress relaxation (stress relief under constant strain).

2.1.5 Choice of fastener material

Several factors have to be taken into account when a material is chosen for a specific fastener. The factors are typically (i) standards and customer demands, (ii) price, (iii) availability as raw material wire and (iv) tradition. The most commonly applied standards for the choice of fastener materials within the European automotive industry are listed in the international ISO and DIN standardization systems. The ISO and DIN standards set restrictions to the mechanical properties, the chemical composition, the microstructure and the heat-treatment process for the production of the fastener.

2.1.5.1 Current high strength fasteners

The majority of all high-strength fasteners used within the European automotive industry are defined according to the standard ISO 898-1 (screws) [5]. ISO898-1 covers fasteners with a nominal strength ranging up to 1200 MPa, so called grade 12.9 (screws). The first number in the grade name indicates the ultimate tensile strength R_m (in multiples of 100 MPa) and the second digit expresses the yield strength $R_{p0,2}$ (as expressed in 1/10 fractions of R_m). In the case of the example: $R_{p0,2} = 0.9\ R_m$. The ISO898-1 standard recommends a maximum service temperature of 150°C. The ISO system furthermore stipulates that high-strength fasteners grades ($R_m \geq 800$ MPa) should be made from carbon steel, boron-alloyed carbon steel or alloyed steel (typically alloyed with Cr). The microstructure of the fastener should be tempered martensite. Fasteners are typically produced via cold forming from a well annealed (ferritic/perlitic or spheroidized) wire and thereafter heat treated to attain the final mechanical properties and microstructure of the fastener product.

Table 2.1 shows the ISO898-1 demands on chemical composition for high strength fasteners. The fastener manufacturers are free to choose any steel that fulfills the requirements related to the concentrations of the chemical elements C, P, S and B and that fulfils the requirements related to the mechanical properties after a quench and temper treatment using a minimum tempering temperature of 425°C.

The demands of table 2.1 allow for a large variety of steels to be applied, and different fastener manufacturers apply different steels, based on price, tradition, availability (as wire) and possibly customer specific demands.

Table 2.1 *Steel chemistry for 8.8, 10.9 and 12.9 grade fasteners according to ISO898-1 [5]*

Property Class	Material and heat treatment	Chemical composition limits (cast analysis, wt.%)					Tempering Temperature °C min
		C		P	S	B	
		min	max	max	max	max	
8.8[f]	Carbon steel with additives (e.g Boron or Mn or Cr) quenched and tempered	0.15[e]	0.40	0.025	0.025	0.003	425
	Carbon steel quenched and tempered	0.25	0.55	0.025	0.025		
	Alloy steel quenched and tempered[g]	0.20	0.55	0.025	0.025		
10.9[f]	Carbon steel with additives (e.g. Boron or Mn or Cr) quenched and tempered	0.20[e]	0.55	0.025	0.025	0.003	425
	Carbon steel quenched and tempered	0.25	0.55	0.025	0.025		
	Alloy steel quenched and tempered[g]	0.20	0.55	0.025	0.025		
12.9[f,h,i]	Alloy steel quenched and tempered[g]	0.30	0,50	0.025	0.025	0.003	425
E	In case of plain carbon boron steel with a carbon content below 0,25% (cast analysis), the minimum manganese content shall be 0,6% for property class 8.8 and 0,7% for 10.9						
F	For the materials of these property classes, there shall be sufficient hardenability to ensure a structure consisting of approximately 90% martensite in the core of the threaded sections for the fasteners in the "as-hardened" condition before tempering.						
G	This alloy steel shall contain at least one of the following elements in the minimum quantity given: chromium 0,30%, nickel 0,30%, molybdenum 0,20%, vanadium 0,10%. Where elements are specified in combinations of two, three or four and have alloy contents less than those given above, the limit value to be applied for steel class determination is 70% of the sum of the individual limits shown above for the two, three or four elements concerned.						
H	A metallographically detectable white phosphorus layer is not permitted for property class 12.9. It shall be detected by a suitable test method						
I	Caution is advised when the use of property class 12.9 is considered. The capability of the fastener manufacturer, the service conditions and the wrenching methods should be considered. Environments may cause stress corrosion cracking of fasteners as processed as well as those coated						

Literature also lists some steels for ultra-high tensile strength fasteners (R_m >1400 MPa) like the W.nr steel 1.7783, 1.6359 and 1.4534 [6]. These materials are at present not applied for high volume serial production due to high price of the raw material and poor formability in cold forging.

2.1.5.2 Current high temperature fasteners

The high temperature fasteners that are approved for use by the European automotive industry are defined according to DIN EN10269 [7]. This standard lists several types of metals: alloy steels, stainless steels of austenitic and martensitic structures and nickel based alloys. DIN ISO 10269 specifies the chemical composition, the heat treatment process parameters and the mechanical properties of the fastener. However, due to high raw material prices and poor availability of the metals in DIN ISO 10269 as wire, only a few of the listed metals are found in high volume automotive applications. The high temperature metals commonly have limited formability in cold forging and require heat treatments that are time consuming and expensive.

Table 2.2 lists the few high temperature metals that are commercially available as fasteners and commonly used within the automotive industry.

Table 2.2 *Common high temperature fastener materials*

Material		**Microstructure components**	**Service temperature range**
1.7709	21CrMoV5-7	Ferrite/martensite	Up to 500°C
1.7711	40CrMoV4-6	Ferrite/martensite	Up to 500°C
1.4923	X22CrMoV12-1	Martensite	Range 500-550°C
1.4980	X6NiCrTiMoVB25-15-2	Austenite	Up to 700°C
2.4952	NiCr20TiAl	Austenite (Nickel base)	Up to 1000°C

2.2 Strength and temperature resistance of metals

2.2.1 Introduction

This section is written to give an introduction to the strength and temperature resistance of metals. Section 2.2.2 gives the definition of strength and temperature of metals. Section 2.2.3 is related to dislocations and dislocation movement. The concept of dislocations is explained and the mechanisms behind different types of dislocation movement are laid out. In section 2.2.4, the link between dislocations and the strength of metals is examined and the different microstructure components that contribute to the strength are reviewed in separate sub-sections. The strengthening mechanism behind each microstructural component is discussed and equations for the quantification of the strengthening effect, together with literature values related to steel are given. Each subsection ends with a brief statement of the influence that elevated temperatures have on each microstructure component. Section 2.2.5 is related to the phenomena of creep. Creep is the time-dependent and permanent deformation of a metal under external loading. The mechanical behavior during the different stages of creep is discussed. Thereafter, the microstructural mechanisms underlying creep are discussed. Subsequently, expressions are given for the different mechanisms of creep. Section 2.2.5 ends with a description of the different methods to measure creep, with special focus on the indentation creep method, since this method was used within the research of this PhD study.

2.2.2 Definitions of strength and temperature resistance of metals

The strength of a metal can be defined as the ability to withstand deformation during exposure to external mechanical load. Deformation of metals can be divided into two different stages: (i) Elastic deformation in which the material returns to its original shape in case the external load is removed and (ii) plastic deformation, in which the shape of the material is permanently changed [8], see Fig. 2.9. Elastic deformation of metals is the result of the stretching of atomic bonds (without the breaking and forming of atomic bonds) and reversible dislocation motion. Plastic deformation of metals is the result of breaking and re-forming of bonds via the movement of dislocations.

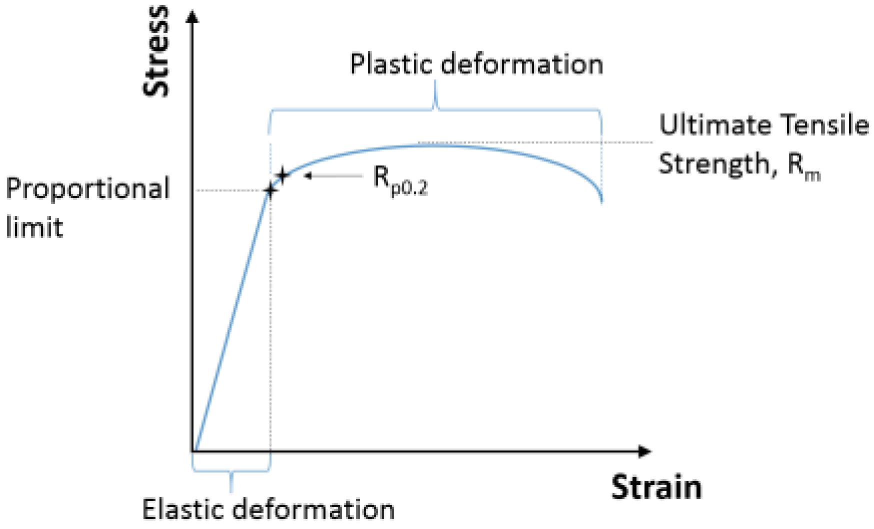

Figure 2.9 *Schematic drawing of the engineering stress-strain curve of a metal as measured during tensile testing, which show two important stages of deformation: elastic and plastic deformation. In practice, the proportional limit, which indicates the transition from elastic to plastic deformation, might be difficult to determine. Therefore the yield strength ($R_{p0.2}$) is defined as the stress required to produce a plastic strain of 0.2%. The (ultimate) tensile strength (R_m) is the maximum engineering stress, in tension, that may be sustained without fracture.*

The proportional limit of a metal is the stress at which elastic deformation changes into plastic deformation. For most engineering applications the strength of a metal reflects the resistance to plastic deformation and the yield strength therefore is the central characterization of material strength. Also the hardness of a metal is an indication of a metal’s resistance to plastic deformation. Strength and hardness are therefore considered as proportional within this thesis [8].

The temperature resistance of a metal can be defined as the ability of the metal to withstand plastic deformation and oxidation at elevated temperatures. The oxidation resistance of metals at elevated temperatures falls outside the scope of this thesis, because fasteners made out of steel can be coated to avoid oxidation. It is important to consider the temperature resistance of steel for fasteners, because engine fasteners are used at elevated temperatures.

Plastic deformation of metals due to an external load at elevated temperatures can take place quickly after applying the external load or can take place a long time after applying the external load. In the former case, the external load has to exceed the yield strength of the metal at elevated temperatures before plastic deformation takes place at relatively short time scales. In the former case it is important to know how the yield strength of the metal decreases with increasing temperature. In general, the yield strength ratio, i.e. the yield strength $R_{p0.2}(T)$ at temperature T divided by the yield strength $R_{p0.2}(25\ ℃)$ at room temperature, will change with temperature, as schematically shown in Fig. 2.10(a).

In the latter case, creep is the dominant mechanism by which plastic deformation takes place. Creep is the time-dependent plastic deformation of a metal when subjected to a load or stress that can be lower than the yield stress, which typically takes place at elevated temperature. Figure 2.10(b) schematically shows the evolution of the strain of a metal as a function of time during creep at elevated temperature. The ability of a metal to withstand plastic deformation is directly related to the microstructure of the metal. In case that heating the metal to elevated temperatures leads to changes in the strengthening components of the microstructure, the strength of the metal is affected.

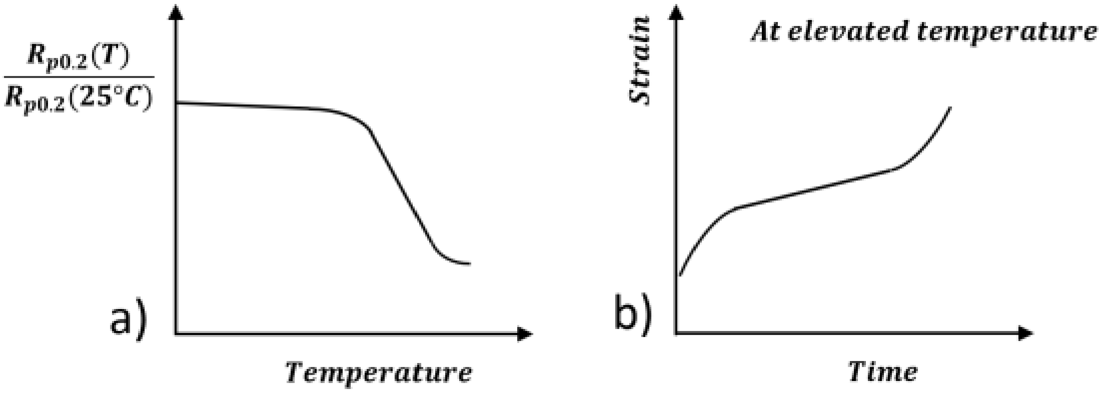

Figure 2.10 *The effect of temperature on a) the yield strength and b) the creep behavior during constant load and temperature exposure.*

2.2.3 Dislocations and dislocation movements

This section is mainly based on Ref. [9]. Plastic deformation of a metal takes place via the motion of dislocations in response to an applied shear stress. A dislocation is a linear crystallographic defect in the metal lattice, around which there is atomic distortion. The magnitude and direction of the lattice misalignment that is caused by the presence of a dislocation is commonly called the Burgers vector, b. The Burgers vector can be found by following the lattice in a square around the dislocation, as illustrated in Fig. 2.11. When a square in a dislocation-free lattice is investigated each parallel side of the square has an equal number of lattice steps. However, when a dislocation is present in the lattice (right pane), one of two parallel sides of the square will contain one extra lattice site. The length of this extra step is the magnitude of the Burgers vector, and the direction of the extra step is the direction of the burgers vector, see Fig. 2.11.

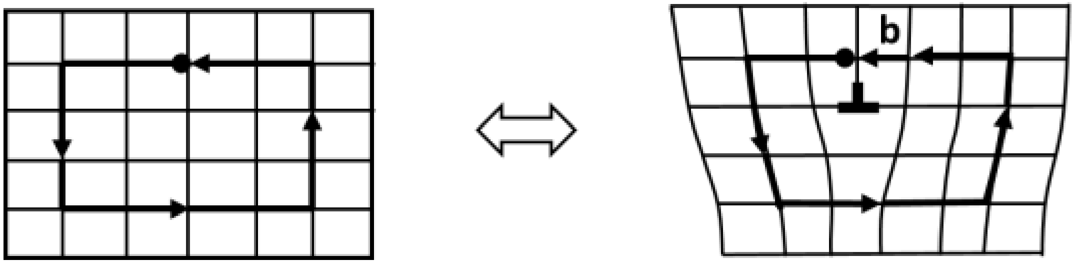

Figure 2.11 *Burgers vectors illustrated for an edge dislocation, redrawn after [9]*

Dislocations can be of three types; (i) edge, (ii) screw, and (iii) mixed dislocations. Dislocations are present in all metals and form during solidification and solid-to-solid phase transformations. During plastic deformation of metals the dislocation density strongly increases.

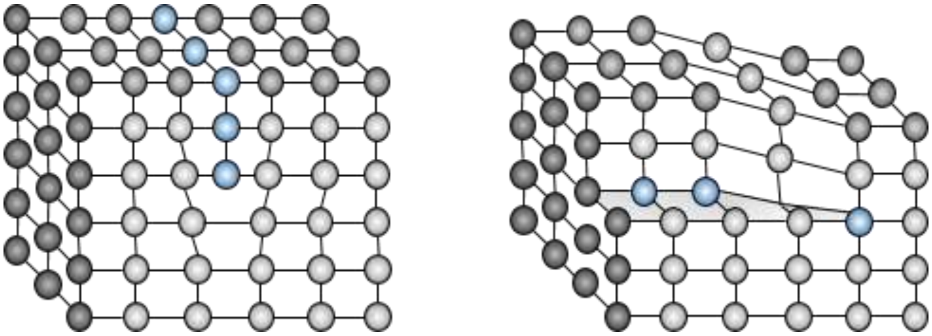

Figure 2.12 *Edge dislocation (left) and screw dislocation (right)*

Dislocation movement in a lattice is illustrated for an edge dislocation in Fig. 2.13. The force that is required to move the dislocation through the lattice is significantly lower than the force that would be required to move the entire plane of atoms over the adjacent plane over an interatomic distance. This is why deformation occurs via movement of dislocations and at a much lower stress than the theoretical strength of a perfect crystal. As the dislocations move, the material is plastically deformed.

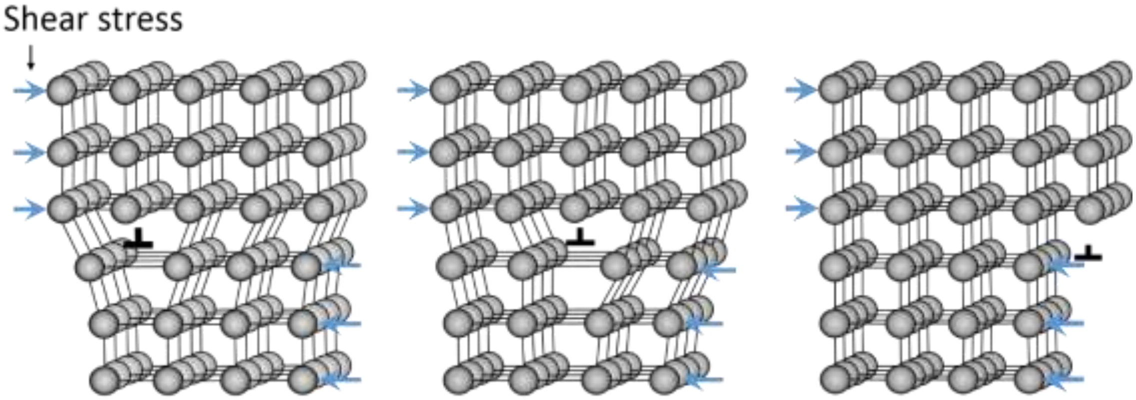

Figure 2.13 *Movement of an edge dislocation, redrawn after [8]*

Dislocation movements can be of two types; (i) glide (also called slide) or (ii) climb. Dislocation glide is a dislocation movement which takes place *along* a slip plane of the host lattice and along a slip direction. The combination of slip plane and direction is commonly referred to as a slip system.

Cross-slip is a type of glide movement, where the dislocation changes direction from one slip plane into another slip plane (still moving along the slip planes). As there are only a limited number of slip systems available within a lattice, the number of possible dislocation glide movements is restricted. Note that different lattice types contain a different number of available slip systems.

Dislocation climb is a movement where the dislocation *moves out of* the slip plane of the host lattice, atom by atom. This migration outside the slip plane requires the presence of vacancies in the host lattice. Climb is a thermally activated process and can allow dislocations to circumvent obstacles. Climb primarily takes place at elevated temperatures as the number of vacancies and the atomic mobility is increased at elevated temperatures.

2.2.4 The microstructural components that strengthen metals

All dislocations are surrounded by small strain fields, as illustrated in Fig. 2.14. These dislocation strain fields can interact with other strain fields that might be present in the lattice.

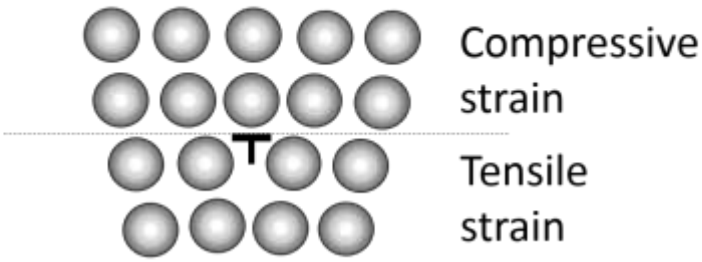

Figure 2.14 *Strain field surrounding a dislocation*

The interactions between different strain fields that might be present in the lattice and the dislocation strain fields commonly lead to reduced dislocation mobility. As described previously, the yield strength of metals is related to the stress that is required to move dislocations through the lattice. This stress can be described according to the general expression:

$$\sigma_y \propto \frac{MGb}{L}, \qquad \textbf{Equation 2.10}$$

where M is the Taylor factor, L is the distance between pinning points in the lattice, G is the shear modulus and b is the Burgers vector. Pinning can be due to interacting stress fields or, in general, due to obstacles. The most common interaction between dislocations and microstructure features which result in reduced dislocation mobility are called the strengthening mechanisms of metals [8].

The total strength of a metal at ambient temperatures is built up from contributions from five microstructure components; (i) the lattice friction, σ_l, (ii) solid solution strengthening, σ_{ss}, (iii) grain boundary strengthening, σ_{gb}, (iv) dislocation strengthening, σ_d and (v) precipitation strengthening σ_p. The last four components involve strengthening of the metal by providing obstacles for the motion of dislocations and are commonly referred to as the strengthening or hardening mechanisms of metals.

There are several methods for expressing the interaction and superposition of the different microstructure components to the total strength of metals. The most simple and common method is linear superposition: the total strength is a linear addition of all microstructure components. The linear superposition can be expressed as [10]:

$$\sigma_{tot} = \sigma_l + \sigma_{ss} + \sigma_{gb} + \sigma_d + \sigma_p \qquad \textbf{Equation 2.11}$$

These 5 microstructural components are discussed separately in next sections.

2.2.4.1 Lattice friction

The lattice friction characterizes the force which is needed for glide movement of a dislocation along one slip-plane. This force is called the Peierls-Nabarro force and is representative for a pure crystal without any additional strengthening mechanisms [11]. The lattice friction depends on the atomic bonding energy between neighboring atoms in the lattice. The bonding energy is the energy required to separate two atoms that are chemically bonded to each other. The lattice friction can be regarded as the intrinsic strength of a metal.

The lattice friction of a metal is affected at increased temperature via a reduction of in atomic bonding energy. Rising the temperature of a metal leads to increased vibrations and increased vibrational energy of the atoms in the lattice. In case the temperature of a metal rises, the mean distance between the atoms increases and the bonding energy between the atoms decreases. A decrease in the bonding energy decreases the lattice friction, which means that the intrinsic strength of the metal is reduced.

The binding energy between atoms is an intrinsic property of the metal. The reduction in the intrinsic strength of a metal due to an increase of the temperature cannot be prevented. However, the effect is reversible: reducing the temperature will lead to an increase in the intrinsic strength of the metal.

2.2.4.2 Solid solution

Solid solution is the solution of solute atoms into a solvent host lattice, in the solid state. In metals the solute atoms are commonly referred to as impurity atoms or alloy atoms. The position of the solute atom in the host lattice depends on the atom sizes. If the solute atom is small in comparison to the host lattice atom type, the solute atoms fit into interstitial positions, according to Fig. 2.15(a). If the solute atoms are similar in size, or larger, in comparison to the host lattice the solute atoms take substitutional positions, according to Fig. 2.15(b).

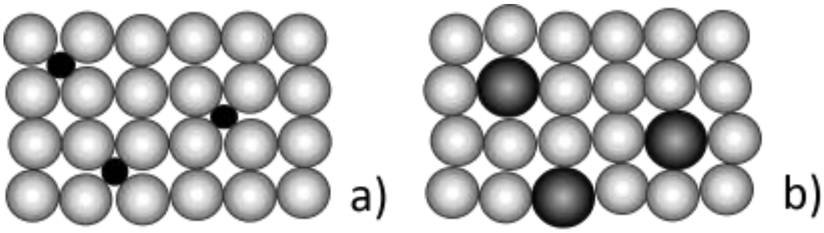

Figure 2.15 *Solid solution by (a) interstitial elements and (b) by substitution elements.*

The strengthening mechanism of solid solution stems from the local strain fields which form around the solute atoms. These strain fields are caused by (i) the difference in atom size comparing foreign atom and host atoms, including the interstitial atoms being larger than voids, and (ii) the differences in bonding characteristics comparing host-to-host atom bonds and host-to-solute atom bonds [12]. The strain fields around the solute atoms interact with dislocations and reduces the dislocation mobility.

The strength increase which can be achieved from solid solution in metals depends on the atomic characteristics and concentration of the solute atoms. Solid solution strengthening can be expressed as a simple additive power law [13]:

$$\sigma_{ss} = \sum_i K_i \cdot (C_i)^{n_s}, \qquad \textbf{Equation 2.12}$$

where K_i is a proportionality constant for element i, C_i is the concentration of element i and n_s usually ranges between 1/3 and 2.

The solid solution strengthening of low concentrations of alloy elements in steel (bcc ferrite structure) is commonly assumed to be approximately linear, n_s=1, at low concentrations [14]. The strengthening effects of several alloying elements is schematically represented in Fig. 2.16. Note that interstitial elements C, N and P are more effective than the substitutional elements

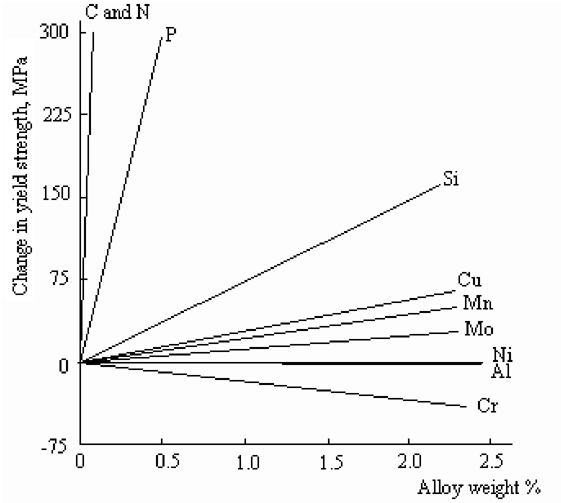

Figure 2.16 *Solid solution strengthening by alloy elements in steel [14]*

Solid solution strengthening is affected at increased temperature via increased diffusivity. Diffusivity describes the mobility of atoms. The diffusivity can also be called the diffusion coefficient, and is given the SI unit m^2/s. The increase in diffusivity at elevated temperatures can be described according to [15]:

$$D = D_0 \exp\left(\frac{-Q_D}{kT}\right), \qquad \textbf{Equation 2.13}$$

where D_0 is the pre-exponential factor, Q_D is the activation energy for diffusion, k is Boltzmann's constant and T is the temperature. Increased diffusivity of solute atoms at elevated temperature leads to higher mobility of the solute atoms than of the dislocations, with the result that the solute atoms no longer restrict the mobility of the dislocations [16].

Diffusion is a time dependent process that can lead to both irreversible and reversible yield strength loss. When the increased temperature is reduced again, the mobility of solute atoms is also reduced, and the solute atoms go back to contribute to solid solution strengthening. However, solute atoms that segregate into grain boundaries or lattice defects such as interphases of precipitates, cause an irreversible yield strength loss.

Increased diffusion can in some specific cases lead to increased solid solution strengthening. Interstitial solute atoms, such as carbon and nitrogen in steel, can diffuse to dislocations in order to relax their solute strain field and the dislocation strain field. This is called a Cottrell atmosphere. The effect of a Cottrell atmosphere is reduced dislocation mobility because the solute atoms in the Cottrell atmosphere increase their energy when the dislocation moves away. The phenomenon of decreased dislocation mobility due to Cottrell atmospheres is called strain ageing [17]. Strain ageing is particularly marked in mild steel and soft iron.

Strain ageing is time- and strain dependent [18]. The rate of strain ageing depends on the migration rate of the solute atoms to the dislocation. The ageing temperatures which normally are involved in strain ageing vary for different metals; e.g. austenitic stainless steel show strain ageing due to carbon and nitrogen atoms in the temperature range of 200-600°C [19].

2.2.4.3 Grain boundaries

A grain boundary is the interface between neighboring crystals of the same crystal structure but varying crystallographic orientations (each crystal is called a grain). Grain boundaries can be sub-divided in several ways, where the coarsest subdivision is into two categories: (i) low angle grain boundaries and (ii) high angle grain boundaries. The angle refers to the crystallographic mis-orientation between the neighboring grains. The distinction between low and high angle is usually drawn at 15°. Low-angle grain boundaries are made up of rows of dislocations, as for an example shown in Fig. 2.17 for a tilt boundary. Early theories suggested that high-angle grain boundaries consisted of a thin disordered layer, but now it is known that these boundaries consist of regions of good and bat matching between the two grains. This theory is known as the concept of the coincidence site lattice (CSL). The coincident site lattice (CSL) theory considers the fit of the outermost atom layer of two neighboring grains. This theory is based on counting the fraction of lattice sites which coincide between the two lattices of the neighboring grains. A boundary that contains a high density of lattice points in a CSL has a good atomic fit.

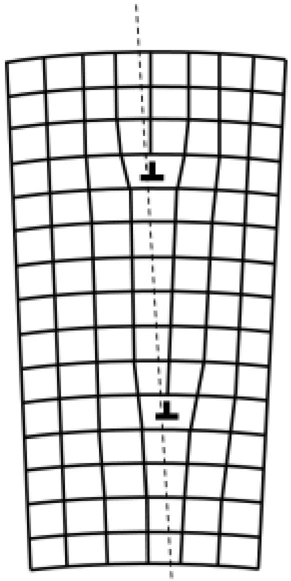

Figure 2.17 *A tilt boundary, which is a type of low angle grain boundary consisting of misfit dislocations*

Grain boundaries act as barriers to dislocation motion for two reasons: (i) there is a change in the direction of the slip planes at the grain boundary between two neighboring grains according, as illustrated in Fig. 2.18, and (ii) there is a discontinuity between the slip planes of the two neighboring grains. In the case of high angle grain boundaries, the dislocations tend to 'pile' up at the grain boundaries, which introduces stress concentrations ahead of their slip planes. This generates new dislocation in the adjacent grains.

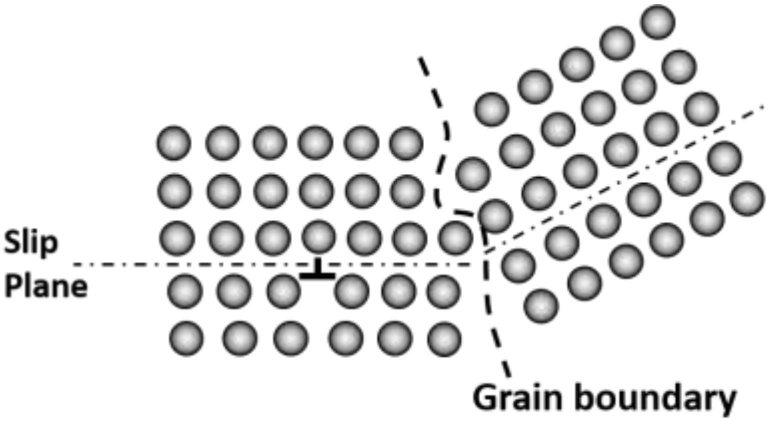

Figure 2.18 *Neighboring grains which have different orientation of slip plane.*

The strength increase which can be achieved via grain boundary strengthening depends on the grain size and is commonly estimated via the empirical Hall-Petch equation [20-21]:

$$\sigma_{gb} = k_D \cdot {d_g}^{-1/2}, \qquad \textbf{Equation 2.14}$$

where d_g is the grain size and k_D is the strengthening coefficient (Hall-Petch term). The strengthening coefficient is different for different metals. The strengthening coefficient k_D for micro-alloyed steel varies, but is often found to be consistent within the range of 17.4 to 23.5 MPa $\text{mm}^{-1/2}$ [14, 22].

Grain boundary strengthening is affected at increased temperature via grain coarsening. Grain coarsening involves the migration of grain boundaries. The driving force for grain coarsening is the reduction of the total grain boundary energy in the metal. It is common that high energy grain boundaries have a higher mobility than low energy grain boundaries and therefore enable faster coarsening. Grain coarsening leads to a reduction of the grain boundary strengthening contribution, since grain coarsening results in increased mean grain sizes.

Grain coarsening is a time dependent process that leads to irreversible yield strength loss. When the temperature is reduced, the yield strength is permanently reduced. The rate at which grain coarsening takes place depends on the temperature, the type of grain boundaries (e.g. low-angle or high-angle grain boundaries), the composition of the metal and the density of obstacles for grain boundary migration. It is possible to reduce the rate of grain coarsening via solute atoms and via precipitates of a second phase. Certain solute atoms (impurities as well as alloying elements) can segregate to grain boundaries, in order to reduce their energy. The segregation leads to a higher solute concentration in and around the grain boundaries. Locally higher concentrations of solute atoms reduce the grain boundary mobility since motion of the grain boundary increase the energy of the solute atom cloud (similar to strain ageing). The phenomenon is related to solute drag [23-24]. Precipitates in a metal can reduce, or even stop, grain coarsening, as the precipitates can exert a pinning effect on the boundary [25]. However, if coarsening of precipitates takes place this will lead to less efficient pinning of grain boundaries and continued grain coarsening.

2.2.4.4 Dislocations

The strain fields which surround a dislocation can interact with the strain fields of neighboring dislocations. This interaction between dislocations can lead to dislocations repelling each other or attracting each other, depending on their Burgers vectors. If two dislocations of the similar Burgers vector approach each other, they repel each other, which reduces dislocation mobility. Furthermore, intersecting dislocations can pin each other.

The strength increase which can be achieved via dislocation strengthening, σ_d, depends on the dislocation density and can be expressed according to Bailey-Hirsch [26] by:

$$\sigma_d = M\alpha G b \cdot \rho^{1/2}, \qquad \textbf{Equation 2.15}$$

where α is an empirical parameter and ρ is the dislocation density. The parameter α varies from 0.05 to 1.2 [9, 22, 27].

In case of work hardening the metal is strengthen by the accumulation of dislocations, which are generated by plastic deformation. Metals therefore become harder/stronger when they are plastically deformed, hence the name work hardening.

Dislocation strengthening is affected at increasing temperature via recovery and recrystallization. Recovery is the term for the combined processes of (i) annihilation of dislocations of opposite signs acc. to Fig. 2.19(a)-(b), (ii) annihilation of single dislocations by migration to grain boundaries and (iii) rearrangement of dislocations of similar signs into polygonized structures acc. to Fig. 2.19(b)-(c). A polygonized dislocation structure is a low energy structure where dislocations are arranged into relatively stable arrays.

Recovery reduces the mechanism of dislocation strengthening due to that recovery reduces the dislocation density. Recovery is a time dependent process that leads to irreversible yield strength loss. The rate of recovery depends on the temperature and on the density of pinning points for dislocation movements. It is possible to reduce the rate of recovery via precipitates of a second phase, which can pin dislocations and prevent them from moving.

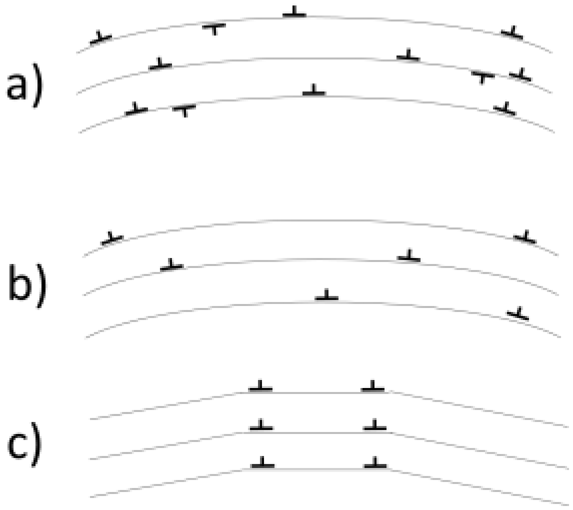

Figure 2.19 *Strained lattice showing slip planes as lines and dislocations (a) before recovery, (b) after annihilation and (c) after polygonization*

Recrystallization is the formation of new grains, with the same phase as the parent phase, in cold worked or strained metals. Recrystallization results in roughly equi-axed grains with a low dislocation density. Recrystallization is a slower process than recovery and typically requires a higher temperature to start. The two processes can interact, since recovery affect the dislocation density, which constitutes the driving force for recrystallization. Recrystallization reduces the mechanism of dislocation strengthening since recrystallization reduces the dislocation density. Recrystallization can also affect the contribution of grain boundary strengthening, if the new grains are of a different size than the parent grains. Recrystallization is a time dependent process that leads to an irreversible yield strength loss. The rate of recrystallization depends on the temperature and the strain level in the metal.

2.2.4.5 Precipitates

A precipitate is a particle of a second phase, β, inside a host lattice, phase α. The strengthening mechanism of precipitates originates from small precipitates that are located on the slip plane of a dislocation and that act as obstacles, or pinning points for dislocations. The dislocation will need extra force to bypass by the precipitate, which reduces the dislocation mobility.

The strength contribution of precipitates depends on the volume fraction of precipitates in the lattice, the precipitate size, the precipitate strength and the interface between the precipitate and the matrix. There are several expressions for calculating precipitation strengthening. One of the most common expressions used for steel is the Orowan-Ashby relationship [28]:

$$\sigma_p = \left(\frac{0.538Gbf^{1/2}}{d_p}\right) ln\left(\frac{d_p}{2b}\right), \qquad \textbf{Equation 2.16}$$

where f is the volume fraction of precipitate phase and d_p is the diameter of the precipitates. This expression was originally derived for incoherent particles, but has shown good correlation also to coherent particles in steel [28].

There are three major mechanisms by which a dislocation can bypass a precipitate; (i) particle cutting (shearing), (ii) local climbing and (iii) Orowan looping [29].

i. Dislocation bypass of precipitates via cutting means that the dislocation travels through the precipitate. Dislocation cutting takes place when the precipitate is soft or small and has a slip plane which fits to the matrix slip plane. The strengthening effect of cutting is commonly called chemical hardening. The increase in force that is needed for the dislocation to cut the precipitate origins from two different phenomena: (i) the particle/matrix interface area is increased by the cutting of the particle according to Fig. 2.20, and/or (ii) an anti-phase boundary or a stacking fault is created inside the precipitate by the dislocation passage. A different lattice friction within precipitate will also affect the cutting process.

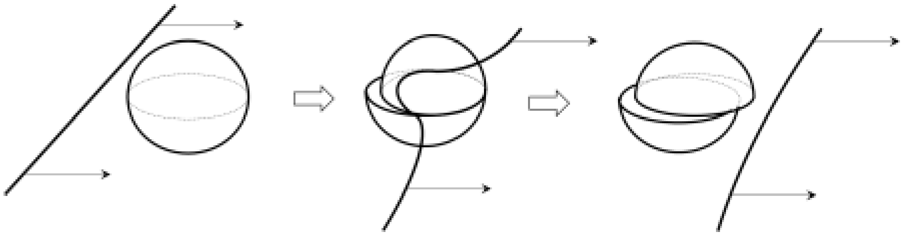

Figure 2.20 *Dislocation passage via cutting, redrawn after [29]*

ii. Dislocation bypass of precipitates via local climb means that the section of the dislocation that is closest to the precipitate moves out of the slip plane, by climb, and surmounts the precipitate as illustrated in Fig. 2.21 [30]. Climb mainly takes place at elevated temperatures and is discussed in more detail later in the section.

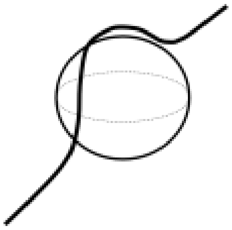

Figure 2.21 *Bypassing of particle via local climb, redrawn after [29]*

iii. The process of Orowan looping begins with the dislocation bowing around a precipitate in the slip plane. As the bowing of the dislocation around the precipitate increases the dislocation can finally leave a closed loop behind [31] as illustrated in Fig 2.22. Orowan looping takes place when the slip plane of the matrix is not extended into the precipitate and when the precipitate is too hard to cut.

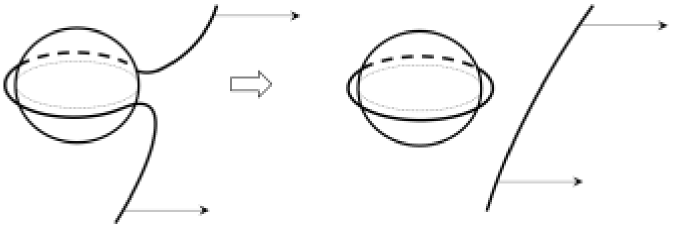

Figure 2.22 *Orowan looping around a precipitate, redrawn after [29].*

The strengthening effect of Orowan looping stems from the increase in dislocation line length from the bowing itself, and from the remaining loop around the precipitates. Orowan looping can therefore be said to lead to localized dislocation strengthening.

Precipitation strengthening is affected at increased temperature by the presence of vacancies and by the coarsening of precipitates. An increased density of vacancies in the lattice reduces the effectiveness of precipitation strengthening since vacancies make dislocation climb possible [30]. A vacancy is a point defect, consisting of one vacant lattice site. The density of vacancies in a metal lattice is increased at elevated temperature according to [15]:

$$X_V^e = exp\left(\frac{-\Delta G_V}{RT}\right), \qquad \textbf{Equation 2.17}$$

where X_V^e is the mole fraction of vacancies, ΔG_V is the formation energy of vacancies and R is the universal gas constant.

Dislocation climb is a time-dependent process that can lead to both reversible and irreversible yield strength loss. If dislocation climb leads to recovery, the yield strength loss becomes permanent. However, dislocation climb as a mechanism to bypass an obstacle is reversibly dependent on the temperature since the number of vacancies in the lattice is reversible with temperature, and will reduce when the temperature is reduced. The rate of dislocation climb depends on the temperature, since the temperature affects the density of vacancies and the diffusional jump frequency.

Coarsening of precipitates leads to a reduction in the number density of precipitates and to larger precipitate sizes. Coarsening of precipitates is accelerated for precipitates when

(i) the solute atoms (from which the precipitate form) have high solubility in the matrix, (ii) the interface energy between matrix and precipitate is high and/or (iii) the diffusivity of the solute atoms from the matrix to the precipitate is high. Coarsening of precipitates leads to a reduction of the precipitate strengthening, since a reduced number density of precipitates implies increased pinning distance, L.

Precipitate coarsening is a time dependent process that leads to irreversible yield strength loss. The rate of precipitate coarsening can be controlled via alloy design to achieve a thermally stable dispersion of precipitates based on precipitate elements that have low solubility in the matrix of the metal, precipitates that have a low interface energy to the matrix and precipitate elements with low diffusivity in the matrix.

2.2.5 Creep

Creep is the time-dependent and permanent deformation of a material, at a stress, which is lower than the yield stress. Creep becomes important at temperature of $0.4T_m$, in which T_m is the melting temperature, for metals. Elastic and plastic deformation, as discussed in section 2.2.2, are the time independent responses to mechanical loading, whereas creep can be described as the viscoplastic, time-dependent response to loading. Section 2.2.5 (with the exception of 2.2.5.4) is mainly based on the book by F.R.N. Nabarro [32].

2.2.5.1 Stages of creep

Creep can be divided into three different regions; (i) primary creep, (ii) secondary creep and (iii) tertiary creep, as illustrated in Fig. 2.23.

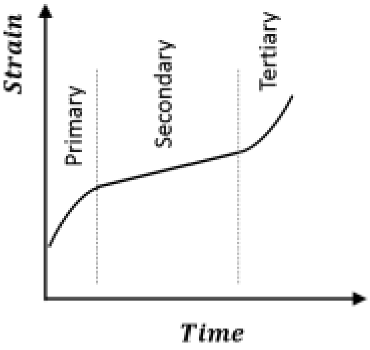

Figure 2.23 *The three stages of creep in metals. The time scale depends on the stress and the temperature and can be measured in years.*

Primary creep is the first stage of creep. Primary creep is characterized by an initially high strain rate, which decreases with increasing time. When the strain rate stabilizes, at the minimum rate, the secondary creep stage has begun. The secondary creep stage is characterized by nearly constant strain rate (at constant temperature and stress) and secondary creep is therefore commonly referred to as steady-state creep. Creep parameters are usually extracted from the secondary creep stage. Tertiary creep is the last stage of creep. Tertiary creep is characterized by increasing strain rate and void formation followed by fracture of the material.

The creep rate of a material depends on the temperature, the loading level and the creep stage. Higher temperatures and higher load levels typically result in higher strain rates. Expressions for the creep rate are given in section 2.2.5.3.

2.2.5.2 Mechanisms of creep

The microstructural processes that cause creep are commonly referred to as mechanisms of creep [33]. The main mechanisms of creep are (i) dislocation movements, (ii) diffusion, (iii) grain boundary sliding and (iv) recrystallization. The time scale and the temperature for these four types of creeps are different.

The creep mechanisms can be summarized into so called deformation mechanisms maps. Deformation maps show which creep mechanism is dominant for a specific homologous temperature, T/T_M, (where $T_M$is the melting temperature of the metal), and normalized stress, σ/G, (where G is the shear modulus). Iso-strain rates lines are represented in the maps. Fig. 2.24, shows a general sketch of a deformation mechanism map for stainless 316 steel.

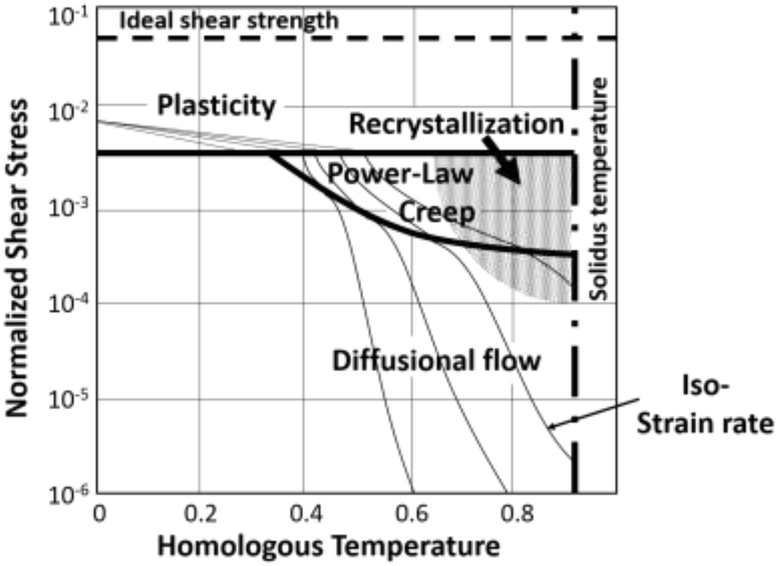

Figure 2.24 *Schematic representation of a deformation mechanism map of stainless 316 steel redrawn after [34].*

2.2.5.2.1 Dislocation movements

Dislocation creep takes place due to increased dislocation mobility at increased temperatures, according to all processes discussed in section 2.2.4, since the thermal energy helps the dislocations to overcome obstacles. Dislocation creep is time-dependent because the bypass mechanisms are time dependent. Dislocation creep can be reduced via every microstructural feature that exerts a strong pinning effect on dislocations at elevated temperatures. A common approach to create temperature resistant metals is to create a fine dispersion of thermally stable precipitates [35]. Also solid solution strengthening can be utilized to reduce dislocation creep.

2.2.5.2.2 Diffusion

Diffusion assisted creep takes place via the movement of vacancies. When vacancies move, the atoms in the lattice move. Diffusion assisted creep is increased at elevated temperature due to increased diffusivity and increased number of vacancies at elevated temperatures, according to Eq. 2.13 and Eq. 2.17. The diffusive flow of vacancies results in deposition of atoms at the grain boundaries. The atoms deposit at the grain boundaries in order to relax the stress in the metal by changing the shape of the grain. Diffusion assisted creep can be divided into two types depending on the path of the diffusive flow; (i) Nabarro-Herring creep, during which diffusion occurs through the lattice and (ii) Coble creep during which diffusion occurs via grain boundaries.

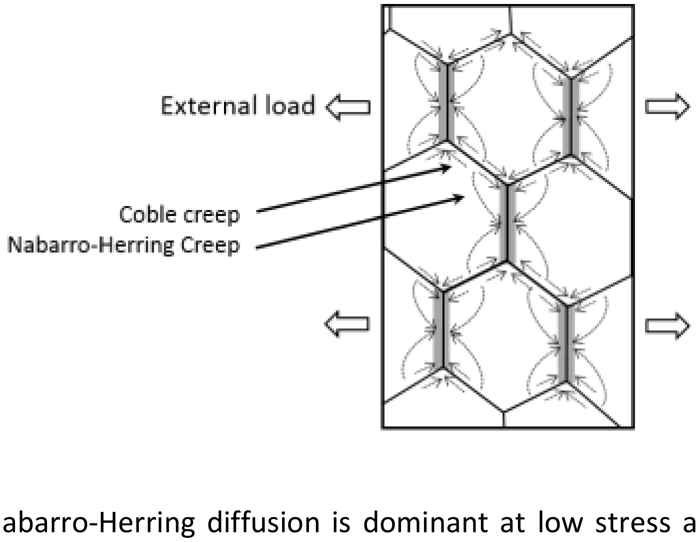

Figure 2.25 *Diffusive creep. Grey areas symbolize regions where atoms deposit.*

Nabarro-Herring diffusion is dominant at low stress and high temperatures and Coble creep (grain boundary diffusion) is increased by small grain sizes in a material. The most common approach to minimize diffusional creep is to increase the grain size, in order to reduce Coble creep.

2.2.5.2.3 Grain boundary sliding

Creep via grain boundary sliding takes place via sliding of individual grains past each other, along the grain boundaries. When a polycrystalline material is externally loaded local stress concentrations form at grain boundaries. Grain boundary sliding takes place because of the bonding strength at the grain boundaries being lower than the bonding strength in the grain interior. Furthermore, the local stress concentrations can result in local plastic strain of the boundary regions, at loads that are smaller than required to deform the metal at ambient temperature. Creep via grain boundary sliding can be reduced by large grain sizes. Metals with large grains have lower density of grain boundaries which can slide. However, creep properties due to grain boundary sliding also depend on the so called grain aspect ratio (GAR). GAR is the ratio of grain dimension parallel to the tensile stress direction and the grain dimension perpendicular to the tensile stress direction. Creep strength is increased by high GAR.

2.2.5.2.4 Recrystallization

Dynamic recrystallization may take place during creep at relatively high strain rates and temperatures [36]. Recrystallization takes place at higher temperatures than relevant for this thesis and is therefore not discussed more in detail in this thesis.

2.2.5.3 Expressions for creep

The rate of creep in metals depends on the stress level, the temperature and time. In addition to these three parameters, the creep rate also depends on the microstructure of the metal and the creep stage. There are therefore many models for describing creep. During the design of engineering components primary and secondary creep stages are often the stages of most interest. Therefore are, as mentioned in section 2.2.5.1, creep characteristics of metals commonly taken from the secondary, steady-state creep region. The creep mechanisms of secondary creep can vary. However most models be generalized according to [37-38]:

$$\dot{\varepsilon} = A\frac{DGb}{kT}\left(\frac{b}{d_g}\right)^p\left(\frac{\sigma}{G}\right)^n, \qquad \textbf{Equation 2.18}$$

where A is a constant, D is the diffusivity (as given by Eq. 2.15), T is the absolute temperature, σ is the applied stress and n and p are exponents of stress and grain size respectively. Equation 2.18 is mainly used for describing creep that is related to the grain size of a metal.

Creep via grain boundary sliding is described by p=2 and n=2 and using the lattice diffusivity of the metal for D [39].

Diffusion assisted Nabarro-Herring creep is described by p=2 and n=1 and using the lattice diffusivity of the metal for D [40-41].

Diffusion assisted Coble creep is described by p=3 and n=1 and using the grain boundary diffusivity of the metal for D [42].

For creep mechanisms that are based on dislocation movements, the dependence on grain size is not relevant (p=0), and secondary creep is commonly modelled according to:

$$\dot{\varepsilon} = A_N \sigma^n \exp(-\frac{Q_C}{RT}), \qquad \textbf{Equation 2.19}$$

where A_N is a constant, n is called the Norton exponent (stress exponent) and Q_C is the activation energy for the creep. Dislocation creep in pure metals is commonly described by n≈5 [38].

2.2.5.4 Measurement of creep

When a metal specimen is externally loaded at an elevated temperature the metal undergoes creep if the load and temperature are sufficiently high.

2.2.5.4.1 Uniaxial creep measurement

Uni-axial creep measurements are performed by monitoring the length of a material specimen while the specimen is subjected to temperature and uni-axial loading. There are two main methods for uni-axial creep testing, (i) measurement at constant load and (ii) measurement at constant stress. The measured creep life is shorter in the constant load test, since the stress in the material increases from the area reduction of the test specimen. Before a uni-axial creep measurement starts, the unloaded test specimen is heated to the test temperature and the initial gauge length is measured. The specimen is thereafter loaded (quickly but without shock) and the extension of sample length is measured at a frequent intervals during the remainder of the test. The test duration of a uni-axial creep test is commonly 2000-10000 hours and the test is typically performed on specimens of several centimetres in length.

2.2.5.4.2 Indentation creep measurement

This section is mainly based on Ref. [43]. When an indenter is pressed into a material, it penetrates the material first by elastic and plastic deformation. If the loaded indenter is allowed to reside on the material it will continue to penetrate the material via creep.

Indentation creep tests are done with a fine scale indenter that is pressed into the test specimen, while the indent displacement is continuously monitored. Indentation creep tests can be performed using constant load, constant strain rate, constant depth or constant rate of loading. The most common method is constant-load testing. The test duration of indentation creep test is commonly several minutes and the test can be performed on specimens that are measured in millimetres or smaller.

Within the research presented in this thesis we use indentation creep to compare the creep behaviour of different fastener steels. This comparison is based on the report that indentation creep can be used to rank different materials to each other for a certain given temperature and load [43]. We point out that at present there is no accepted, validated method of analysing and interpreting indentation creep data. Indentation creep measurement methods have been investigated since 1960 [44-45]. It has been shown that several materials, including several metals, show good correlation between indentation creep data and traditional uni-axial creep data when described via a steady-state power law (Eq. 2.19) [46-49]. In the next section, the theory is presented that led to the development of the indentation technique for creep measurements.

The link between indentation creep measurements and steady state power law creep

During an indentation experiment, stress and strain fields are generated in the deformed zone under the indenter. The deformed zone under the indenter has an approximately hemispherical shape. The theoretical arguments for using indentation measurements too measure creep is based on the relation between the size of the deformed zone and the depth of the indent

In 1970 Johnson [50] suggested that during indentation, the tip of the indenter is encased in a core, according to Fig. 2.26. Inside the core the pressure is hydrostatic. Since there are no shear stresses, and no chemical-potential gradients in the hydrostatic core, creep does not take place within the hydrostatic core. Outside the hydrostatic core there is a plastic-elastic hemispherical zone of a certain radius. Within the elastic-plastic hemisphere the stress field ranges from high stresses, in the vicinity of the hydrostatic core, to low stresses as the distance from the hydrostatic core is increased. Indentation creep is assumed to take place within this elastic-plastic zone. Creep results in an expansion of the elastic-plastic zone (the radius of the elastic-plastic zone increases) which generates an expansion of the hydrostatic core as well. Creep therefore results in further penetration of the indenter into the material.

When indentation experiments are performed with equipment that can monitor the indent depth (the displacement) it is therefore possible to measure the evolution of the material creep within the elastic-plastic hemisphere under the indenter of the tested.

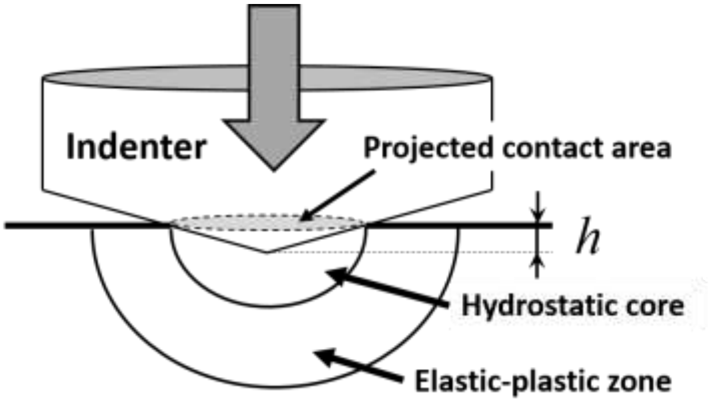

Figure 2.26 *Schematic representation of the hydrostatic core and elastic-plastic zone under an indenter, re-drawn after [33]*

The conversion of indentation displacement measurement data into creep is performed in three steps; (i) definition of the characteristic stress, (ii) definition of the creep strain rate and (iii) assuming that the creep follows a power law such as Eq. 2.19. Since there is not a single value of the stress in the material under the indenter, a characteristic stress must be defined. The characteristic value of the stress is commonly defined in a similar manner as hardness is defined; the applied load, F, is divided by the cross section area of the indenter at the depth of the indent (called the projected contact area, see Fig. 2.26), A_p, rather than the actual contact surface area:

$$\sigma_C = \frac{F}{A_p} \qquad \text{Equation 2.20}$$

The projected area is related to the indent depth via the contact depth, h_c which is the depth of the indenter in contact with the sample under load according to [51]:

$$h_c = h_{max} - k' \frac{P_{max}}{S} \ , \qquad \text{Equation 2.21}$$

where S is the contact stiffness, P_{max} and h_{max} are the maximum applied load and the penetration depth at maximum load respectively and k' is a constant that depends on the geometry of the indenter. Oliver and Pharr [52] derived the method to derive S from the indentation measurement data, and the projected contact area of a Berkowitz indenter (such as used within the research of this PhD thesis) is derived to be $A_p=24{,}56h_c^2$ [53].

The strain rate during indentation experiments is defined by Mayo and Nix [54] as:

$$\dot{\varepsilon} = \frac{1}{h}\frac{dh}{dt} \qquad \text{Equation 2.22}$$

If the time-dependent plastic deformation of the material, as measured by the displacement of the indenter, is generated by power-law creep, Eq. 2.19 applies.

The measured displacement is thereafter plotted as a function of time, according to Fig. 2.27. The creep parameters can be extracted by fitting Eq. 2.19 to the data.

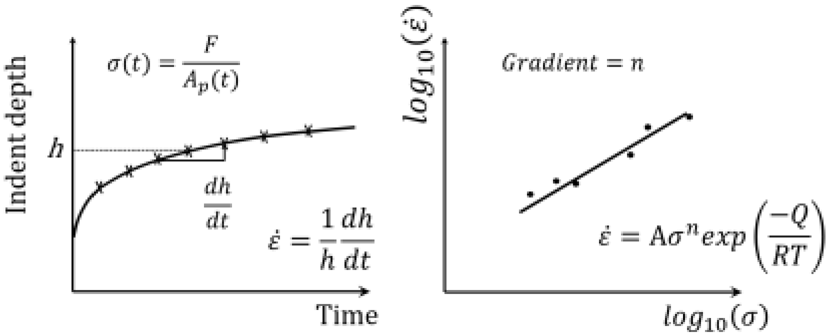

Figure 2.27 *Creep parameters from indentation measurement*

2.3 Precipitation strengthening of Martensite

2.3.1 Introduction

Martensite is the strongest and hardest microstructural constituent of steel. Tempered martensite combines high strength with good toughness and is therefore the key microstructure for high strength fasteners. New fastener steels have been developed which are based on precipitation strengthening of the martensite via alloy carbides, to increase the strength and the resistance to hydrogen related damage of the fastener. These improvements of properties are based on a fine dispersion of alloy carbide-precipitates, which act like pinning points for dislocations and hinder dislocation motion. A clear understanding of the relation between the microstructure, the strength and the processing conditions that are needed to form alloy carbides in martensite is essential for the development of fasteners out of these steels.

The formation, crystallography, and microstructure of martensite are described in next two sections. The hardening mechanisms that contribute to the strength of martensite are discussed in section 2.3.4. Section 2.3.5 describes the changes that take place in the microstructure during tempering of martensite. Section 2.3.6 to 2.3.8 discuss the thermodynamics and kinetics of the nucleation, growth and coarsening of precipitates and section 2.3.9 describes the specific details related to the thermodynamics of the nucleation and growth of TiC in martensite. The main content of sections 2.3.2-2.2.5 is based on the book by Olsen and Owen [13] and the main content of section 2.3.9 is based on the book by Porter and Easterling [15]

2.3.2 Formation of martensite in steel

Steel is iron with up to 2.14wt% carbon, and usually some other alloying elements. Steel consists of an iron lattice with carbon atoms that are located at interstitial positions, dislocations, interfaces or in carbides. The iron lattice can – at ambient temperatures – be ordered in two different lattice structures under equilibrium conditions: (i) Body-centered-cubic (BCC) which is referred to as ferrite (α-iron at low temperatures and δ-ferrite closer to the melting temperature) and (ii) face-centered-cubic (FCC), which is referred to as austenite or ɣ-iron. Figure 2.28 shows the iron-carbon phase diagram, which shows the equilibrium phases as a function of temperature and carbon concentration. The Fe-C diagram is commonly shown with the meta-stable phase of cementite (Fe_3C). The maximum solubility of carbon in the austenite is approximately 100 times higher than in ferrite. Austenite can dissolve slightly more than 2 wt% of carbon, whereas ferrite only can dissolve up to 0.02wt% carbon (depending on temperature). The higher solubility of carbon in austenite than in ferrite makes it possibility to form a martensitic microstructure in carbon steels.

Martensite is created via a rapid cooling from the austenite range (high temperature). This rapid cooling is referred to as “quenching”. At the high temperature, all carbon atoms can be in solid solution, due to the higher solubility of carbon in austenite. Quenching of austenite transforms the FCC structure into the BCC (or BCT as will be explained in the next section) structure. As the cooling is performed rapidly, there is no time for the carbon atoms to diffuse and form carbides. The carbon atoms will therefore remain in the positions of the former austenite phase (FCC) through the transformation from FCC to BCC structure. The carbon atoms become trapped in the interstitial positions of the parent FCC phase.

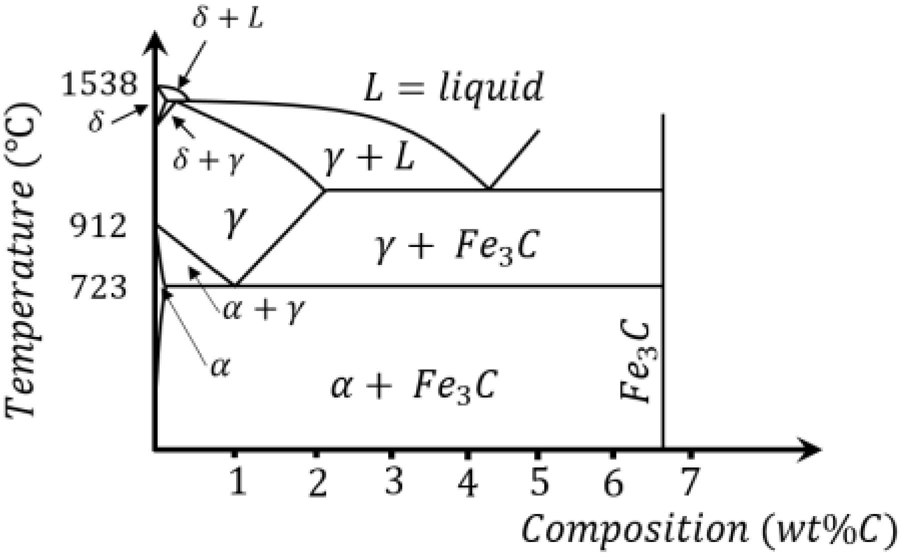

Figure 2.28 *The Fe-C phase diagram showing the phases of ferrite (α and δ), austenite (γ). Fe_3C and liquid (L)*

The exact mechanism behind the nucleation of martensite is not yet fully clarified. However, once the nucleation barrier is overcome, the martensite crystals grow rapidly (at almost the velocity of sound in steel) until they hit an obstacle, such as a former austenite grain boundary. In 1924 Bain proposed that the martensite transformation is a shear deformation, in which the FCC structure is transformed into BCC. Figure 2.29 shows the crystallographic relationship between the FCC and the BCC structures. The BCC and FCC crystal structures are related by rotating the horizontal axes, x and y to x’ and y’ around the vertical (z) axis of the parent FCC cell and by expanding the horizontal axes [55].

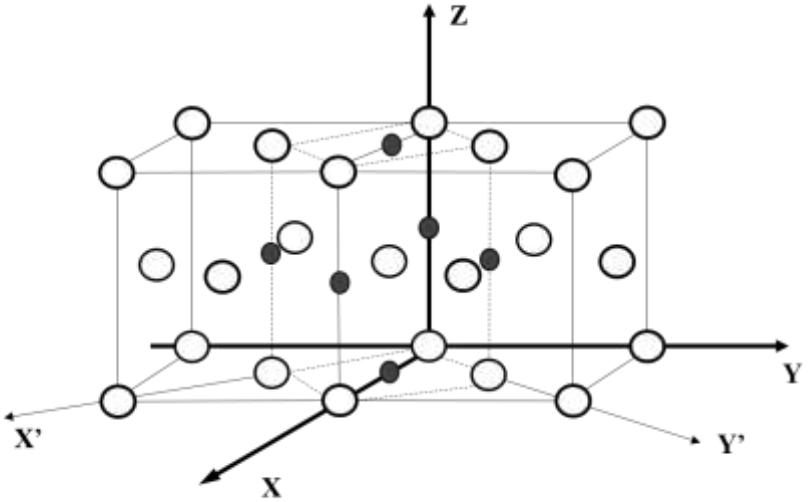

Figure 2.29 *Bain model of the FCC-to-BCC transformation. Iron atoms are shown as white circles and the positions where carbon can be trapped in the resulting BCC structure are shown as dark grey circle*

The Bain model predicts that carbon atoms will be trapped in positions on the vertical axis of the BCC unit cell of ferrite, turning it into a BCT unit cell (Body Centered Tetragonal). Later research has, however, shown that the tetragonality of the BCT cell only appears in martensite that contains more than 0,18 wt.%C (at RT). Martensite that contains less carbon remains cubic [56]. The Bain model has not been experimentally confirmed and cannot fully describe all the details of martensite transformation. However, the model describes the general mechanism of martensite transformation in a concise way.

The martensite transformation is accomplished by a crystallographic misfit between the growing martensite and the parent austenite lattice. The misfit results in high shear stresses at the interface of the growing martensite crystals. Dislocations are formed at the growing interface to accommodate for these stresses. A microstructure that fully consists of martensite, therefore contains a high density of dislocations.

The cooling rate that is required to avoid the formation of ferrite and bainite, and to form martensite depends on the chemical composition of the steel and the grain size of the parent austenite phase. Steels that allow for a slow cooling rate, and yet achieve a fully martensitic microstructure, are said to have good hardenability.

2.3.3 Crystallography of martensite

Martensite can exhibit several types of crystallographic aspects. These crystallographic aspects depend on the chemical composition of the steel and the transformation process. The most general classification is the differentiation between plate martensite and lath martensite. Steel with a carbon concentration below 0.4 wt% typically form lath martensite whereas steel with higher carbon concentration form plate martensite [57-58]. The carbon concentration of high-strength fastener steels range from 0.15 wt% to 0.55 wt% [5]. This makes lath martensite the dominant martensite type found in engine fasteners and the scope of this thesis therefore covers lath martensite. This thesis therefore does not cover the formation mechanism and the details about twinned martensite plates, although some of the fastener steels may contain small fractions of this microstructure type.

The microstructure of lath martensite can be described in a hierarchical manner. The largest constituent is the parent austenite grain structure. A single austenite grain is divided into packets, which in turn are sub-divided into blocks. Each block is built up of more or less parallel laths, according to Fig. 2.30 [59].

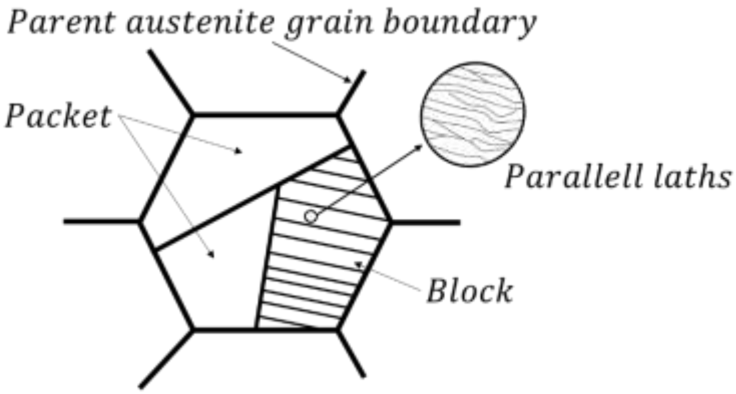

Figure 2.30 *Microstructure of martensite showing former austenite grain boundary, packets, blocks and laths [59].*

The formation of martensite take place along a so called habit plane of the parent austenite phase [60]. A habit plane is a plane among which certain phenomena such as twinning can occur. The habit plane is a crystallographic common plane that is common to both the parent austenite and the martensite and that remains intact during the martensite transformation. There is a special crystallographic orientation relationship (OR) between the parent austenite grain and the product martensite.

Recent investigations by Morito et al have shown that the orientation relationship between the martensite and the former austenite follows a near Kurdjumov-Sachs (K-S) OR, [59, 61], which deviates with a few degrees from the Nishiyama-Wasserman (N-W) OR. There are 24 and 12 different variants of the KN’ and NW orientation relationships, respectively. This means that –for the KS OR – there are 24 different combinations of parallel crystallographic planes and parallel crystallographic directions between the FCC and the BCC lattices.

The possible misorientations between different crystallographic variants of the KS OR are 10.53˚, 14.88 ˚, 20.61˚, 21.06˚, 47.11˚, 49.47˚, 50.51˚, 51.73˚, 57.21˚ or 60.00˚ [62]. Morito et al. furthermore measured that the packets in martensite in low carbon and alloy steel contain blocks made of six of the ten possible variants. The reason why only 6 out of 10 possible variants form is not clear. The misorientation between martensite blocks ranges from 10.53° to 60°, according to the variants described above. The block can therefore be considered as the smallest effective 'grain' in lath martensite [63].The individual blocks contain parallel laths. The parallel laths within one block are of the same variant. In case of low carbon steels, the block can be further divided into two groups (sub-blocks) of laths of two variants with the misorientation of about 10° [59]. The individual laths of martensite are separated by walls of entangled dislocations at a distance of approx. 200 nm [64]. The misorientation between neighbouring laths is only a few degrees.

2.3.4 Strength of martensite

Solid solution strengthening, dislocation strengthening and grain size strengthening are commonly listed as the main strengthening components of martensite [57]. However, also precipitation strengthening via alloy carbides and/or small iron carbides can add to the total strength of martensite.

2.3.4.1 Solid solution strengthening effect of carbon

Martensite can be considered as a ferrite matrix that is super-saturated with carbon atoms. The carbon atoms are located at interstitial octahedral positions of the BCC/BCT lattice or are segregated into lattice defects. Recent investigations have shown that after quenching only approx. 0.02wt% of the carbon atoms are located in true interstitial solid solution in the martensite matrix [65]. The majority of the carbon atoms are thus segregating to lath boundaries and dislocations during quenching. The segregated carbon atoms have however been shown to contribute to the strength of as-quenched martensite to the same extent as true interstitial carbon atoms. The solid solution strengthening of carbon in martensite can be expressed according to [57]:

$$\sigma_{ss}(MPa) = 1720 \cdot C_c^{1/2}, \qquad \textbf{Equation 2.23}$$

where $C_c$is the carbon concentration given in wt.%. The carbon concentration of the steel furthermore influences the crystallography and the dislocation density of the martensite, as higher carbon concentration results in smaller packet and block sizes [57, 59] and higher dislocation density [66].

2.3.4.2 Dislocation strengthening

The martensite formation results in the creation of a high dislocation density at the edge of each growing martensite lath. This high dislocation density will contribute to the strength of martensite according to Eq. 2.15:

$$\sigma_d = M\alpha G b \cdot \rho^{1/2}, \qquad \textbf{Equation 2.24}$$

For calculations of dislocation strengthening of martensite the G and b for ferrite are commonly applied. Furthermore, the following values is used for the product $M\alpha = 0.34$ [67]. Table 2.3 lists the typical dislocation density of lath martensite of different carbon concentration measured by TEM [66].

Table 2.3 *Dislocation density of lath martensite in the as-quenched state [66]*

Alloys	**Dislocation density [x10^{14} m^{-2}]**		
	Average	Max	Min
Fe-0.0026C	6.5	6.9	5.5
Fe-0.18C	11.1	13.3	8.9
Fe-0.38C	14.2	16.1	12.4

The influence of carbon concentration on the dislocation density originates from the formation of a Cottrell atmosphere around the dislocation. The carbon atoms segregate to dislocations and reduce the recovery during quenching of the martensite. A higher carbon concentration therefore increases the dislocation density of the martensite in the as-quenched state. Nordstrom [68] and Kehoe et. al [69] therefore suggests that the strengthening effect of segregated carbon in martensite should be calculated via the dislocation density (via dislocation strengthening) and not via solid solution strengthening.

2.3.4.3 Grain boundary strengthening

The transformation of the parent austenite into the smaller martensite blocks add grain boundary strengthening to martensite. The contribution of grain boundary strengthening to martensite can be based on the grain size of the martensite blocks, and is expressed according to Eq. 2.14 [22]:

$$\sigma_{gb} = 17.4 \cdot {d_g}^{-1/2} \qquad \textbf{Equation 2.25}$$

Literature reports that the block size decreases when the carbon concentration in steel increases [59] and that refining of the austenite grain size results in a decrease of the block width and packet size [70].

2.3.5 Tempering of martensite

Directly after quenching the martensite is called virgin martensite. This is the hardest and most brittle state of martensite. Tempering is an isothermal heat treatment of martensite performed to increase the toughness of the steel. Tempering is performed at temperatures which are high enough to allow changes in the martensite microstructure, but below the austenite formation temperature, A_1. The hardness decreases during tempering, but the toughness of the microstructure is significantly increased.

The microstructural changes which takes place in the martensite during tempering have been extensively studied by many experimental techniques and are nicely summarized in [58, 71]. The main processes that take place during tempering of Fe-C martensite are (listed in their order of appearance and/or at higher temperatures); (i) carbon clustering and segregation into lattice defects, (ii) iron carbide precipitation (iii) decomposition of retained austenite, (iv) coarsening of iron carbides, (v) recovery of dislocation structures, and (vi) recrystallization of the martensite into equi-axed ferrite.

The processes may overlap and each process may individually be affected by alloy additions to steel. Furthermore, each of these processes has a direct effect on the hardening mechanisms of martensite.

2.3.5.1 Carbon clustering and segregation

The first process that takes place during the tempering of martensite involves carbon segregation and the formation of carbon clusters. This process is sometimes called martensite ageing. Segregation is the redistribution of carbon atoms from interstitial positions to lower-energy sites, such as individual dislocations, vacancies and lath boundaries.

Carbon clustering is the accumulation of carbon atoms into clusters or modulations in the martensite lattice. The driving force for carbon clustering is the reduction of the total elastic energy of the lattice [58]. The carbides which form during later stages of tempering are primarily forming from carbon clusters, and not from segregated carbon atoms [72-73].

2.3.5.2 Iron carbide nucleation and growth

The first type of iron-carbides which form during tempering are so called ε-carbides, which are $Fe_{2.3}C$-particles with a HCP crystal structure. The formation of ε-carbides is homogeneous in the lattice and is commonly called the first stage of tempering, even though it takes place after carbon clustering and segregation. The first stage of tempering proceeds during a few minutes of tempering at 100-200°C, but can also start during auto-tempering: tempering that takes place during the quenching. . The shape of ε-carbides have been reported to range from needle-, rod-, lath- to disk-like, depending on the tempering temperature [74]. ε-carbides are metastable transition carbides, which dissolve during the later stages of tempering.

The second type of iron-carbides which form during tempering of martensite is cementite. The formation of cementite is called the third stage (the second stage is discussed later) of tempering and takes place at a high rate at temperatures of 200-300°C. Cementite has the composition Fe_3C and an orthorhombic lattice structure.

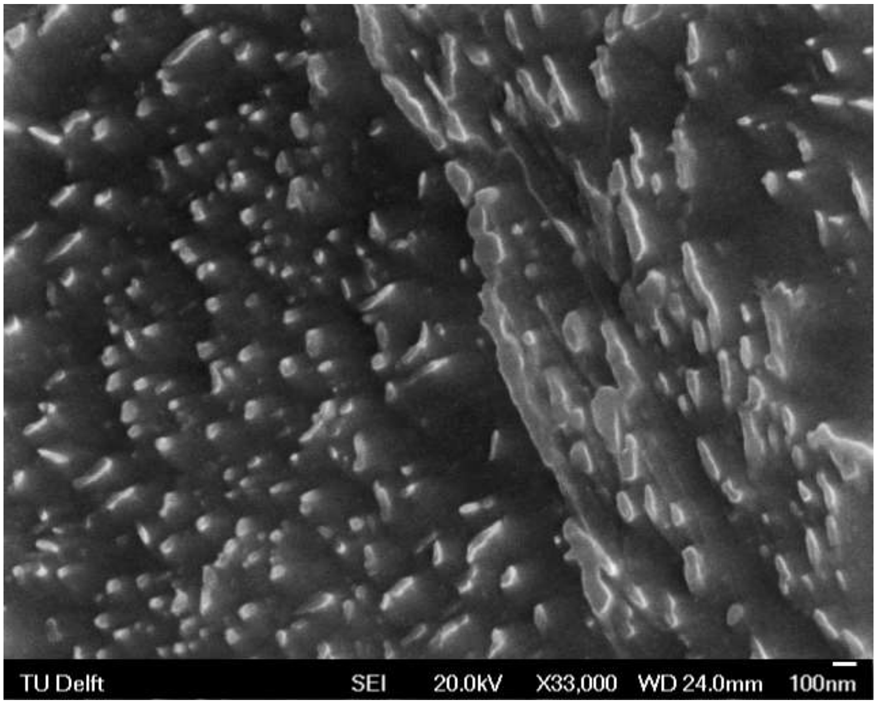

Figure 2.31 *Cementite particles in KNDS4 as observed by SEM on nital etched specimens after 60 minutes of annealing at 550°C*

Cementite nucleates primarily on lath and block boundaries and the initial shape of cementite is needle- or disc-like which evolves into plate or lath shapes [58, 71], as shown in Fig. 2.31. At higher tempering temperatures (400-600°C) the cementite particles will start to become more spherical in shape. Coarsening of cementite take place via Ostwald ripening. The larger particles grow by consuming the smaller particles.

2.3.5.3 Decomposition of retained austenite

Meta-stable austenite can be retained in martensite after quenching. Retained austenite is usually only present in martensitic steels with carbon content above 0.4wt% and is therefore not common in lath martensite. The decomposition of retained austenite takes place at 200-300°C and is commonly called the second stage of tempering since it can take place before cementite formation and growth. Retained austenite is commonly transformed into bainite [58, 71].

2.3.5.4 Dislocation recovery, recrystallization and grain coarsening

Dislocation recovery is generally said to start at temperatures above 400°C. The recovery process of the dislocation structure in martensite is comparable to the process of recovery in cold worked metals. Recovery of martensite result in a reduction of the dislocation density in the martensite.

The degree of recovery depends on the tempering temperature, where higher temperatures typically results in a higher degree of recovery [75]. Recovery is followed by recrystallization. The recrystallization of martensite results in equi-axed ferrite grains. At elevated temperatures recrystallization of martensite can be followed by grain growth. Recrystallization and martensite grain coarsening usually starts at 600-700°C. Recrystallization is slowed down by the pinning of carbides. The processes of recovery/recrystallization/grain growth and cementite coarsening can take place in parallel.

2.3.6 Nucleation of precipitates

Nucleation is the localized formation of a new β-phase, in a parent α-phase. Nucleation starts with the formation of a cluster of the solute atoms (the atoms which make up the β-phase) which form the nucleus of the new β-phase. The classical nucleation theory describes the change in Gibbs free energy, during the nucleation event of one nucleus of β-phase in the host matrix of α-phase, as [15, 76];

$$\Delta G = -V_\beta \Delta g_v + \sum_i A_i \gamma_i + V_\beta \Delta g_s - \Delta g_d\,,$$

Equation 2.26

where V_β is the volume of the new β-phase and Δg_v is the free energy difference, $g^\alpha - g^\beta$, between α-phase and β-phase per unit volume of the β-phase (also called the chemical driving force for nucleation). A_i and γ_i are the area and energy of the i^{th} interface of the nucleus or of the grain boundary of the parent phase that is removed during the nucleation. The product $A_i\gamma_i$ is taken to be negative in case grain boundary area is removed during nucleation. The product $A_i\gamma_i$ is taken to be positive for the new interfaces that are created during nucleation. Δg_s is the strain energy per unit volume of formed β-phase and Δg_d is the change in free energy related to defects in the parent phase, which are annihilated during the nucleation of the β-phase. The nucleation process of the new β-phase is a balance between the negative terms and the positive terms in Eq. 2.26. Nucleation only takes place in case the activation energy, ΔG^*, for nucleation is overcome, see Figure 2.32. This point defines the critical nucleus size, which is generally indicated with the symbol *. Subsequent attachment of atoms to the critical nucleus will reduce the Gibbs free energy of the system.

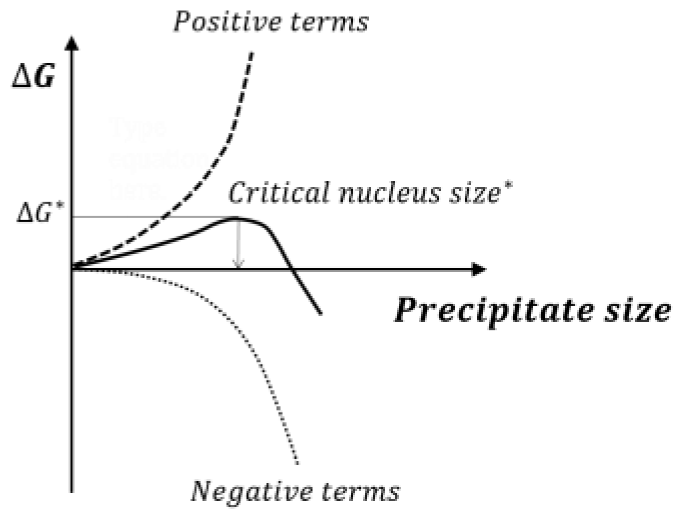

Figure 2.32 *The change in Gibbs free energy (solid line) as a function of nucleus size*

The critical dimensions of the nucleus can be found by differentiation of Eq. 2.26 with respect to the precipitate dimension, equating to zero, and solving the equation for the precipitate dimension. An assumption of the nucleus shape is necessary for this step, as the exact shape of critical nuclei is not known.

2.3.6.1 Driving force for nucleation, $\Delta \boldsymbol{g_v}$

The driving force for the nucleation is the free energy difference between phase α-phase and β-phase per unit volume of the β-phase. For any given temperature there is a maximum concentration of solute atoms that can dissolve into the parent α-phase. This is called the solubility limit of the α-phase. By exceeding this critical concentration, a driving force for nucleation of precipitates of β-phase arises. The solubility of the atoms of the β-phase can be expressed in terms of solubility products. For a carbide precipitate of type M_mC_n (M=metallic, such as Ti, V and Nb etc.) the following relationship is valid [77]:

$$\log K_s = A - \frac{B}{T}, \qquad \textbf{Equation 2.27}$$

where $K_s = [M]^m[C]^n$ is the solubility product and A and B are experimentally determined parameters. [M] and [C] are the atomic percentages or mole fractions of element M and C respectively. The unit of the solubility product therefore depends on the stoichiometric composition of the precipitate phase, and the unit is concentration to the power of $m + n$. In case the solubility limit is exceeded, the solution is said to be supersaturated. The solubility product is a function of temperature, and the driving force for nucleation is therefore also directly dependent on temperature.

2.3.6.2 Interface energy, $\boldsymbol{\gamma_i}$

The interface energy of Eq. 2.26 refers to either the energy of the interface between the precipitate of β-phase and the matrix of the parent α-phase or to the energy of a grain boundary in the parent phase that is removed during the nucleation. The interface between β-phase and the parent α-phase can be divided into three main types; (i) coherent, (ii) semi-coherent and (iii) incoherent, see Fig. 2.33.

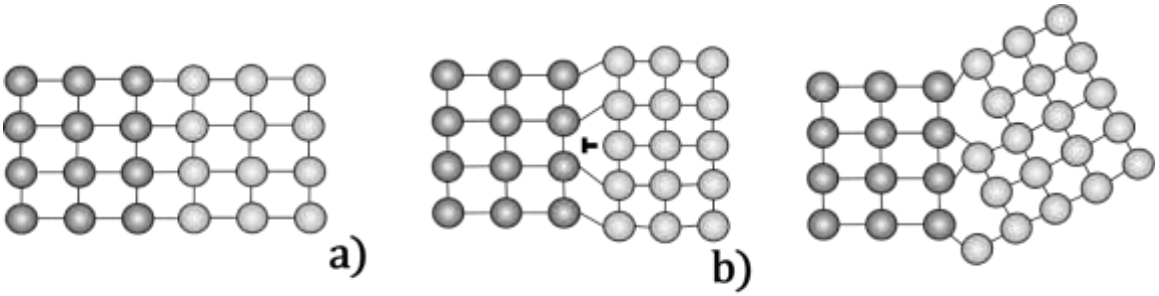

Figure 2.33 *Interfaces between two different phases (grey and white) showing (a) a perfectly coherent interface, (b) a semi-coherent interface and (c) an incoherent interface.*

Coherent interfaces form when the host lattice and precipitate lattice have the same or nearly the same inter-atomic spacing at the position of the interfaces between the two phases. This implies that there is a specific orientation relationship between the crystallographic planes of the two phases. Less than perfect matching of the lattice parameters of coherent interfaces will result in straining of one or both of the lattices. This straining is called coherency strain and is included in the volume strain energy term Δg_s in Eq. 2.26 [78]~~.~~ The energy of a coherent interface is normally in the range of 1-200 mJ/m^2.

Semi-coherent interfaces form when it becomes energetically more favorable to replace a coherent interface with large strains by an interface with misfit dislocations that are periodically spaced to reduce the strain energy. The dislocations form to accommodate the strain, and the interface becomes semi-coherent. The higher the misfit between the two phases, the closer the misfit dislocations will be placed. Similar to coherent interfaces, semi-coherent interfaces are associated to a specific orientation relationship between the two phases. The surface energy of a semi-coherent interface includes the energy of the dislocations which are part of the interface. The energy of semi-coherent interfaces is typically in the range of 200-500 mJ/m^2

Incoherent interfaces arise when there is no atomic fit at the meeting interfaces between the two phases. Incoherent interfaces are not associated to a specific orientation relationship. They are generally associated with high energies, 500-1000 mJ/m^2

2.3.6.3 Misfit strain energy, $\Delta \boldsymbol{g_s}$

The misfit strain energy of Eq. 2.26 refers to the straining of the host lattice around a precipitate. This strain energy is therefore closely linked to the coherency strains and is dependent on the lattice parameter and elastic constants of the β-phase, the α-phase and the temperature of the system.

Misfit strain energies are difficult to measure, but they can be approximated via first-principles calculations [79]. The misfit strain energy is commonly ignored in Eq. 2.26.

2.3.6.4 Defect energy, $\Delta \boldsymbol{g_d}$

The defect energy of Eq. 2.26 refers to the defects in the parent phase α which are annihilated (consumed) due to the nucleation of the new β-phase. Defects that can be annihilated during the nucleation of a new phase are vacancies and (part of) dislocations. The magnitude of Δg_d depends on the type and the dimensions of the defects that are removed by the nucleation.

The defect energies for dislocations can be calculated from the length of the dislocation line which is consumed, and the line energy of the dislocation itself.

2.3.6.5 Homogeneous and heterogeneous nucleation

During homogeneous nucleation the precipitates nucleate within the matrix phase. Truly homogeneous nucleation does not result in any annihilation of defects. However, it may be difficult to experimentally determine if nucleation did or did not involve the removal of a vacancy during nucleation. During homogeneous nucleation there is no site preference, and all the atoms in the host lattice can act as potential nucleation points for the nucleating precipitates. Usually, this results in a uniform distribution of precipitates throughout the host phase. Homogeneous nucleation of spherical precipitates requires precipitates which have the same interface energy in all directions. However, non-spherical nuclei may appear during homogeneous nucleation due to the crystallographic nature of the matrix and precipitating phase. For truly homogeneous nucleation the defect energy term is zero.

During heterogeneous nucleation the precipitates nucleate at grain boundaries, edges or corners, or other defects. Heterogeneous nucleation results in annihilation of defects. Figure 2.34 shows two examples of heterogeneous nucleation. This restricts the number of possible positions for nucleation within the host lattice. Heterogeneous nucleation therefore results in a distribution of precipitates throughout the host phase, similar to the distribution of the defects which the precipitates nucleate on.

During heterogeneous nucleation the precipitates form with the help of defects in the host lattice; so called site preference. Heterogeneous nucleation is therefore linked to the interfaces and the defect energy terms of Eq. 2.26.

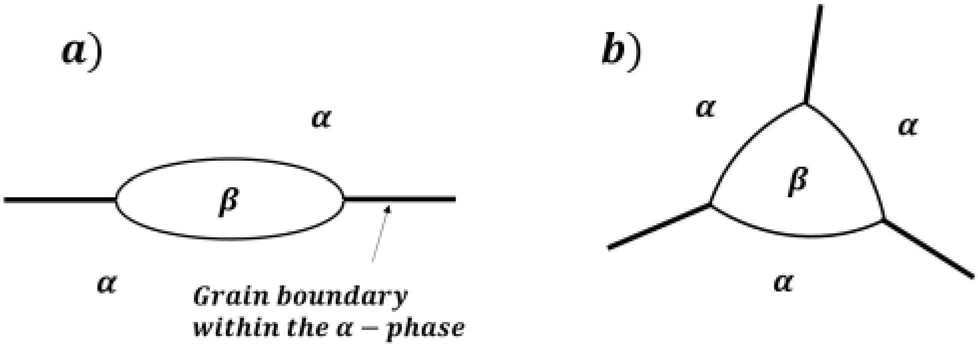

Figure 2.34 *Heterogeneous nucleation at (a) a grain boundary and (b) at a grain edge.*

2.3.6.6 Nucleation rate

Nucleation is a time dependent process. The time-dependent nucleation rate ($m^{-3}s^{-1}$) can be described as [76, 80]:

$$J = NZ\beta^* exp\left(-\frac{\Delta G^*}{k_B T}\right) exp\left(-\frac{\tau}{t}\right), \qquad \textbf{Equation 2.28}$$

where N is the density of potential nucleation sites, Z is the non-equilibrium Zeldovich factor, β^* is the frequency factor (the rate at which single atoms are added to the sub-critical nucleus), ΔG^* is the activation energy for nucleation, T is the absolute temperature at which the nucleation takes place and τ is the incubation time.

The non-equilibrium Zeldovich factor takes into account that when a nucleus reaches the critical size (at the top of the energy barrier in Fig. 2.32) it can either grow or it can dissolve. The general equation for the non-equilibrium Zeldovich factor is commonly described as [81]:

$$Z = \sqrt{\frac{1}{2\pi k_B T}\left(-\frac{\partial^2 \Delta G}{\partial n_a^2}\right)_{n_a^*}}, \qquad \textbf{Equation 2.29}$$

where n_a is the number of atoms in the nucleus and n_a^* is the number of atoms in the critical nucleus.

The frequency factor covers the rate at which single atoms are added to the nucleus. The frequency factor can be described according to [80]:

$$\beta^* = N_j \cdot \Gamma \qquad \textbf{Equation 2.30}$$

where Γ is the atomic jump frequency and N_j is the number of atoms that are within one atomic jump distance to the nuclei (α_j).

If the surface of the nuclei is described as $S*$ and a is the interatomic distance we can approximate:

$$N_j \approx \frac{S^*}{a^2}$$ **Equation 2.31**

The atomic jump frequency Γ can be expressed in terms of the diffusivity of the solute atom according to:

$$\Gamma = \frac{6D}{\alpha_j^2}$$ **Equation 2.32**

The incubation time is given by [80]:

$$\tau = \frac{1}{2Z^2\beta^*}.$$ **Equation 2.33**

The incubation time for nucleation of alloy carbide precipitates in steel can be of the order of seconds or even less (the nucleation of TiC precipitates in the simulations presented in chapter 5 started already during heating up to the isothermal annealing temperature [82]).

2.3.7 Growth and coarsening of precipitates

When the critical nuclei have formed the precipitate will grow by migration of the interface into the host matrix. The growth of a precipitate is highly dependent on the diffusivity of the atoms that form the precipitate phase. The growth mechanism of precipitates can be of three types; (i) diffusion controlled, (ii) interface controlled, or (iii) mixed-mode.

Diffusion controlled growth is governed by the long-range diffusion of solute atoms to the growing precipitate. Interface controlled growth is governed by the rearrangement of the atoms near the interface by short range diffusion. During diffusion controlled growth local equilibrium of the solute atoms will form at the interface of the precipitate. As the attachment of solute atoms to the surface is rapid, the close vicinity of the matrix near the precipitate will be depleted of solute atoms. This depleted zone creates a concentration gradient which will cause diffusion of solute atoms towards the growing precipitate. We give an example for a precipitate of β-phase with equilibrium concentration $C_\beta^{A,eq}$ *of A* atoms, in a matrix of α-phase which is supersaturated $\left(C_{\alpha,0}^{A} > C_{\alpha}^{A,eq}\right)$ in *A*.

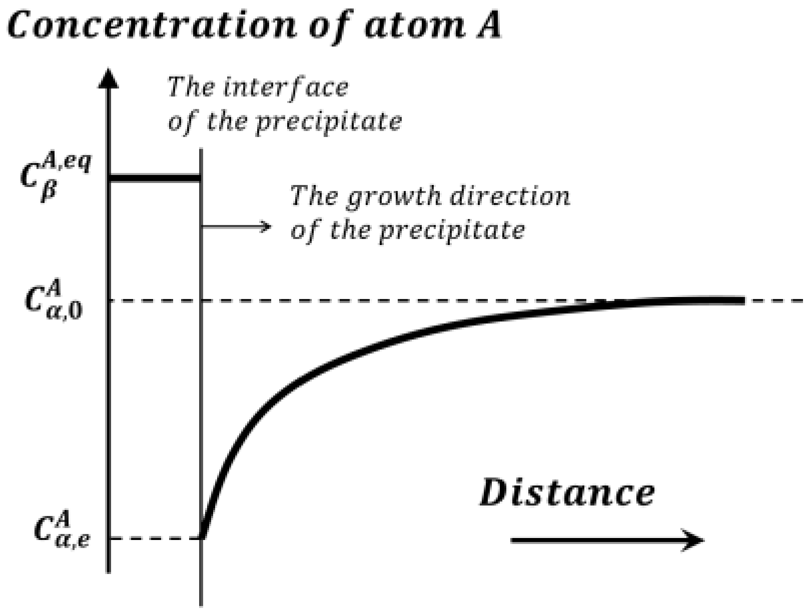

Figure 2.35 *The concentration profile of A atoms showing the equilibrium concentration of A atoms in the precipitate,* $C_{\beta}^{A,eq}$*, the concentration of A atoms in the matrix near the interface of a growing precipitate,* $C_{\alpha,e}^{A}$ *and the concentration of A atoms in the bulk matrix of* α*-phase outside the diffusion filed of the precipitate during diffusion controlled growth.*

Figure 2.35 shows the concentration profile of solute A atoms near the interface of a growing precipitate during diffusion controlled growth. The concentration of A atoms in the bulk matrix of α-phase, outside the diffusion field of the precipitate is $C_{\alpha,0}^{A}$. The concentration of A atoms in the matrix, near the precipitate interface is C_{e}^{A} and the concentration of A atoms in the precipitate β-phase is C_{β}^{A}.

The growth rate, v, of spherical precipitates can be described according to Zener [83]:

$$v = \frac{D}{r_p}\frac{C_{\alpha 0}^{A} - C_{\alpha,e}^{A}}{C_{\beta}^{A} - C_{\alpha,e}^{A}} \ ,$$

Equation 2.34

where D is the diffusivity of the solute atom A in the host matrix of α-phase and $r_p$is radius of the growing precipitate.

For small precipitates this growth rate can be affected by the so called Gibbs-Thompson effect [84]. The Gibbs-Thompson effect describes the influence of a curved interface between precipitate and matrix on the solubility limits of solute atoms in the matrix. A high curvature increases the interface energy, which in turn increases the free energy at the surface. This will increase the solubility limit of the solute atoms. Small precipitates with a high radius of curvature are therefore surrounded by a matrix where the local equilibrium concentration of solute atoms is higher than it is in the surrounding of large precipitates. This reduces the concentration gradient near the surface of small precipitates which reduced reduces the growth rate of the precipitate. Moreover, the Gibbs-Thompson effect enables the dissolution of small precipitates in comparison to large precipitates during coarsening.

2.3.8 The thermodynamics of TiC-precipitate nucleation and growth in steel

Titanium is a carbide forming element, which can be used to create a fine dispersion of precipitates in steel. The carbide which is formed by titanium consists of one carbon atom per titanium atom; TiC. The crystal structure of TiC is of the NaCl type, see Fig. 2.36. The reported lattice parameters of TiC is 0.432 nm [85].

The Baker-Nutting orientation relationship has been observed between TiC and ferrite [86]. TiC precipitates in steel are reported to be fully coherent at small sizes and to grow into semi-coherent discs/platelets at a critical dimension [87-88]. The broad interface of the TiC platelet is parallel to the {100} plane of the ferrite. The lattice parameter of TiC is larger than the inter-atomic spacing of ferrite, and the result is a misfit of approx. 6-7% [79, 88] along the direction of the plate. Normal to the broad interface the misfit is significantly higher. As a result the distance between the mis-fit dislocations becomes 4.2 nm at the diameter of the disk, and 0.82 nm at the edge/height of the disk [87]. The interface energy between small TiC precipitates and ferrite is commonly reported to be in the range of 0.3 J/m^2 [79, 89-92].

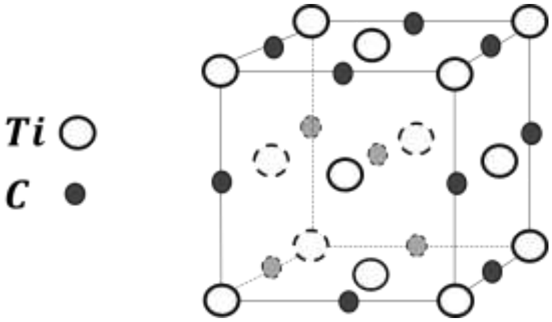

Figure 2.36 *NaCl crystal structure of TiC.*

The nucleation of TiC in steel is heterogeneous and takes place near dislocations [93]. Literature reports that the nucleation rate is enhanced by the strain field which surrounds the dislocations and that the position of nucleation is next to the dislocation. [94]. Experimental studies show that TiC nucleation in martensite requires an isothermal annealing temperature of 500°C or higher [87-88] and calculations of the time dependent nucleation rate, from classical nucleation theory, show that the nucleation rate of TiC in steel at 580°C is up to 10^{19} $m^{-3}s^{-1}$ in case the steel contains a dislocation density of 10^{13} m^{-2} [91].

The solubility of TiC in ferrite is low, but it is possible to fully dissolve TiC in austenite. Figure 2.37 shows a ThermoCalc simulation (TCFE6) of stable equilibrium phase of TiC in KNDS4 steel. TiC is stable up to temperatures of approx. 1250°C.

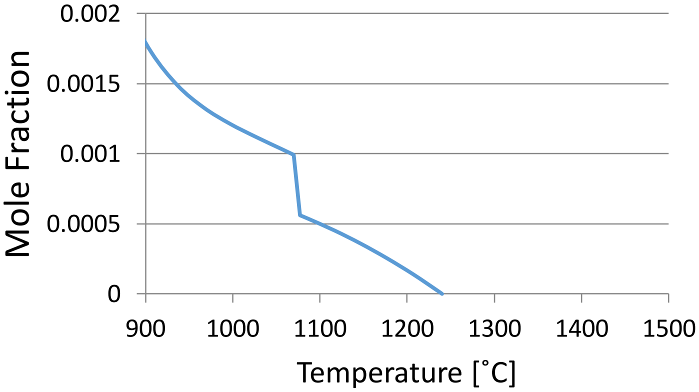

Figure 2.37 *Mole fraction of stable TiC in steel KNDS4, as a function of temperature. Data calculated by ThermoCalc (TCFE6).*

The solubility data for TiC in ferrite is reported to be [77]:

$$\log[Ti][C] = 2.75 - \frac{7000}{T} \text{ (at.\%)}^2 \qquad \textbf{Equation 2.35}$$

This low solubility in ferrite results in a high supersaturation of Ti in ferrite if quenching is done from temperatures where Ti is in solid solution. The driving force for nucleation during subsequent tempering of martensite is therefore high. Literature report values of $\Delta G_v(580°\mathrm{C}) = 3.2x10^9\ \mathrm{J/m^3}$ [91] and $\Delta G_v(0K) = 81.9x10^9\ \mathrm{kJ/mol}$ [79].

The diffusivity of titanium in ferrite follows the general equation for diffusivity:

$$D_{Ti}(T) = D_{0,Ti}\exp\left(-\frac{Q_{D,Ti}}{RT}\right) , \qquad \textbf{Equation 2.36}$$

where the most commonly applied diffusivity data are the values reported by Ogilvie and Moll [95]. Ogilvie and Moll examined Fe-Ti alloys with low Ti concentration to study the interdiffusion data; $D_{0,Ti}$ = 0.315x10^{-3} m^2/s and $Q_{D,Ti}$= 247.7 kJ/mol [95]. This data was measured in polycrystalline ferrite. The tracer diffusion coefficient of Ti in single crystal α-iron have been measured by [96] via the serial sectioning method and established that the temperature dependence of the diffusion coefficient can be described according to:

$$D_{Ti}(T) = 0.21\exp\left(-\frac{293.2\frac{kJ}{mol}}{RT}(1+0.079M^2(T))\right)\mathrm{m^2s^{-1}}, \qquad \textbf{Equation 2.37}$$

where M is the ratio of the spontaneous magnetization (at temperature T) to the saturation magnetization of ferrite. The spontaneous magnetization is given by [97]:

$$M_s(T) = M_0\frac{(1-t)^{\beta}}{(1-\beta\vartheta+A\vartheta^{3/2}-C\vartheta^{7/2})} \qquad \textbf{Equation 2.38}$$

and

$$M_0 = M_1(1-\beta+A-C), \qquad \textbf{Equation 2.39}$$

where $= T/T_c$, T_c is the Curie temperature and the constants $\beta = 0.368$, A=0.110 and C=0.129. Equation 2.37 deviates from a linear Arrhenius relationship, as given in Eq. 2.36, due to the magnetic spin ordering, that is accounted for by the parameter M.

2.3.9 References

[1] E. Eckerman: World history of the automobile, Society of Automotive Engineers, Warrendale, USA, 2001
[2] VDI 2230-1, Systematic calculation of high duty bolted joints – Joints with one cylindrical bolt. VDI-Gesellschaft Entwicklung Konstruktion Vertrieb, Dussledorf, Germany, 2003
[3] G. Toth: Torque and Angle Controlled Tightening Over the Yield Point of a Screw, Chalmers Univeristy of Technology, Gothenburg, Sweden, 2002
[4] Volvo Car Corporation, Design Instructions, PV3-1997, Standards VCC, Gothenburg, Sweden, 1997
[5] ISO898-1, Mechanical properties of fasteners made of carbon steel and alloy steel-Part 1. Fifth edition, Switzerland, 2013
[6] K.-H. Kloos and W. Thomala: Schrauben verbinduingen; Grundlagen, berechnungen, Eigenschaften, Handhabung,. Springer, Berlin Heidelberg, Germany, 2007
[7] DIN EN 10269, Stähle und Nickellegierungen für Befestigungselemente für den Einsatz bei erhöhten und/oder tiefen Temperaturen, Berlin, Germany, 2006
[8] WD. Callister Jr.: Materials Science and Engineering, An introduction. Seventh Ed. John Wiley & Sons, New York, 2007
[9] D. Hull and D.J Bacon: Introduction to dislocations. Fifth Ed. Pergamon, Oxford, UK, 2011
[10] D. Chandrasekaran: Grain size and solid solution strengthening in metals, Royal Institute of Technology, Stockholm, Sweden, 2003
[11] FRN Nabarro: Mater Sci Eng. A 234-236(1997), 67-76
[12] EW. Collings and HL. Geel: Physics of solid solution strengthening. AIME, Plenum Press, New York, USA, 1973
[13] GB. Olson and WS. Owen (Eds.), Martensite, ASM International, Materials Park, Ohio, USA, 1992

[14] T. Gladman: The physical metallurgy of microalloyed steels, The University press, London, UK, 1997
[15] DA. Porter and KE. Easterling: Phase transformations in metals and alloys, Van Norstrand Reinhold, New York, USA, 1981
[16] R. Viswanathan: Damage Mechanisms and Life assessment of High Temperature Components, ASM International, USA, 1989
[17] AH. Cottrell and BA Bilby: Proc. Phys. Soc., A(1949), 49-62
[18] AH. Cottrell: Dislocations and plastic flow in crystals, Clarendon Press, Oxford, UK, 1961
[19] U. Ehrnsten, M. Ivanchenko, V. Nevdacha, Y. Yagodzinskyy, A. Toivonen and H. Hanninen: Proceedings of the 12th international conference on environmental degradation of materials in nuclear power system – water reactors-,. TMS, 2005in Nitrogen
[20] EO. Hall: Proceedings of the Physical SocietyB, 64 (1951), 747-753
[21] NJ. Petch: J. Iron Steel Inst., 174 (1953), 25-28
[22] Y. Han, J. Shi, L. Xu, WQ Cao and H. Dong: Mater. Sci. Eng. A,. 503(2011), 643-651
[23] K. Lucke and K. Detert: Acta Metallurgica., 5(1956) 628-637
[24] JW. Cahn: Acta Metall., 10(1962), 789-798
[25] T. Gladman: Proceedings of the Royal Society of London, Series A, Mathematical and Physical Sciences, 294(1966), 298-309
[26] JE. Bailey and PB. Hirsch: Philos. Mag., 5:53(1960), 485-497
[27] R. Lagneborg and B. Bergman: Metal. Sci., 10(1976), 20-28
[28] T. Gladman: Mater. Sci. Tech., 15(1999), 30-36
[29] DC. Chrzan and JW. Morris, Jr YN. Osetsky, RE. Stoller, SJ. Zinkle: MRS Bulletin., 34(2009), 173-177
[30] R. Lagneborg: Scripta Metall., 7(1973), 605-614
[31] E. Orowan: Symposium on International Stresses, Inst. of Metal, London, UK, 1947
[32] FRN. Nabarro and HL. de Villiers: The physics of creep and creep-resistant alloys, CRC Press, 1995
[33] WB. Li, JL. Henshall, RM. Hooper and KE. Easterling: Acta Metall. Mater., 39(1991), 3099-3110
[34] http://engineering.dartmouth.edu/defmech/
[35] DR. Muzyka, Eds CT Sims and WC Hagel: The Superalloys, John Wiley & Sons, New York, 1972
[36] ME. Kassner: Fundamentals of creep in metals and alloys., Elsevier, 2015
[37] W. Blum, P. Eisenlohr and F. Breutinger: Metall Mater Trans A., 33A(2002). 291-303
[38] ME. Kassner and MT Perez-Prado: Prog. Mater. Sci., 45(2000), 1-102
[39] TG. Langdon: Acta Metall. Mater., 42(1994), 2437-2443
[40] FRN. Nabarro: Report of a Conference on Strength of solids, Physical Society, London, 1948
[41] C. Herring: J. Appl. Phys., 212(1950), 437-445
[42] RL. Coble, J. Appl. Phys., 34(1963), 1679-1682
[43] R. Goodall and TW Clyne: Acta Mater., 54(2006), 5489-5499

[44] TO. Mulhearn and D. Tabor: J. Inst. Metals., 89(1960), 7-12.
[45] AG. Atkins, A. Silverio and D. Tabor: J. Inst. Met., 94(1966), 369-378.
[46] H. Takagi, M. Dao, M. Fujiwara and M. Otsuka: Mater. Trans., 47(2008), 2006-2014
[47] Z-F. Yue, J-S Wan and Z-Z Lu: App. Mathematics and Mechanics., 24(2003), 307-317
[48] M. Fujiwara and M. Otsuka: Mater. Sci. Eng., A319-312(2001), 929-933
[49] PM. Sargent and MF. Ashby: Mater. Sci. Tech., 8(1992), 594-601
[50] KL. Johnson: J. Mech. Phys. Solids., 18(1970), 115–126
[51] GZ. Voyiadjis, AH. Almasri and T. Park: Mech. Res. Com., 37(2010), 307-314
[52] WC. Oliver and GM. Pharr: J. Mater. Res., 7(1992), 1564-1580
[53] X. Li and B. Bhushan: Mater. Characterization., 48(2002), 11-36
[54] MJ. Mayo and WD. Nix: Acta Metall., 36(1988), 2183–2192.
[55] EC. Bain: Transactions of the American Institute of Mining and Metal Engineering., 70(1924), 25-46
[56] L. Xiao, Z. Fan and Z. Jinxiu: Phys. Review B., 52(1995), 9970-9978
[57] G. Krauss: Mater. Sci. Eng., A273-275(1999), 40-57
[58] GR. Speich and WC. Leslie: Metall Trans., 3(1972), 1043-1054
[59] S. Morito, H. Tanaka, R. Konishi, T. Futuhara and T. Maki: Acta Mater., 54(2003), 1789-1799
[60] JA Klosterman: J. less common Met., 28(1972), 75-79
[61] S. Morito, X. Huang, T. Futuhara, T. Maki and N. Hansen: Acta Mater., 54(2006), 5323-5331
[62] G. Kurdjumov and G. Sachs: Zeitschrift fur Physik, 64(1930), 325-343
[63] T. Ohmura, M. Hayakawa, K. Miyahara, S. Matsuoka, K. Tsuzaki and T. Takahashi: Proceedings of 20th Risa International Symposium on Materials Science. Deformation-Induced Microstructures: Analysis and Relation to Properties Roskilde, Denmark, (1999), 443-439
[64] F-G. Wei and T. Tsuzaki: Scripta Mater., 52(2005), 467-472
[65] B. Hutchinson, J. Hagstrom, O. Karlsson, D. Lindell, M. Tornberg, F. Lindberg and M. Thuvander: Acta Mater., 59(2011), 5845-5858
[66] S. Morito: ISIJ Int. 43(2003), 1475-1477
[67] G. Thomas and J. Washburn (Eds): Electron Microscopy and Strength of Crystals, John Wiley & Sons Inc, New York, USA, 1963
[68] LA. Nordstrom: Scand. J. Metall., 5(1976), 159-165
[69] M. Kehoe and PM Kelly: Scripta Metall., 4(1970), 473-476
[70] S. Morito, H. Saito, T. Ogawa, T. Furuhara and T. Maki: ISIJ Int., 45(2005), 91-94
[71] RN. Caron and G. Krauss: Metall. Trans., 3(1972)2381-2389
[72] GR. Speich: Trans. Metal. Soc. AIME., 245(1969)2553-2564
[73] C. Zhu, A. Cerezo and GDW. Smith: Ultramicroscopy., 109(2009), 545-552
[74] Y. Ohmori and I. Tamura: Metall Trans A, 23A(1992), 2737-2751
[75] S Takebayashi, T. Kunieda, N. Yoshinaga, K. Ushioda and S. Ogata., ISIJ Int. 50(2010), 875-882
[76] J.W. Christian, The Theory of transformations in metals and alloys, 1st edition, Pergamon, Oxford, UK, 2002.
[77] J. Strid and KE. Easterling: Acta Metall., 33(1985), 2057-2074

[78] M. Enemoto, JK. Lee and HI. Aaronson, Mechanisms of diffusional phase transformations in metals and alloys, CRC press, Taylor and Francis, London, UK, 2010.
[79] JH. Jang, C-H. Lee, Y-U. Heo and D-W. Suh: Acta. Mater., 60(2012), 208-217
[80] H. Landheer., Nucleation of ferrite in austenite, The role of crystallography, TU Delft, Delft, The Netherlands, 2010
[81] KC. Russell: Acta Metall., 16(1968), 761-769
[82] CEIC. Ohlund, D.den Ouden, J.Weidow, M.Thuvander and SE. Offerman: ISIJ Int,, 55(2015), 883-892
[83] C. Zener: J. Applied Phys., 20(1949), 950-953
[84] M. Perez: Scripta Mater., 52(2005), 709-712
[85] A. Teresiak and H. Kubsch: NanoStructured Mater., 6(1995), 671-674
[86] Z-G. Yang and M. Enemoto: Mater. Sci. Eng. A., 322(2002), 184-192
[87] F-G. Wei, K. Tsuzaki: Metall. Mater. Trans. A., 37A(2006), 331-353
[88] F-G. Wei, T. Hara, T. Tsuchida and K. Tsuzaki: ISIJ Int., 43(2003), 539-547
[89] W-S. Jung, S-C. Lee and S-H. Chung: ISIJ Int., 48(2008), 1280-1284
[90] H-K. Kim, W-S Jung and B-J. Lee: Acta Mater., 57(2009), 3140-3147
[91] A. Sawahata, M Enemoto, K. Okuda and T. Yamashita: Tetsu-to-Hagane., 94(2008), 21-29
[92] DHR. Fors and G Wahnstrom: Phys. Review. B., 82(2010), 1-13
[93] W. Kesternich: Philos Mag A., 52(1985), 533-548
[94] Z. Wang, X. Mao, Z. Yang, X. Sun, Q. Yong, Z. Li and Y. Weng: Mater. Sci. Eng. A., A529(2011), 459-467
[95] Moll SH and Ogilvie RE: Trans. Metal. Soc. AIME., 2015(1959), 613-618
[96] P. Klugkist and CHR Herzig: Phys. Stat. Sol., 148(1995), 413-421
[97] AS. Arrott and B. Heinrich: J. Appl. Phys., 52(1981), 2113-2115

3 The kinetics of softening and microstructure evolution of martensite in Fe-C-Mn steel during tempering at 300°C

C. Emmy I.C. Ohlund, Erik Schlangen and S. Erik Offerman

Materials Science & Engineering A, 560 (2013) 351-357

Abstract

A fundamental understanding of the properties of tempered martensitic steel during the production and service of fasteners helps the development of cost-effective, micro-alloyed, medium-carbon steel for future automotive fasteners, which have to fulfill more stringent requirements due to the on-going trend of down-sizing the car engine. We have studied the relation between the softening kinetics of martensite and the kinetics of the evolution of the microstructure in high-purity Fe-C-Mn steel during tempering at 300˚C by means of nano-indentation, SEM, and EBSD. The as-quenched specimen consist of martensite blocks that are auto-tempered and non-tempered. We find that the nano-hardness that is measured directly at the martensite boundaries is significantly higher than the nano-hardness that is measured in the martensite matrix. The boundary regions soften with increasing tempering time, whereas the nano-hardness of the tempered matrix remains approximately constant with increasing tempering time. The kinetics of martensite softening can be described by three stages that are related to the evolution of the microstructure. However, most of the softening takes place during the first stage of tempering: The macroscopic softening of martensite is mainly related to: (i) the nano-scale softening of boundary regions, (ii) the reduction in area fraction of the boundaries regions, and (iii) the reduction in area fraction of the non-tempered matrix regions.

3.1 Introduction

Tempered martensitic steel is the most commonly used material for high-strength fasteners in mass-produced car engines today. The tensile strength of these fasteners is up to class 12.9, which means a tensile strength of 1200MPa and a recommended maximum temperature during service of 150˚C. The trend for car engines is down-sizing, which means that future generations of fasteners are required to have the capability to (1) carry higher loads and (2) resist creep at higher temperatures as compared to today's fasteners. In addition to enhanced requirements for the mechanical properties during service of the fasteners, there are the requirements for the production of the fasteners: the steel needs to be cold formed and heat treated on an industrial scale. Moreover, from a business perspective the steel for the fastener is required to have low levels of alloying elements.

A fundamental understanding of the kinetics of martensite softening in relation to the kinetics of the evolution of the microstructure during tempering is essential for the development of cost-effective, micro-alloyed, medium-carbon steel for future automotive fasteners. Research on as-quenched martensite has shown that the strength/hardness is related to the morphology, carbon concentration, dislocation density, carbide density and the block size of martensite [1-2]. More recently, Ohmura et al. showed that the macroscopic hardness of martensite is the result of the matrix hardness and the hardness of grain boundaries (the grain boundary/size effect). They have observed this by measuring the ratio of the matrix nano-hardness H_n and the macroscopic hardness H_v [3-7]. A recent study by Hutchinson et al. concluded that segregation of carbon atoms to defects during quenching is the largest single factor controlling the strength of as-quenched martensite. Furthermore, the study of Hutchinson concludes that the amount of carbon existing in solid solution after quenching is very small (0.02 wt.%) and independent of the total carbon content of the steel [8]. From these observations we derive the hypothesis that the nano-hardness at grain boundaries should be significantly higher than in the matrix of as-quenched martensite in medium carbon steels.

The strength of martensitic steel is known to reduce during temperature exposure. The factors causing softening, listed in the order they appear in time and for increasing temperatures are: migration of carbon atoms, decomposition of retained austenite, precipitation and coarsening of cementite, recovery of dislocation structure and recrystallization [9-12]. More recently, Ohmura et al. characterized the temper-softening behavior of Fe–C martensitic steels by nano-indentation. They found that both the matrix hardness and the grain size/boundary effect decrease with increasing tempering temperatures [13-17]. However, no studies have been performed on the time-dependency of the softening kinetics of martensite during isothermal tempering by using nano-indentation. Moreover, no studies have been conducted to measure if there is a difference in the softening kinetics of the grain boundaries and of the matrix of martensite by using nano-indentation.

The aim of this study is to determine the relation between the softening kinetics and the microstructure evolution during isothermal tempering of Fe-C-Mn martensite. We specially focus on the hardness of grain boundaries, since previous research has shown that the strength of as-quenched medium-carbon, martensitic steel strongly depends on these boundary regions.

For the purpose of evaluating the softening of the grain boundaries we have developed and validated a methodology to differentiate between nano-hardness measurements performed directly at grain boundaries and measurements performed in the matrix by using the technique of continuous stiffness measurement (CSM) nano-indentation [18]. Moreover, we have studied the kinetics of other microstructural factors potentially leading to martensite softening during tempering: strain relief, carbide precipitation and coarsening, and martensite block coarsening.

3.2 Experimental procedures

The material investigated is a ternary, high-purity Fe-C-Mn alloy. The composition is given in table 3.1. The steel is received with a carbon concentration of 0.011 wt.%, machined into cylinders with a diameter of 4 mm and subsequently carburized to 0.39 wt.%C.

Table 3.1 *Steel composition (wt.%)*

C	*Mn*	*Si*	*P*	*S*	*Al*	*Cu*	*Cr*	*O*	*V*
0,39	*0,87*	*0,0035*	*0,0010*	*0,0007*	*0,0050*	*0,0021*	*0,0018*	*0,0008*	*0,0023*

The steel cylinders are cut into 10 mm long specimens for heat-treatment in a Bähr 805 A/D dilatometer (Bär-Thermoanayse GmbH, Hüllhorst Germany). A homogenization treatment is performed at 1100˚C for 207 minutes followed by cooling to 500˚C. Thereafter, the steel is austenitized at 940˚C for 40 minutes, followed by quenching to room temperature with He at a rate of 45 ˚C/s between the martensite start (M_s) and finish (M_f) temperatures. Tempering treatments are performed at 300˚C for 5, 10, 30, 60 and 600 minutes. All heating rates are 2 ˚C/s. After heat treatment all samples are prepared by grinding and polishing down to 1 µm. After full homogenization the carbon concentration was verified by line scans with Electron probe micro-analysis.

Scanning electron microscopy (SEM, JEOL JSM-6500F with field emission gun) is performed on nital etched surfaces to determine the kinetics of the evolution of the microstructure during tempering: the area fraction of tempered regions, the carbide dimensions, and carbide number density.

Conventional micro-vickers hardness measurements and CSM nano-hardness measurements are performed in order to study the softening kinetics during tempering. Micro-Vickers hardness is measured at twenty locations on polished specimens using a load of 500g and reflects the macroscopic hardness of the investigated steel. CSM nano-indentation measurements are performed on electro-polished specimens. Electropolishing is conducted in a solution of 8 % perchloric, 10 % butylcellosolve, 60 % ethanol and 22 % water at 0°C under a potential of 55V. An Agilent G200 nano-indenter equipped with a Berkovich-indenter and a oscillation amplitude of 2nm is employed. The tip is calibrated using a reference specimen of fused silica. The hardness values are determined following the method of Oliver and Pharr [19]. We performed 8 x 8 indents to a depth of 60 nm on each steel specimen. An additional array of 5 x 5 indents to a depth of 400 nm is made on the as-quenched sample to verify that the macroscopic hardness and E-modulus of the steel are reached. We determined the location (at a boundary or in the matrix of the martensite) of the nano-indents on the as-quenched specimens by using EBSD. A step-size of 150-175 nm is used for identification of the position of the nano-indents. The accuracy of the nano-hardness measurements is 14 % for the CSM nano-indenter that we used, which we determine by measuring the hardness of 8 nano-indents on a single ferrite grain in the steel with the as-received composition of 0.011 wt% C. A single ferrite grain is studies instead of a single martensite grain, because a single ferrite grain is possible to make larger and is microstructurally more homogenous than (tempered) martensite.

Electron-back scatter diffraction (EBSD with a Nordlys detector) measurements are performed on electropolished surfaces to determine the kinetics of the evolution of the microstructure during tempering: the martensite grain size and the width of the boundary region. The EBSD-data are acquired and post-processed with the Channel 5 software. A step size of 100nm is used during the EBSD-mapping. The diameter of the electron-beam is 16nm during the EBSD-measurements, which gives a spot size of 16x35nm due to the tilt of the sample.

3.3 Results and discussion

3.3.1 SEM studies

Fig. 3.1 shows SEM images of the specimens annealed for different times at 300˚C. Fig. 3.1(a) shows that the as-quenched microstructure is comprised of two types of regions: (1) rough, carbide-containing regions and (2) smooth, carbide-free regions.

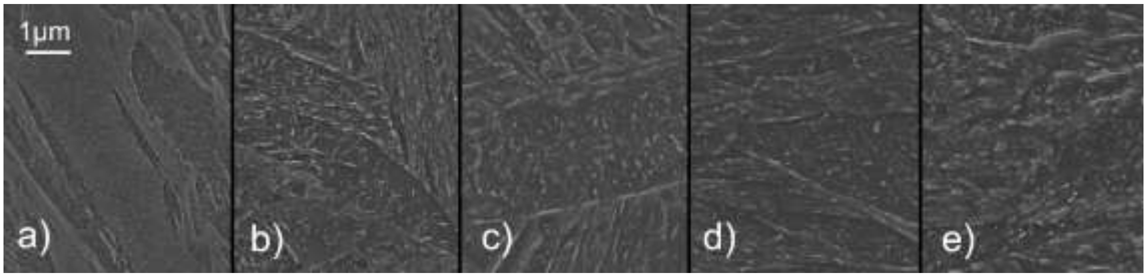

Figure 3.1 *SEM images of the microstructure of the heat treated specimens: (a) as quenched and the specimen tempered at 300˚C for (b) 5 minutes, (c) 10 minutes, (d) 30 minutes and (e) 60 minutes.*

The two different regions correspond to auto-tempered regions (containing carbides) and non-tempered regions (smooth). Auto-tempering means that tempering started during the quenching process, i.e. carbon diffusion resulting in segregation and modulation of carbon atoms and carbide precipitation. The observed difference in etching depth between auto-tempered and non-tempered regions is most likely due to the different concentration of carbon atoms in solid solution in the two different regions and not due to differences in crystal orientations between grains. In case the crystal orientations were the main reason for different etching depths, similar effects would be present also in the tempered specimens, which is not the case. The presence of both tempered and non-tempered regions in the as-quenched state is believed to be a direct result of the martensite formation kinetics during quenching. During martensite transformation [20] the full volume of the steel is not transformed into martensite instantaneous. The volume fraction of transformed martensite is a function of time during the quenching process. As a result, the interstitial carbon atoms inside the first formed martensite crystals will have more time to diffuse at elevated temperature, as compared to the interstitial carbon atoms in the last volume fraction of transformed martensite.

Fig. 3.1(b)-(e) shows the microstructure of tempered specimens, which consists of only rough, tempered, carbide-filled regions.

3.3.2 Nano-indentation studies

Fig. 3.2 shows the average nano-hardness <H_n> and the average E-modulus as measured by CSM nano-indentation at the boundaries, tempered matrix, and non-tempered matrix of martensite of the as-quenched specimen as a function of the indent depth. Examples of nano-indents located in the matrix of martensite and at boundaries as measured on the as-quenched sample by EBSD are shown in Fig. 3.2(b) and (d) respectively.

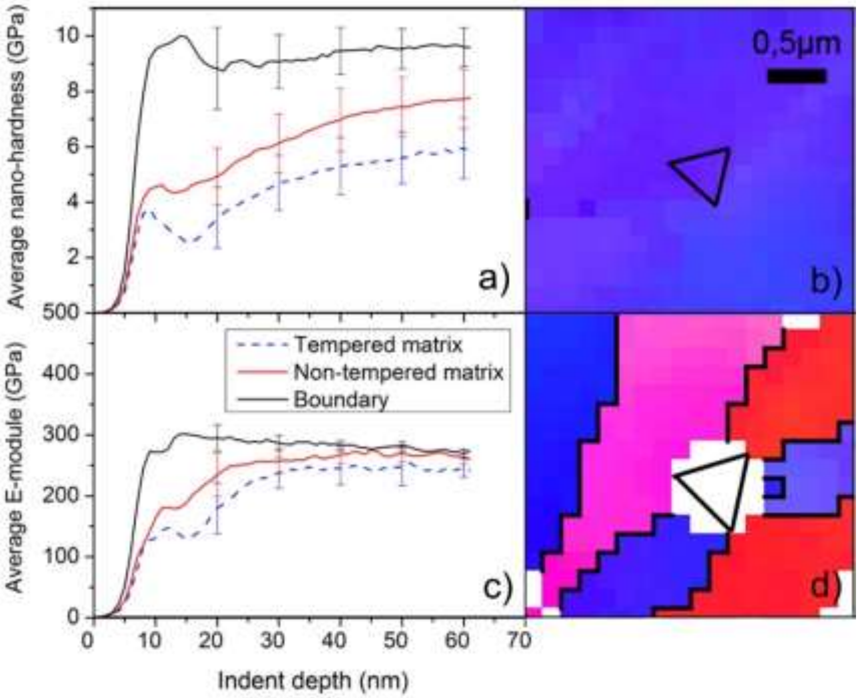

Figure 3.2 *The average (a) nano-hardness<H_n> and (c) E-modulus measured in the matrix and at the grain boundaries as a function of indent depth. Examples of EBSD scans of a nano-indent located (b) in the matrix and (d) on a boundary. The nano-indents are located within the triangle and boundaries exceeding 10˚ misorientation are marked with black lines. The error bars represent the 95% confidence interval and is chosen at 5 different indent depth to indicate the spread of the measurements over the full indent depth.*

Thirteen indents are found on martensite boundaries, which separate areas of different crystal orientations with misorientations that are exceeding 10˚, see e.g. the IPF map in Fig. 3.2(d). Seventeen indents are found to be located inside the matrix as they are placed in regions of similar crystal orientations according to the IPF map, see e.g. Fig 3.2(b). The matrix indents of the as-quenched sample can thereafter be further divided into non-tempered matrix regions and tempered matrix regions by looking for the presence of carbides in the SEM images, see Fig 3.1. Seven matrix indents are found in tempered regions according to SEM.

Fig. 3.2(a) shows that the that the nano-hardness of the martensite boundaries is significantly higher than the nano-hardness of the non-tempered matrix, which is in turn significantly higher than the nano-hardness of the tempered matrix. This observation confirms our hypothesis and is in line with the observations of Hutchinson et al. [8]. We further observe that the nano-hardness of matrix indents continues to increase from indent depths of 20 nm to indent depths of 60 nm whereas the nano-hardness of boundaries has reached final hardness already at indent depths of 20-30 nm. We make use of this difference in the shape of the curves for the nano-hardness as a function of indent depth to distinguish between measurements of nano-indents at boundaries and in the matrix for the annealed specimens, see Fig 3.2(a).

Fig. 3.2(c) shows that the E-modulus as a function of indent depth reaches a stable value at a depth of approximately 60 nm. According to the hemispherical approximation, the plastically deformed zone of an indent to a depth of 60 nm is approx. 560 nm [7] which fits inside the average size of the martensite block which is measured to be 3.5 μm^2, see below. For these two reasons, the reported nano-hardness values in the remainder of this paper are measured at a depth of 60 nm, which is also in correspondence to earlier literature [4, 13-16]. Moreover, the validation measurements on the as-quenched specimen to a depth of 400 nm show that at depths exceeding 150 nm the curves of the nano-hardness and of the E-modulus have converged to the same values: the macroscopic properties of the steel. At all indent depths lower than 150 nm the matrix hardness is lower than the macroscopic hardness.

3.3.3 EBSD studies

Fig. 3.3 show EBSD-measurements of the microstructures of the as-quenched sample (a)-(c) and the sample tempered for 60 min. EBSD measurements of the microstructures of the intermediate tempering times were also measured, but are not shown. During EBSD mapping of the as-quenched specimen, no points were indexed as austenite.

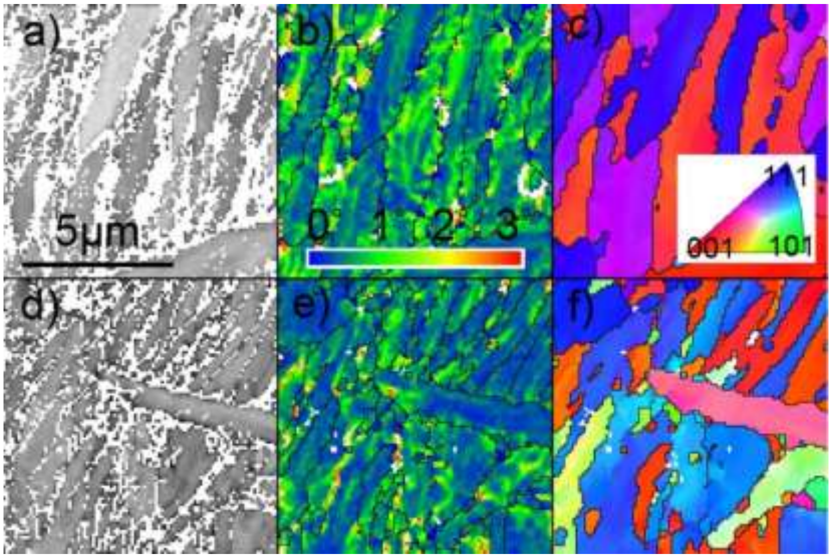

Figure 3.3 *EBSD-images of the microstructure of the as-quenched specimen (a-c) and the specimen tempered for 60 minutes (d-f).The Left column (a and d) shows the band contrast prior to noise reduction where non-indexed pixels show as light blue, the middle column (b and e) shows the misorientation mapping after noise reduction in which boundaries exceeding 10˚ are represented as black lines, and the right column (c and f) shows the inverse pole figure (IPF) maps in which boundaries of less than 10˚ misorientation are represented as thin white lines.*

The EBSD-images in Fig. 3.3(a) and (d) show the band contrast of the as-quenched specimen and the specimen tempered for 60 minutes as measured prior to noise reduction, respectively. The band contrast is a measure of the quality of the Kikuchi pattern and is shown on a black-white scale, where poor band-contrast is shown as dark areas. Reduction of pattern quality is typically a result of surface roughness, grain boundaries and dislocations which induce strain in the measured lattice [21]. Fig. 3.3(a) and (d) shows that the band contrast is degraded close to non-indexed regions. Non-indexed points, which are shown as white pixels, arise during EBSD mapping when the Kikuchi patterns cannot be identified at all.

Fig. 3.3(b) and (e) shows the misorientation-profiles of the same EBSD-images as shown in Fig. 3.3(a) and (d), but after noise reduction. The grain boundaries are defined as boundaries between two neighboring pixels with a misorientation that exceeds 10˚ (shown as black lines). We observe that all grain boundaries exceeding 10˚ are located inside formerly non-indexed regions. These grains structures are interpreted as block boundaries in accordance to earlier literature [6-7, 14-15]. The misorientation profiles are calculated from the average misorientation within sections of 3x3 pixels, all belonging to the same grain, i.e. with a smaller misorientation than 10˚ between the pixels. Fig. 3.3(b) and (e) shows that the misorientation increase towards the martensite boundaries.

Fig. 3.3(c) and (f) shows the inverse pole figures (IPF). Block boundaries are again marked with black lines. The average block size is measured to be 3.5 µm^2 for all tempered specimens. No block coarsening take place during the 60 min of annealing. A slightly higher block size is measured for the as-quenched state. This is an artifact of the post processing of the EBSD data as non-indexed regions become integrated in larger neighboring grains.

The non-indexed points in Fig. 3.3(a) and (d) are observed at and around block boundaries. Comparison of Fig. 3.3(a) and (d) further shows that the area fraction of non-indexed regions decreases with increasing annealing time. The width of the non-indexed regions is measured via the line intercept method in the horizontal and vertical direction of each scan. The line intercept analysis showed the same average width, independent of measurement direction, demonstrating that the asymmetric geometry of the beam spot has no influence on the results. The average width of the non-indexed regions is 350nm and 200 nm for the as-quenched sample and the sample tempered for 60 min, respectively. A recent study performed with high-resolution EBSD on an extensively tempered low carbon steel has shown that the width of the region within which the lattice orientation is distorted over a grain boundary has a thickness of 40 nm [22]. These results indicate that the minimum block boundary thickness we can expect to measure by EBSD exceeds 40 nm.

The above results (band contrast and misorientation mapping) show that the strain levels in the martensite increases closer to non-indexed regions. The results further show that the non-indexed regions contain the block boundaries of the martensite and that no block coarsening take place during tempering at 300 ˚C. As the surface roughness should be comparable for all test specimens (the electropolishing was carried out using the same parameters), the non-indexed regions are considered to be a result of high strain due to high dislocation density. The relative change of non-indexed points for different tempering times is considered to be a direct result of dislocation annihilation within the non-indexed regions. In this study, we define the width of the non-indexed regions as the boundary region. A quantitative analysis of the images in Fig. 3.3 is given in the next section.

3.3.4 Softening and microstructure evolution

Fig. 3.4(a) shows the macroscopic hardness H_v measured as a function of tempering time. The hardness reduces from 543.8 HV for the as-quenched specimen to 422.7 HV after 60 min of tempering. The hardness loss is highest during the first 5 min of tempering, but continues after 10 min of tempering. Extended tempering from 60 to 600 min resulted in only a minor hardness drop of 5 HV and therefore the 60 min tempering state is considered the full tempering level in the present investigation. Fig. 3.4(a) also shows the ratio of the nano-hardness, H_n, to the macroscopic hardness H_v. In agreement with Ohmura et al. [13-17] we observe that the H_n/H_v-ratio increases with tempering time. For the curve with the filled box-shaped symbols we used the nano-hardness of the tempered matrix (see Fig. 3.4(b)) for H_n. The present study shows that the increase of the H_n/H_v-ratio becomes less with increasing tempering time. The open-box-shaped symbol in Fig. 3.4(a) represents the H_n/H_v-ratio based on the average nano-hardness of matrix, as calculated from the relation of area fractions of tempered and non-tempered matrix in the as quenched state (black and red line in Fig 3.4(c)).

Fig. 3.4(b) shows the nano-hardness of the tempered matrix, non-tempered matrix, and of boundaries, measured at 60 nm depth, as a function of tempering time. We observe that the nano-hardness of boundaries is significantly higher than the nano-hardness of the matrix (both tempered and non-tempered matrix), at each investigated tempering time. We further observe that the nano-hardness of the non-tempered matrix is significantly higher than the nano-hardness of the tempered matrix in the as-quenched sample.

Only one data point, at 0 min, exists for non-tempered matrix because these regions disappear within 5minutes of tempering (see Fig 3.4(c)). The nano-hardness of boundaries reduces significantly during the first 5 min of tempering and thereafter reduces only slightly during tempering from 5 to 60 min. The nano-hardness of tempered matrix does not change upon tempering.

Fig. 3.4(c) shows the area fraction of tempered and non-tempered martensite as measured by SEM and the area fraction of boundary regions as measured by EBSD, as a function of tempering time. The area fraction of non-tempered martensite is reduced to 0 within 5minutes of tempering. The area fraction of boundary regions reduces from 0.44 in the as-quenched state to 0.27 after 60 min of tempering due to dislocation annihilation. The block boundaries are assumed to be located in the center of the boundary regions as measured by EBSD.

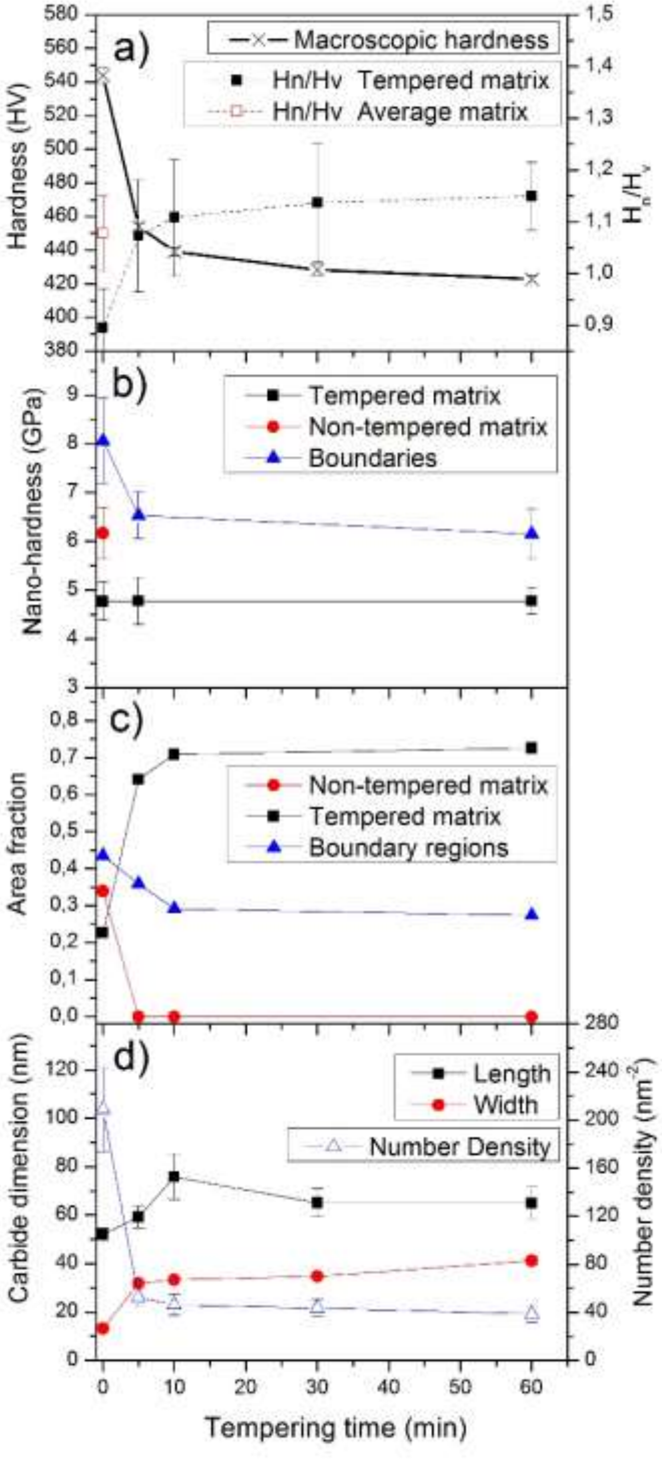

Figure 3.4 *Macro- and nano-hardness and microstructural parameters as a function of annealing time: (a) Macroscopic hardness,* H_v*, [HV0,5] and the ratio of the matrix nano-hardness and the macroscopic hardness (*H_n/H_v*), (b) Nano-hardness,* H_n*, [GPa], (c) Area fraction of tempered, non-tempered and boundary regions and (d) carbide length[nm], width[nm] and number density [*μm^{-2}*]*

Fig. 3.4(d) shows the carbide dimensions and number density as measured by SEM as a function of tempering time. The carbide dimensions initially increase via a combined length and width increase. After 10 min of tempering, spheroidization starts, the carbide length decreases while the width increases. The initial number density of the small carbides observed in the tempered regions of the as-quenched sample exceeds 200 μm^{-2}. This number density is reduced to approx. 50 μm^{-2} after 5 min of tempering. After 60 min of tempering the number density of carbides is reduced to approx. 39 μm^{-2}.

The low macroscopic hardness of the as-quenched specimen is most likely a result of auto-tempering during quenching. An artificial hardness value for comparison with virgin martensite of 0.39 wt.%C can be calculated from the nano-hardness of non-tempered matrix regions combined with the nano-hardness of boundary regions. The area fraction of boundary regions in the as-quenched specimen is shown in Fig. 3.4(c) and the remaining area is for the calculation assumed to consist only of non-tempered matrix. An average hardness value calculated following these principles result in 6.99 GPa, which correlates to 713 HV. This value is in line with literature reports of hardness of 0.39 wt.%C virgin martensite where quenching has been performed in liquid nitrogen to avoid auto-tempering and formation of retained austenite [2].

The higher nano-hardness measured at boundaries, for all tempering times, can be related to carbon atoms being present at defects, as we derive from the research of Hutchinson [8] and the high dislocation density observed in the boundary regions, see Fig. 3.3 and Fig. 3.4(c). Fig. 3.4(c) show that dislocation annihilation in boundary regions continues throughout the majority of the tempering process. Retained austenite in block and lath boundaries can also contribute to added hardness of boundary regions in the as-quenched sample. Retained austenite would cause deformation-induced transformation to high carbon martensite during indentation. Based on the lack of points indexed as austenite during EBSD measurements of the as-quenched sample, in combination with literature reports of very low expected volume fractions of retained austenite in 0.39 wt.%C steels [2] we neglect the possible contribution of retained austenite to the hardness.

The higher nano-hardness of non-tempered matrix is related to the redistribution of carbon atoms in solid-solution in the non-tempered matrix to carbon in carbides in the tempered regions during quenching.

The lack of nano-scale softening of the tempered matrix during tempering can be related to the lower amount of dislocation annihilation inside the matrix. Furthermore we calculate that the possible hardness change due to changes in carbide size and number density in the tempered matrix is in the range of 0.2 GPa according to the Orwan-Ashby model [23], based on the carbide length. This is within the error of the measurement method and is therefore difficult to distinguish.

Fig. 3.5(a) shows the macroscopic softening rate during tempering. During the first 5 minutes of tempering the softening rate is highest (18.0 HV/min), followed by a large reduction in softening rate to 3.0 HV/min between 5 and 10 min. After 10 min, the softening rate continues to reduce to 0.54 HV/min and after 30 min minor softening occurs at a rate of 0.19 HV/min.

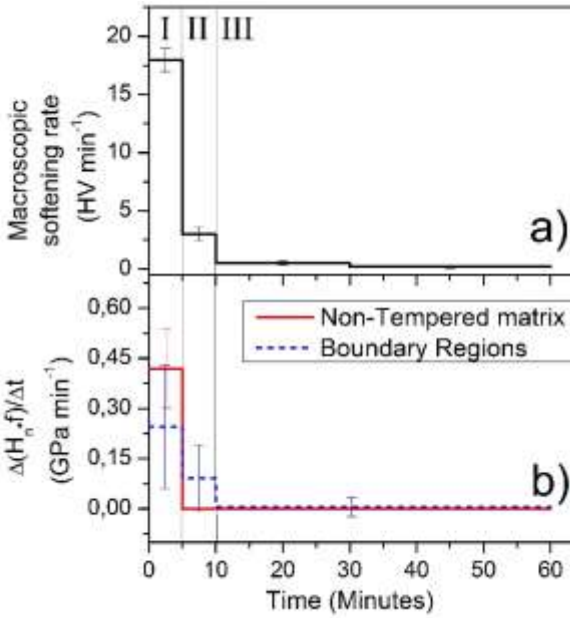

Figure 3.5 *Kinetics of the softening processes during annealing at 300˚C, showing (a) The rate of macroscopic softening [HV min^{-1}]and (b) The rate of nano-scale softening of the tempered matrix regions and the boundary region; nano-hardness H_n, multiplied by the area fraction, f, per unit time [GPa min^{-1}]*

Fig. 3.5(b) shows the change in nano-scale hardness H_n multiplied by the area fraction f per unit time, i.e. $\Delta(H_n \cdot f)/\Delta t$, which is proportional to the relative contributions of the two microstructural regions to the macro-scale softening rate: boundary regions (BR) and non-tempered matrix (NTM). The nano-hardness value of the boundary regions at 10 min of tempering is estimated by interpolating the values measured at 5 and 60 min tempering. From Fig. 3.5 we can distinguish the following three stages in the kinetics of martensite softening in the Fe-C-Mn alloy during tempering at 300 ˚C. The distinction between the tempering stages, is based on the hardness measurements of a limited number of measurement points (5 minutes, 10 minutes, 30 minutes and 60 minutes).The three stages identified are:

I. Stage I (0-5 min) is characterized by fast macroscopic softening kinetics (18,0HV/min) that are strongly related to: (a) fast and simultaneous softening and reduction in area fraction of boundaries regions, i.e. $\Delta H_{nBR} \cdot f_{BR}/\Delta t = 0.24$ GPa/min, and (b) fast reduction in area fraction of non-tempered matrix regions

$\Delta H_{n\mathrm{NTM}} \cdot f_{\mathrm{NTM}}/\Delta t = 0.42$ GPa/min. The microstructure processes of stage I are redistribution of carbon atoms, recovery, and growth of iron carbides from Ɛ-carbides to cementite. Figure 3.1 (a)-(b) and Fig 3.4 (c)-(d) show that these processes take place in parallel and at different rates. Carbon redistribution is most rapid, followed by carbide growth. Recovery appears to be the slowest process.

II. Stage II (5-10 min) is characterized by slow macroscopic softening kinetics (3.0 HV/min) that is related to slow softening and reduction in area fraction of the boundaries regions ($\Delta H_{n\mathrm{BR}} \Delta f_{\mathrm{BR}} = 0.091$ GPa/min). The microstructure processes that dominate stage II are recovery and cementite growth. Figure 3.4(c)-(d) shows that these processes take place in parallel and at different rates. The recovery process is more rapid than the cementite growth process. The recovery process appears to stop during stage II.

III. Stage III (10-60 min) is characterized by very slow softening kinetics (0.54-0.19 HV/min) that is related to very slow softening and reduction in area fraction of boundary regions $\Delta H_{n\mathrm{BR}} \cdot f_{\mathrm{BR}}/\Delta t = 0.0041$ GPa/min). The microstructure process of stage III is cementite coarsening (see Fig 3.4 (d)).

3.4 Conclusions

We conclude the following from our investigation on the softening kinetics and the kinetics of the evolution of the microstructure of martensite in high-purity Fe-C-Mn steel during tempering at 300˚C:

1) The nano-hardness measured directly at the martensite boundaries is significantly higher than the nano-hardness measured in the matrix for the as-quenched specimen.
2) The boundary regions soften with increasing tempering time, whereas the nano-hardness of the tempered matrix remains approximately constant with increasing tempering time.
3) The kinetics of martensite softening can be described by three stages, which are related to the evolution of the microstructure. However, most of the softening takes place during the first stage of tempering. The macroscopic softening of martensite is mainly related to: i) the nano-scale softening of boundary regions, ii) the reduction in area fraction of the boundaries regions, and iii) the reduction in area fraction of the non-tempered matrix regions.

3.5 References

[1] GB. Olson and W.S. Owen (Eds.): Martensite, ASM International, Materials Park, Ohio, USA, 1992
[2] G. Krauss: Mater. Sci. Eng., A 273 (1999) 40-57
[3] T. Ohmura, M Hayakawa, K. Miyahara, S. Matsuoka, K. Tsuzaki and T. Takahashi: (1999) 20th RISO International Symposium on Materials Science (p. 433) Roskilde, Denmark
[4] T. Ohmura, K. Tsuzaki and S. Matsuoka: Scripta Mater., 45 (2001) 889-894
[5] J. Li, T. Ohmura, F. Wei and K. Tsuzaki: Mater. Sci. Forum., 475-479 (2005) 4109-4112
[6] J. Li, T. Ohmura and K. Tsuzaki: Materials Transaction., 46 (2005) 1301-1305
[7] J. Li, T. Ohmura and K. Tsuzaki: Sci. China. Ser E: Technol. Sci., 49 (2006) 10-19
[8] B. Hutchinson, J. Hagstrom, O. Karlsson, D. Lindell, M. Tornberg, F. Lindberg and M. Thuvander: Acta Mater., 59 (2011) 5845-5858
[9] KA. Taylor and M. Cohen: Progr. Mater. Sci., 36 (1992) 225-272
[10] GT. Eldis and M. Cohen: Metall. Mater. Trans., A 14A (1983) 1007-1012
[11] GR. Speich and WC. Leslie: Metall. Mater. Trans., B 3(1972) 1043-1054
[12] RN. Caron and G. Krauss: Metall. Mater. Trans., B 3 (1972) 2381-2389
[13] T. Ohmura, K. Tsuzaki and S. Matsuoka: Phil. Mag. A., 82 (2002) 1903-1910
[14] T. Ohmura, T. Hara and K. Tsuzaki: Scripta Mater., 49 (2003) 1157-1162
[15] T. Ohmura, T. Hara and K. Tsuzaki: J. Mater. Res., 18 (2003) 1465-1470
[16] T. Ohmura and K. Tsuzaki: J. Phys. IV France., (2003) 267-270
[17] T. Ohmura and K. Tsuzaki: Mater. Sci. Forum., 475-479 (2005) 4113-4116
[18] X. Li, B. Bhushan: Mater. Charact., 48 (2002) 11-36
[19] WC. Oliver and GM. Pharr: J. Mater. Res., 7 (1992) 1564-1583
[20] SMC van Bohemen, J. Sietsma, MJM Hermans and IM Richardson: Acta Mater. 51 (2003) 4183-4196
[21] SI. Wright, MM Nowell and DP. Field: Microsc. Microanal., 17 (2011) 316-329
[22] CJ. Gardner, BL. Adams, J. Basinger and DT. Fullwood: Int. J. Plasticity., 26 (2010) 1234-1247
[23] T. Gladman, Precipitation hardening in metals, The Institute of Materials, The University Press, London, UK,1997

4 Effect of Ti on evolution of microstructure and hardness of martensitic Fe-C-Mn steel during tempering

C.Emmy I.C. Ohlund, Jonathan Weidow, Mattias Thuvander
and S.Erik Offerman

ISIJ International, Vol 54 (2014), No. 12, pp. 2090-2899

Abstract

The effect of the addition of 0.042 wt.% of titanium on the relation between the evolution of the microstructure and the softening kinetics of quenched martensite in high-purity Fe–C–Mn steel has been studied during tempering at 300 and 550°C. The evolution of the microstructure is characterized by measuring the cementite particle size, the martensite block size, the area fraction of martensite regions which contain a high dislocation density, the macroscopic hardness , the nano-hardness of martensite blocks boundaries, the nano-hardness of the matrix and the TiC-precipitate size during tempering. Nucleation of TiC-precipitates take place during annealing at 550°C and starts earlier in regions close to the block boundaries, after 5-10 minutes, and thereafter in the matrix, after 10-30 minutes, due to the higher dislocation density in the regions close to the block boundaries. The TiC-precipitates slow down the recovery in regions of high dislocation density compared to the alloy without TiC-precipitates. The TiC-precipitates increase the macroscopic hardness of the steel after 30 minutes annealing at 550°C. The growth of TiC-precipitates in martensite is simulated in good agreement with experimental observations by a model that takes into account: 1) capillarity effects, 2) the overlap of the titanium diffusion fields between TiC-precipitates, and 3) the effect of pipe diffusion of titanium atoms via multiple dislocations. The average, experimentally-observed, TiC-precipitate size is 69±48 Ti atoms.

4.1 Introduction

Tempered martensitic steel of strengths up to 1200 MPa is the most commonly used material for high-strength fasteners in mass-produced car engines today. The recommended maximum temperature during service is 150˚C [1]. These are the typical requirements for the service conditions of fasteners for mass-produced passenger cars. However, the current trend of engine down-sizing has resulted in higher mechanical and thermal loading of the engines. There is a need for stronger (and yet tough) steels at higher temperatures for engine fasteners. The design of this steel must fulfil additional requirements. The alloying elements should be abundantly available and should be added in low quantities to assure cost and material formability. Furthermore, heat-treatment must be possible using industrial heat-treatment equipment and tempering temperatures above 425 °C according to the ISO898-1 standard [1].

Precipitates have for decades been used in steels in order to improve mechanical properties of steel. Good examples are the improved fire-resistance of construction steel [2], the temperature and wear resistance of tool and high-speed steels [3], and the creep-resistance of 9-12Cr martensitic steels for the power generation industry [4-6]. These improvements of properties are based on a fine dispersion of precipitates, which act like pinning points for dislocations and hinder dislocation movement and recovery. Recent research suggests that TiC-precipitates are good candidates for improving the strength of martensite at elevated temperature due to their slow coarsening rate [7]. Martensitic steel with medium carbon content and a small addition of Ti (around 0.04 wt%) is therefore an interesting candidate steel for making steels for fasteners that are stronger at higher temperatures. Furthermore are TiC-precipitates known to act as hydrogen traps [8-10] and improve the resistance to hydrogen-induced damage, a very desirable feature when creating a high-strength steel for the automotive industry.

In order to optimize the microstructure and properties of the steel we need fundamental understanding of the relation between the evolution of the microstructure and the softening kinetics during tempering of martensite with small additions of titanium. Previous research has shown that the strength of as-quenched and tempered, medium-carbon, martensitic steel strongly depends on the grain boundaries [11-14]. The grain boundaries of the martensite blocks bring a so called grain boundary effect to the steel; the boundaries are harder than the grain interior and therefore increase the macroscopic strength.

We know that TiC-precipitates nucleate near dislocations and that the nucleation rate is increased by increasing dislocation density [15-21]. However, the interplay is not clear between the nucleation and early growth of TiC-precipitates and the softening of the martensite due to the redistribution of carbon and titanium atoms into cementite and TiC and the dislocation annihilation during tempering.

The aim of this study is to determine the effect of titanium in solid solution and TiC on the evolution of the microstructure and the softening kinetics of quenched martensite in Fe–C–Mn steel during tempering at 300 and 550 °C. A special focus of our research is to differentiate between the hardness of block boundaries and the matrix, because previous research has shown that the strength of medium-carbon, martensitic steel strongly depends on martensite block boundaries [11-14].

4.2 Method

One Ti-containing and one Ti-free alloy of Fe-C-Mn is investigated. The steel compositions are given in table 1. Both steels are received with a carbon concentration of 0.011 wt%, machined into cylinders with a diameter of 4 mm and subsequently carburized to a carbon concentration of 0.39 wt.%C. The steel cylinders are cut into 10 mm long specimens for heat-treatment in a Bähr 805 A/D dilatometer (Bär-Thermoanayse GmbH, Hüllhorst Germany). Both steels are given a homogenization treatment before quenching to martensite The Ti-free steel is homogenized at 1100 ˚C for 207 min, followed by natural cooling to 500°C to form ferrite. The steel is thereafter transformed to austenite again, at 940˚C for 40 min, to create smaller austenite grain sizes. The Ti-containing steel is homogenized at 1350˚C for 30 min to assure that all Ti-atoms are in solid solution.

Both steels are quenched to room temperature from their respective homogenization/austenization temperatures, using He-gas, at a cooling rate of approx. 175-180 °C/s from the start of quench to the martensite start (M_s) temperature and a cooling rate of approx. 45 ˚C/s between the M_s and finish (M_f) temperatures. The M_s temperature is approx. 360-370 °C and 380-390 °C for the Ti-free and the Ti-containing steel respectively. Tempering treatments are subsequently performed at 300 ˚C and 550°C for 5, 10, 30 and 60 min. The heating up time to the tempering temperature is 138 s. The tempering temperature of 300 °C is chosen to assure that all Ti atoms remain in solid solution and the tempering level of 550 °C is chosen to assure that TiC nucleation and growth takes place during tempering [8-9].

All specimens are prepared by grinding and polishing to 1 µm diamond dispersion, followed by 5 % nital etching or electro-polishing conducted in a solution of 8 % perchloric, 10 % butylcellosolve, 60 % ethanol and 22 % water. Electron probe micros-analysis (EPMA) is performed to verify that the specimens are indeed homogeneous in composition after the homogenization treatment, as determined with a spatial resolution of 1 µm. The cementite particle size is measured by scanning electron microscopy (SEM, JEOL JSM-6500F with field emission gun) on nital etched surfaces. The size of the martensite blocks and the boundaries between the martensite blocks is measured by electron back-scatter diffraction (EBSD with a Nordlys detector), on electro-polished surfaces. The EBSD data are acquired and post-processed with Channel 5 software. The beam diameter during EBSD mapping is approx. 16 nm, resulting in a spot dimension of 16 x 35 nm. This spot dimension is combined with a step size of 100 nm.

Transmission electron microscopy (TEM) is used to control that no TiC-precipitates are present in the steel after quenching and Atom probe tomography (APT) is used to measure the TiC precipitate size after annealing of the martensite. The TEM specimens are produced with the in-situ lift-out method [22] using a FEI Strata DB235 DualBeam workstation combining a focused ion beam with a scanning electron microscope (FIB-SEM). The TEM specimens are analysed in a FEI Tecnai G2 transmission electron microscope working at 200 kV with a LaB_6 filament. APT specimens are produced with an in-situ lift-out method [23] using the FEI Strata 235 DualBeal workstation. The specimen is sharpened by Ga+ sputtering using a pattern shaped as an annulus circle. The voltage used is 30 kV with an initial current of 3000 pA which is decreased as the specimen becomes sharper. The final sputtering is performed at 10 kV and 300 pA in order to decrease the gallium implementation in the specimen.

The APT specimens are analysed in an Imago LEAP 3000X HR atom probe tomography instrument. The analyses are performed using laser pulsing at 200 kHz and the laser energy of 0.2 nJ. The specimen temperature is 30-50 K and the evaporation rate is 1 %. The reconstruction and data evaluation is performed using IVAS 3.6.1 software. The quantitative analysis is based on isotope distributions of different ions of relevant atom types [24]. Overlaps involving Ti atoms exist at 24 Da (given by $^{48}Ti^{2+}$ or one molecular ion consisting of two $^{12}C^{+}$) and 16 Da (given by $^{48}Ti^{3+}$ or O^{+}). We correct the number of Ti counts at 24 Da with the Ti counts in the surrounding peaks, 23, 23.5, 24.5 and 25 Da. The surrounding peaks have no overlap with other atom types and the Ti count at 24 Da is scaled according to the natural isotope abundance. For the Ti atoms in the TiC precipitates the oxygen ion count at 16 Da is compared with the known nominal concentration of oxygen in the steel and the excess count is attributed to Ti.

The quantitative APT analysis of C atoms is based on ions detected at 6, 6.5, 12 and 13 Da, plus all ions which exceeded the expected Ti level at 24 Da (as two C ions).

The detection and visualization of TiC-precipitates is done via isoconcentration-surfaces enclosing regions which contain a Ti concentration that exceeds the nominal steel concentration by 20 times (high enough to avoid local fluctuations or segregations of Ti atoms and low enough to avoid ruling out very small TiC precipitates). The diameter of the precipitates is determined from the number of Ti atoms measured by APT, together with the lattice parameter of TiC. We count 4 Ti atoms per unit cell of TiC.

Micro-Vickers hardness is measured at 20 locations on polished specimens using a load of 500 g. CSM nano-indentation measurements are performed on electro-polished specimens using an Agilent G200 nano-indenter equipped with a Berkowich-indenter and oscillation amplitude of 2 nm. The tip is calibrated using a reference specimen of fused silica and the hardness values are determined following the method of Oliver and Pharr [25]. We perform 8 x 8 indents to a depth of 70 nm on each sample. The location of each individual indent is derived via the methodology developed by Öhlund et al [11]. The method is based on the fact that the shape of the nano-hardness and the E-module curves, as a function of indent depth, has a steeper increase during the first 20-25 nm for indents located at block boundaries, whereas indents located in the matrix show a gradual increase of the values. The method was validated previously by us by determining the location of the indents by EBSD measurements [11] where 13 indents on block boundaries and 17 indents in the matrix were compared. Block boundaries were defined as boundaries with a misorientation that exceeded 10° and IPF mapping revealed that the majority of all block boundaries in the investigated specimen had a misorientation in the range of 45-60°.

4.3 Results

4.3.1 Cementite particle size evolution

Fig. 4.1 shows SEM images of Ti-free martensite (a)-(b) and Ti-containing martensite (c)-(d) in the as-quenched condition and after tempering for 60 min at 550 °C. The intermediate tempering times at both 300 °C and 550 °C were also examined by SEM but are not shown here.

The SEM images in Fig. 4.1(a) and (c) show that the microstructures of both steels are similar in the as-quenched state. Two types of regions exist: auto-tempered regions which contain small iron-carbides and non-tempered regions which are smooth and carbide-free [11]. The area fraction of tempered martensite in the as-quenched state is larger in the Ti-containing steel. The SEM images in Fig. 4.1(b) and (d) show that the microstructures of both steels consists of tempered martensite with cementite particles after tempering at 550 °C for 60 min.

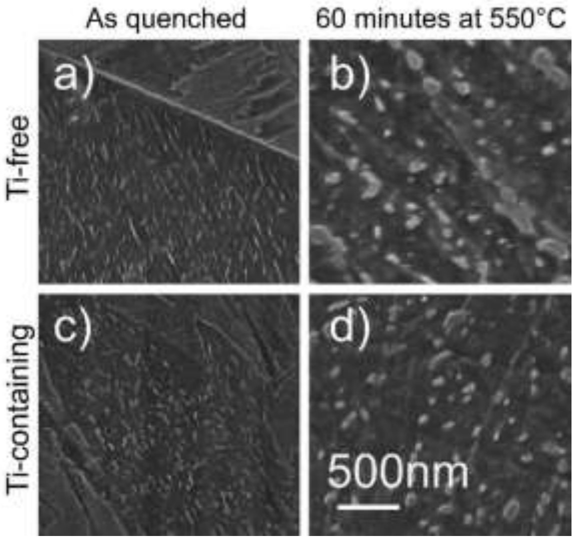

Figure 4.1 *SEM pictures of nital-etched specimens showing the Ti-free martensite and the Ti-containing martensite in the following two states: as-quenched in (a) and (c) and after tempering for 60 min at 550 °C in (b) and (d).*

Fig. 4.2 shows the average cementite particle radius and number density as a function of annealing time during annealing at 300 °C and 550 °C, which are derived from the SEM images.

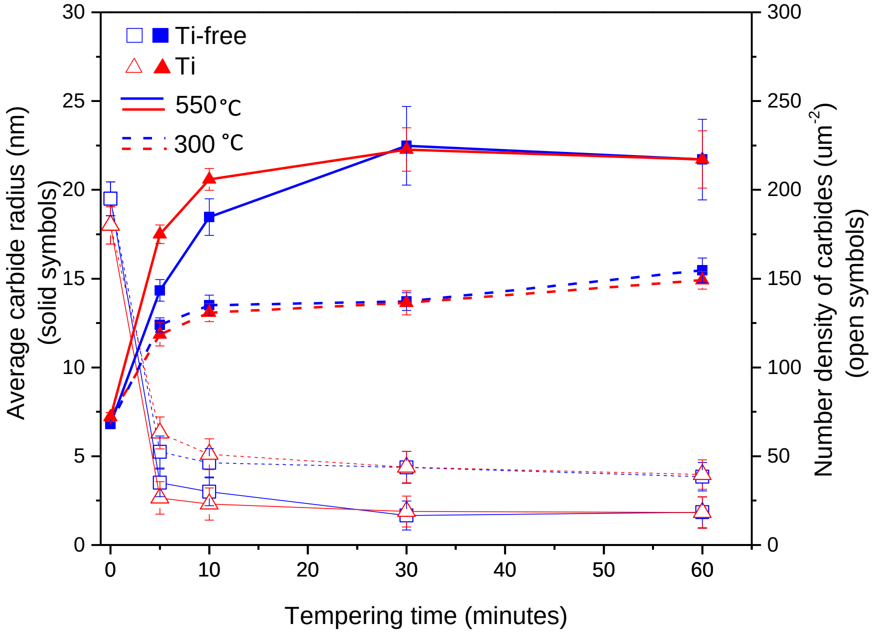

Figure 4.2 *Cementite carbide size and number density as a function of annealing time during annealing at 300°C and 550°C as measured in the Ti-free and the Ti-containing martensite. The error-bars represent a 95% confidence interval.*

We observe that the average cementite particle size is larger during annealing at 550°C than during annealing at 300°C, for each annealing time. Furthermore, we observe that the average cementite particle size is larger in the Ti-containing martensite than in the Ti-free martensite during the first 10 min of tempering at 550 °C. Both steels show comparable carbide sizes during tempering at 300 °C. The number density of cementite particles decreases rapidly between 5-10 min and is thereafter decreasing at a slower rate.

4.3.2 Martensite block size and area fraction of block boundaries and regions of high dislocation density

Fig. 4.3 shows the martensite blocks and the boundaries between the martensite blocks, as measured by EBSD, of the Ti-free and the Ti-containing martensite after quenching and after tempering at 550 °C for 60 min.

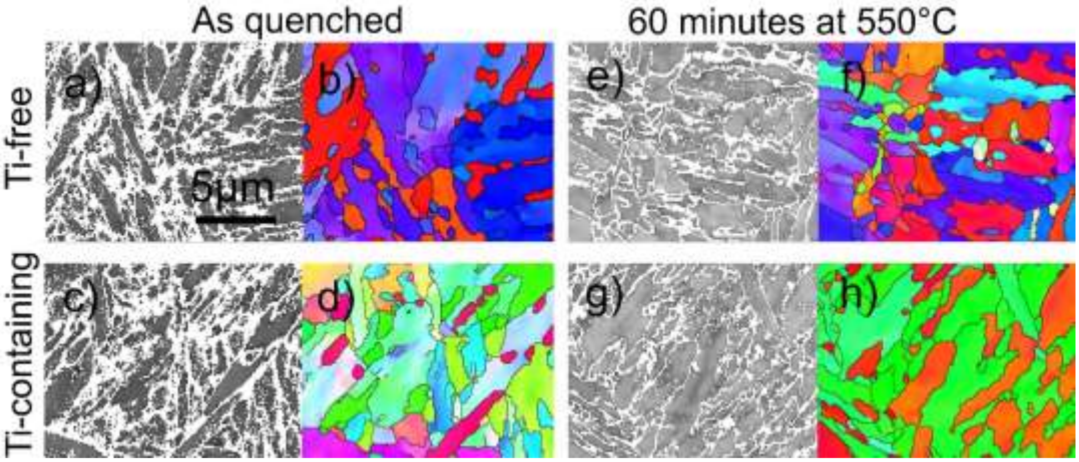

Figure 4.3 *EBSD-images of the microstructure showing Ti-free and Ti-containing martensite in the as-quenched state (a-d) and after annealing at 550°C for 60minutes (e-h). The left panel shows the band contrast prior to noise reduction where non indexed points show as white pixels and the right panel shows the inverse pole figure (IPF) maps after noise reduction where grain boundaries exceeding 10° misorientation are represented as black lines.*

The left hand panels (Fig. 4.3(a), (c), (e) and (g)) show the band contrast (BC) prior to noise reduction: dark grey regions indicate poor band contrast, light grey regions indicate good band contrast, and white regions indicate such poor band contrast that crystallographic indexing is not possible. Degradation of the band contrast typically arises from surface roughness, grain boundaries, elastic strain, and strain induced by dislocations [26]. We observe that the BC is degraded close to non-indexed (white) regions. Furthermore we observe that the BC is improved and that the width of the non-indexed regions is reduced during annealing (compare Fig. 8.3(a) and (c) with 8.3(e) and (f), respectively).

The right hand panels views (Fig. 4.3(b), (d), (f) and (h)) show the inverse pole figure (IPF) maps of the same EBSD images as the left view (created after noise reduction) where martensite block boundaries are marked by black lines. The martensite block boundaries are defined as boundaries located between two neighbouring pixels which have a misorientation that exceeds 10° in agreement with Morito et al [27-28]. We observe that the block boundaries are located in formerly non-indexed regions.

There is no significant difference (95% confidence interval) comparing the block size of Ti-containing and Ti-free martensite, and no block coarsening takes place during 60 min of annealing at both tempering temperatures. As no grain coarsening take place during annealing and the surface roughness and elastic strain is comparable for all specimens (specimen preparation was the same), we derive that all improvements of Kikuchi pattern quality during annealing is a result of recovery. We note that non-indexed regions cover both martensite block boundaries and areas adjacent to the block boundaries. Indexing of block boundaries is not affected by annealing. The reduction of non-indexed points is therefore representative for recovery within areas of the martensite block matrix that are directly adjacent to the martensite block boundary. We call these regions boundary regions. The boundary regions are expected to consist of parallel laths separated by lath boundaries, similar to the matrix in the centre of the martensite block.

We observe that no significant improvement of indexing takes place after 10 min of annealing. Therefore, we consider the 60 min level to be representative for the fully recovered state within the boundary regions for the annealing temperature applied. The area fraction of non-indexed points is hereafter used to estimate the area fraction of boundary regions and the evolution of recovery within these regions.

4.3.3 TiC-precipitate size

The TEM investigation did not reveal the presence of any TiC-precipitates in the as-quenched state of the Ti-containing steel.

Fig 4.4 shows the APT measurements of the Ti-containing martensite specimen where (a) displays Ti atoms in solid solution and TiC-precipitates and (b) displays C atoms, after 60 min of tempering at 550 °C.

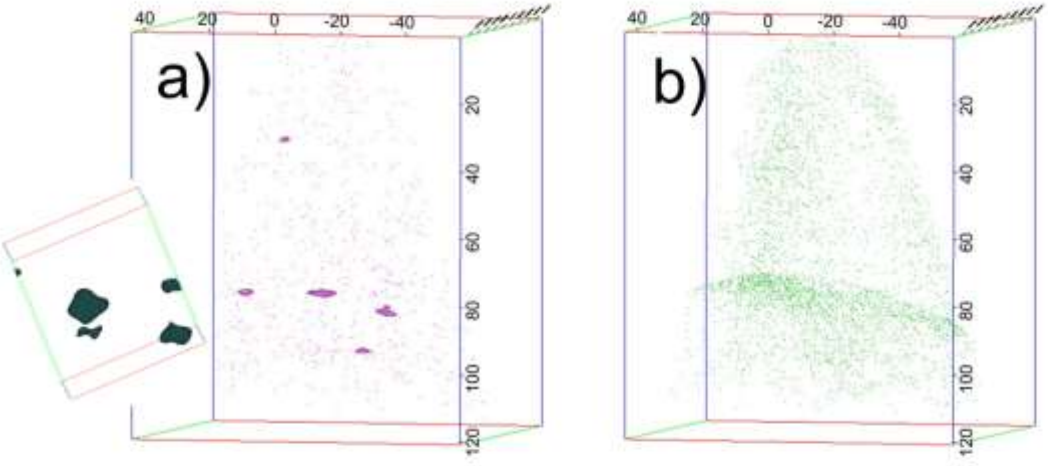

Figure 4.4 *ATP images (90 x 90 x 120 nm) of the Ti-containing martensite after 60 minutes of tempering at 550°C showing (a) distribution of Ti atoms in solid solution and iso-concentration surfaces surrounding TiC-precipitates and (b) distribution of C atoms. The small window in a) shows the five lower TiC-precipitates from the view of the single upper TiC-precipitate*

Fig. 4.4(a) shows that both TiC-precipitates and Ti atoms in solid solution are present in the martensite after 60 min of tempering at 550 °C .The amount of Ti in solid solution is measured to be 0.015 at% which indicate that approx. 67 % of all Ti atoms have precipitated as TiC. The number of Ti atoms in the largest TiC particle is approximately 160 Ti atoms and the smallest particle contains approximately 35 Ti atoms (here the detection efficiency of 37 % has been accounted for). The average precipitate size, based on all six precipitates is 69±46 Ti atoms (standard deviation). 69 Ti atoms correspond to a diameter of 1.39nm.

Fig. 4.4(b) shows that there is an increase in the carbon concentration along a planar feature in the examined volume. This planar feature could correspond to a lath boundary in the martensite [29]. The concentration of carbon atoms in the lath boundary is 0.21 at% and the concentration of carbon atoms in the matrix outside the lath boundary is 0.012-0.030 at%. We observe that five out of the six TiC-precipitates in Fig. 4.4(a) are located on the lath boundary that is visible in Fig. 4.4(b). The average number of atoms in the five precipitates inside the lath boundary is 76±48 Ti atoms (standard deviation).

The small TiC-precipitates in the APT reconstruction are close to spherical and the larger TiC-precipitates appear to be more ellipsoidal. We expect that some degree of compression in the analysis direction can take place and the true shape of the larger precipitate can therefore be closer to spherical. APT measurements on specimens with shorter annealing time were not performed due to that the expected TiC precipitate sizes in these samples are too small to allow us to accurately differentiate between local fluctuations or possible Ti atom segregation and TiC precipitates.

4.3.4 Hardness in matrix and boundaries

Fig. 4.5 shows the (a) macroscopic hardness and (b)-(c) the nano-hardness of the boundary regions and the matrix of both steels as a function of annealing time at 300 °C and at 550 °C.

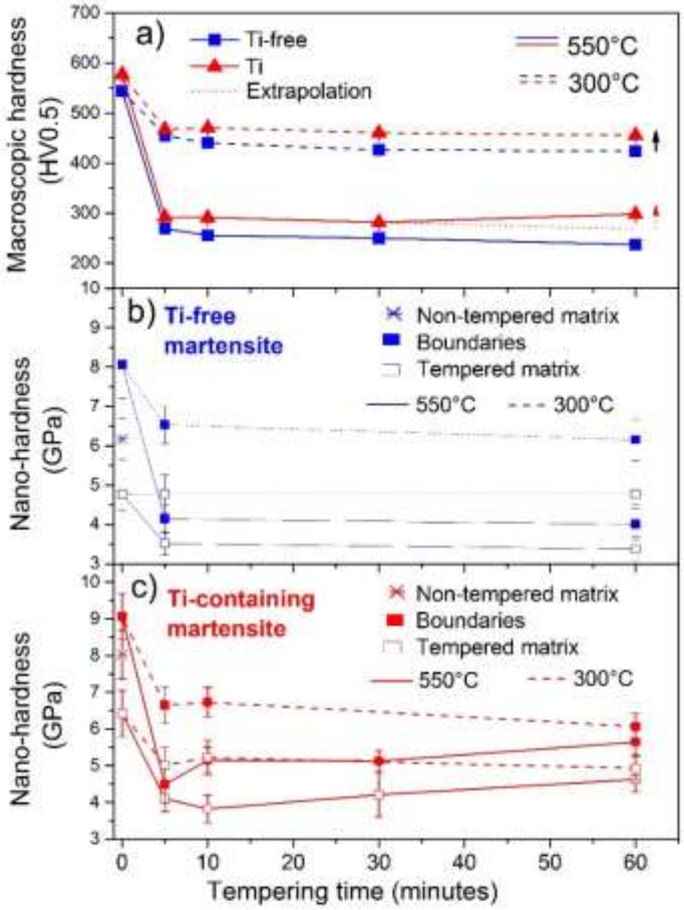

Figure 4.5 *Martensite hardness measured as a function of annealing time at 300°C and 550°C showing (a) the Microvickers hardness (HV0.5) of both steels and (b)-(c) the nano-hardness measurement the Ti-free martensite and the Ti-containing martensite respectively, where the nano-hardness of boundaries, non-tempered matrix and matrix are separated. The extrapolated line in (a) represents the expected martensite hardness if no TiC nucleation would take place and the black arrow shows the hardness increase due to Ti in solid solution. The error-bars represent a 95% confidence interval*

Fig. 4.5(a) shows that the addition of Ti to the steel increases the macroscopic hardness of the steel. Both steels soften rapidly during early stages of annealing, where a higher annealing temperature result in a higher degree of softening. After 10 min of annealing the softening decreases or stops. We observe a hardness increase (approx. 18 HV) for the Ti-containing martensite between 30 and 60 min of annealing at 550 °C.

Fig. 4.5(b)-(c) shows the nano-hardness of the tempered matrix (both auto-tempered and normal tempered regions), non-tempered matrix and of boundaries, measured at 60 nm depth, as a function of annealing time for (b) the Ti-free martensite and (c) the Ti-containing martensite at 300 °C and at 550 °C. Only one data point exists for non-tempered matrix, at *t*=0 minutes, because these regions disappear within 5 min of annealing. We observe that both steels have a higher nano-hardness in the boundaries as compared to the tempered matrix, for each tempering time, at both annealing temperatures.

Fig. 4.5(b) shows that the majority of the nano-hardness reduction in all regions of the Ti-free martensite takes place during the first 5 min of annealing. After 5 min no significant further softening takes place for both annealing temperatures.

Fig. 4.5(c) shows that the nano-hardness reduction of the Ti-containing martensite at 300 °C is similar to the nano-hardness reduction of Ti-free martensite, the majority of the hardness reduction takes place during the first 5 min of annealing and thereafter no further softening take place. However, at 550 °C we observe an increase of the boundary nano-hardness in the Ti-containing martensite between 5 and 10 min of annealing followed by a nano-hardness increase of the matrix between 10 and 30 min. We furthermore observe that the average nano-hardness of the boundaries remains unchanged between 10 and 30 min and that after 30 min the nano-hardness of both the boundaries and the tempered matrix increase in parallel.

4.4 Discussion

4.4.1 Hardness and microstructure evolution

The influence of Ti in solid solution is a macroscopic hardness increase estimated to 32 HV (marked with a black arrow in Fig. 4.5(a)). This is estimated by comparing the Ti-free and the Ti-containing steel during annealing at 300 °C and by knowing that no TiC-precipitates were present after quenching and that no TiC-precipitates nucleate at 300 °C [8-9]. The influence of TiC precipitates on the macroscopic hardness of martensite can be observed first after 30-60 min of annealing at 550 °C, see Fig. 8.5(a). The measured hardness increase of 16 HV shows that the TiC-precipitates we observe by APT have added precipitation strengthening to the steel. We calculate the precipitate strengthening after 60 minutes of annealing according to [30]:

$$\sigma_p = \frac{0.538Gbf^{1/2}}{d_p} ln\left(\frac{d_p}{2b}\right), \qquad \textbf{Equation 4.1}$$

where G is the shear modulus (81600 MPa for iron), b is the Burgers vector in iron, f is the volume fraction of TiC and d_p is the average precipitate diameter of 1.39 nm (69 Ti atoms acc. to APT). The volume fraction of TiC is 67% of the equilibrium volume fraction (0.00084) as measured by APT and calculated by ThermoCalc, (TCFE6). The strengthening effect is approx. 105 MPa which correlate to approx. 35 HV, according to the conversion R_p (in MPa)=3.0 HV [29]. This precipitation hardening effect is counteracted by the redistribution of Ti atoms from solid solution to TiC, where 67 % of the solid solution strengthening effect will disappear. This correspond to a hardness reduction of approx. 21.4 HV. We furthermore calculate that the smallest precipitate size which gives a strengthening effect to the martensite is approximately 35 Ti atoms. The net effect of TiC precipitates on the Ti-containing steel can be estimated using two methods. The first method is the linear addition of the hardening mechanisms [31], which have been suggested for quenched low carbon martensite. The second method is based on separate treatment of dislocations and hard particles [32] and had successfully been applied on high strength low alloy aluminium.

Linear addition results in a net hardness increase of approx. 13.6 HV, which is in good agreement with the measured hardness increase of 16 HV and the approximation in Fig. 4.5(a) (see the extrapolated line in Fig. 4.5(a)). For the separate treatment of dislocations and hard particles we need to consider the recovery of the martensite.

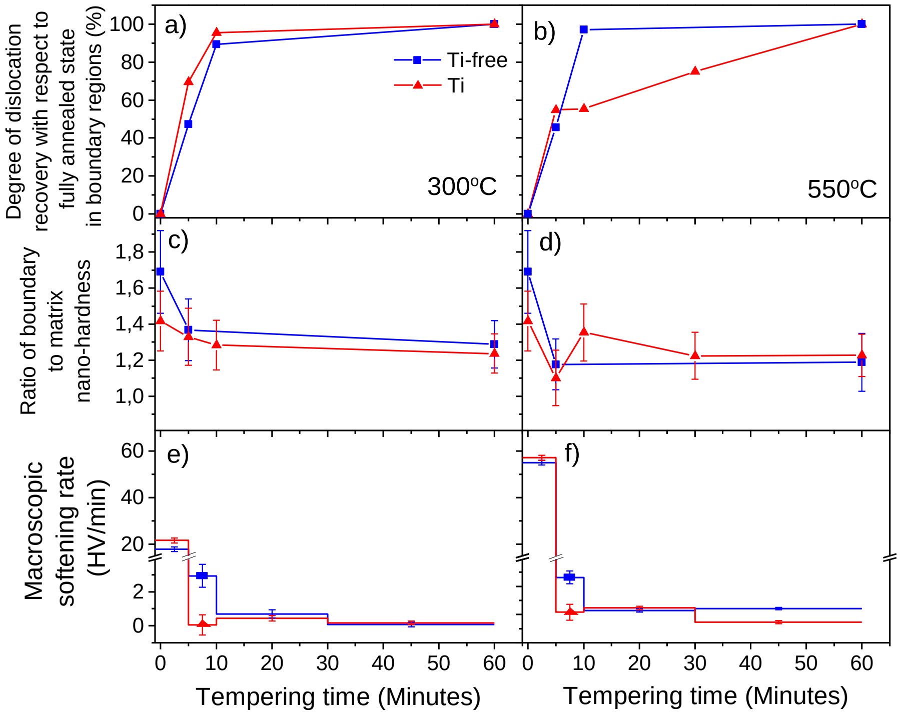

Figure 4.6 *The influence of Ti in solid solution and TiC during annealing at 300°C and 550°C showing (a-b) the degree of dislocation recovery, (c-d) the ratio of boundary and matrix nano-hardness and (e-f) the macroscopic softening rate as a function of annealing time for both Ti-free and Ti-containing martensite. The left column shows annealing temperature 300°C and the right column shows annealing temperature 550°C. The error-bars represent a 95% confidence interval.*

Fig. 4.6 shows the effect of Ti in solid solution and as TiC-precipitates on the hardness and microstructure evolution of martensite during annealing at 300°C (left column) and at 550 °C (right column). Fig. 4.6(a)-(b) shows the evolution of dislocation recovery, with respect to the fully annealed state, in boundary regions (a) at 300°C and (b) at 550 °C. The degree of recovery is calculated from the EBSD indexing results. We consider the indexing result measured at 60 min to be representative for full recovery (100%) at the respective tempering temperature, and the indexing result in the as-quenched state to be representative for 0 % recovery. We observe that the evolution of recovery is similar in both steels during annealing at 300 °C. As no TiC-precipitates are present at this tempering temperature, we conclude that Ti atoms in solid solution have no effect on the recovery rate.

Annealing at 550 °C results in different recovery evolution in the Ti-free and the Ti-containing steel. The Ti-free steel is similar to the two steels at 300°C; rapid recovery during the first 10 min, followed by no recovery during the remainder of the 60 min. The lack of recovery after 10 min of annealing and the EBSD map (see Fig. 4.3(e)) suggest that the non-indexed regions, which remain in the Ti-free steel after 10 min of annealing, mainly consist of martensite block boundaries.

The Ti-containing steel shows a delay in the recovery process between 5 and 10 minutes (at 55 % of the fully recovered level), followed by slow recovery from 10 to 60 min. At 60 min the Ti-containing steel reaches a similar recovery level as the Ti-free steel. The complete recovery stop between 5-10 min indicates that the dislocations present at 5 min are pinned and cannot annihilate. The pinning of the dislocations is believed to be caused by the presence of TiC precipitates. We calculate the hardness contribution to the steels, due to dislocation strengthening, at different annealing times according to the expression derived by Bailey and Hirsch [29, 33]:

$$\sigma = M\alpha G b \rho^{1/2}, \qquad \textbf{Equation 4.2}$$

where α is the dislocation hardening factor, M is the Taylor factor ($M\alpha =$0.34 for pure iron [34]) and ρ is the dislocation density. The dislocation density in the as-quenched state is set to the average value of 14.2×10^{14} m^{-2} [35] and the dislocation density after full recovery at 550 °C is set to $0.025\rho_{AsQ}$ [36]. The dislocation density after 5 min of annealing at 550 °C correlate to 55 % of the fully recovered state (see Fig. 4.6(b)).

The hardness contribution to the steel due to dislocation strengthening in the fully recovered state is expected to be homogeneous in the material (no boundary regions remain) and is calculated to 15 HV for both steels.

The hardness contribution due to dislocation strengthening after 10 min of annealing is different in the Ti-free and the Ti-containing steel. The Ti-free steel will have a hardness contribution that reflects a fully recovered structure (15.0 HV), whereas the hardness of the Ti-containing steel is affected by the boundary regions where recovery only has reached 55 % of the fully recovered level. The boundary regions in the Ti-containing steel (excluding the block boundaries) account for 9 % of the material and have a higher hardness due to the higher dislocation density. The average hardness contribution due to dislocation strengthening of the Ti-containing steel, taking the boundary regions into account, is thereby calculated to be 19.0 HV. This higher degree of dislocation induced hardness is however counteracted by the hardness loss caused by redistribution of titanium and carbon atoms from solid solution to TiC via nucleation of TiC-carbides in the boundary regions. These newly nucleated TiC precipitates are most likely smaller than 35 atoms, and will not add any precipitate strengthening. Linear addition of the hardening mechanisms is therefore possible. We estimate that the hardness loss due to reduction of Ti atoms in solid solution caused by the nucleation of TiC-precipitates in the time interval between 5 and 10 min, is approx. 3.9 HV. We here assume that the critical TiC nucleus size is 14 Ti atoms (one unit cell of TiC), which is approx. 18 % of the average TiC-precipitate size we measure in the laths after 60 min of annealing by APT. We furthermore assume that no further nucleation of new precipitates take place after 10 min as the TiC nucleation rate is reported to be high [21]. The hardness decrease due to depletion of Ti atoms in solid solution during nucleation is therefore expected to be approx. 18 % of the total hardness reduction due to depletion of Ti atoms from solid solution as measured after 60 min of annealing at 550 °C (21.4 HV acc. to earlier paragraph). The hardness change of the Ti-containing steel at 10 min of annealing due to dislocation density and redistribution of Ti atoms is therefore close to 0 HV (not taking the depletion of carbon atoms into account). We now compare the methods of linear addition [32] and separate treatment of dislocations and hard particles [32] to estimate the net hardness increase of the Ti-containing steel after 60 min of annealing at 550 °C, including precipitation strengthening of TiC, Ti atoms in solid solution and dislocation strengthening. Linear addition predict a net hardness increase (comparing the state after 10 min of annealing and the state after 60 min of annealing) of 5.7 HV and the separate treatment of dislocations and hard particles predict a hardness reduction of 6.2 HV. We conclude that linear addition is suitable for martensitic steel containing TiC precipitates.

Fig. 4.6(c)-(d) shows the ratio of the boundary-to-matrix nano-hardness, as a function of annealing time, calculated from the nano-hardness measurements (c) at 300 °C and (d) at 550 °C. The evolution of the ratio of boundary to matrix nano-hardness shows if the nano-hardness evolution is different in these two regions during annealing. Fig. 4.6(c) shows that the evolution of the nano-hardness ratio is similar for the Ti-free and the Ti-containing martensite during annealing at 300 °C. Therefore, we conclude that Ti atoms in solid solution have little effect on the nano-hardness evolution of martensite. Fig. 4.6(d) shows that the nano-hardness ratios of the two steels are similar during the first 5 min of annealing at 550°C. This indicates that nucleation of TiC precipitates has not yet taken place. However, between 5 and 10 min of annealing at 550°C the nano-hardness ratio is increased in the Ti-containing martensite followed by a decrease between 10 and 30 min of annealing at 550°C. The ratio increase is believed to be the result of the nucleation of TiC-precipitates in the boundary regions close to the block boundaries. The higher dislocation density of boundary regions promotes faster TiC nucleation due to a higher number of possible nucleation sites (the nucleation of TiC-precipitates is reported to take place on/near dislocations [16, 18-19]) and the possibility of rapid pipe diffusion for solute Ti atoms. Fig. 4.5(c) clearly shows a small increase in nano-hardness of the martensite block boundary regions and a parallel decrease in the nano-hardness in the matrix during annealing from 5-10 min at 550 °C. The former can be the result of the small hardness increase caused by a lower degree of recovery due to TiC nucleation in boundary regions and the latter indicates that nucleation of TiC-precipitates has not started yet in the matrix. The reduction in the nano-hardness ratio between 10 and 30 min annealing at 550°C for the Ti-containing steel is the result of the onset of TiC nucleation in the matrix (see the hardness increase of the matrix in Fig. 6c during annealing between 10-30 min at 550°C). After 30 min of tempering the ratio remains unchanged as the nano-hardness of the boundaries and the matrix increase in parallel (see Fig. 8.6(c)).

Fig. 4.6(e)-(f) shows the macroscopic softening rate during annealing, as a function of annealing time (e) at 300°C and (f) at 550°C, calculated from the macroscopic hardness measurements. We observe that the softening rate is slightly higher in the Ti-containing steel than in the Ti-free steel during the first 5 min of annealing and thereafter (5 to 10 min) the macroscopic softening rate is lower in the Ti-containing steel, at both annealing temperatures. This higher initial (0-5 min) softening kinetics of the Ti-containing martensite is the result of the faster cementite formation in the Ti-containing martensite, as shown in Fig. 4.2, which is in agreement with the fact that titanium is a cementite stabilizer [37].

We furthermore observe that after 30 min of annealing at 550 °C the Ti-containing steel shows a negative softening rate due to the hardness increase measured at 60 min (see Fig. 4.6(a)). The hardness increase is a direct result of precipitation hardening from the TiC-precipitates we observe by APT (in the size of approximately 70 Ti-atoms), see Fig. 4.4.

4.4.2 Diffusional TiC-precipitate growth

The high dislocation density of martensite is expected to influence the growth rate of TiC in martensite, as compared to nucleation and growth of TiC in ferrite or austenite. Our results indicate that the nucleation of TiC-precipitates starts earlier in boundary regions (which have a higher dislocation density), than in the matrix of martensite.

We model the growth of spherical TiC-precipitates in martensite according to three different models, in order to investigate the influence of the dislocations on the growth of TiC. In all three models we assume that the nucleation of TiC starts in the regions close to martensite block boundaries after 5 minutes of annealing, based on the measured recovery results (Fig. 4.6(b)).

Furthermore, we model the start of nucleation of TiC-precipitates in the matrix regions between 10-30 min of annealing, based on the increase of the nano-hardness measured for the same time interval (see Fig. 4.5(c), matrix, 550°C, Ti-containing steel). We assume that all TiC-precipitates nucleate at the same time in each region since the nucleation rate of TiC-precipitates in ferrite is reported to be high [21]. The influence of cementite on the growth of TiC-precipitates is considered to be negligible in the calculations, because the majority of the volume fraction of cementite has formed before 5 min of annealing (prior to nucleation of TiC in both regions).

In the first model, the growth is modelled to be controlled by volume diffusion only). In the second and the third model, the growth rate is assumed to be controlled by a combination of volume diffusion and diffusion along dislocations. We use the tracer diffusivity of ^{44}Ti, as measured in large single Fe crystals [38], as the lattice diffusivity of Ti in martensite, $D_L^{Ti/M}$ for all three models. The diffusivity data of Ti in α-iron, as measured by Moll and Ogilvie [39] is not used for the calculations as this data is derived from polycrystalline materials, which is believed to overestimate the lattice diffusivity. We furthermore assume that the concentration of carbon (interstitial element) of the martensite does not influence the diffusivity of Ti (substitution element) [40]. ThermoCalc simulations (TCFE6) show that the atomic fraction of Mn in the TiC phase is in the range of 0.2 at% and we therefore do not expect Mn to have a significant influence on the nucleation and growth of TiC due to partitioning.

4.4.2.1 Volume-diffusion growth

The growth of TiC-precipitates is modelled according to classical diffusion-controlled growth theory. The early stages of precipitate growth, when the diffusion fields of neighbouring TiC grains do not overlap, is described by the Zener model where the radius of a growing precipitate, R_n, as a function of time, is given by [41]:

$$R_n(t) = 2.102\left(\frac{c_0^m - c_{eq}^m}{c_{eq}^{TiC} - c_0^m}\right)^{0,5871} \sqrt{\langle D_{Ti}\rangle (t - t_s)} \qquad \textbf{Equation 4.3}$$

Where t_s is the moment of nucleation and t is the annealing time. c_{eq}^m and c_{eq}^{TiC} are the equilibrium concentrations of Ti in the matrix and in the TiC-precipitate, respectively, and c_0^m is the concentration of Ti atoms in the parent phase far away from the precipitate. $\langle D_{Ti}\rangle$ is the average diffusion coefficient of Ti in martensite.

For the later stages of TiC-precipitate growth, when the diffusion fields have started to overlap, we describe the growth by a model involving the transition from non-overlapping to overlapping diffusion fields developed by Offerman et al [42], see Fig. 4.7.

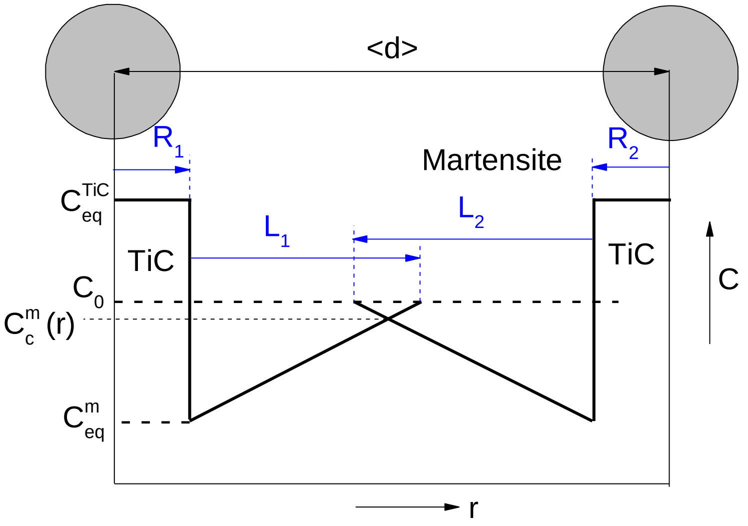

Figure 4.7 *Model for growth of TiC-precipitates involving overlapping diffusion fields. The concentration of Ti-atoms, C_{Ti}, is shown as a function of the distance r where two spherical TiC-precipitates with different radii, R_1 and R_2, are separated by an average distance <d>. Local equilibrium is assumed at the interface of the TiC-precipitates (C_{eq}^{TiC}) and the in the matrix (C_{eq}^m). The overall Ti-concentration of the alloy is indicated by C_0^m. The concentration of Ti-atoms at the position where the two diffusion profiles cross during precipitate growth, C_c^m, is approximated using linear concentration gradients over the distances L_1 and L_2*

The model still uses Zener-type concentration profiles to calculate the velocity of the interfaces but uses linear concentration profiles to estimate the concentration of Ti-atoms at the position where the diffusion fields overlap.

For the growth of TiC-precipitates during overlapping diffusion fields, the Zener model is still used, but the concentration c_0^m in Eq. 4.3. is replaced by c_c^m, which is the concentration of Ti at the position where the linear diffusion profiles intersect:

$$c_c^m = c_0^m - \left(c_0^m - c_{eq}^m\right)\frac{2R+2L-\langle d\rangle}{2L},$$

Equation 4.4

where $\langle d\rangle$ is the average distance between the neighbouring precipitates and the length L of the linear concentration profile is given by [42]:

$$L = \left\{\frac{1}{3}\left(44+54B+6\sqrt{54+132B+81B^2}\right)^{1/3} - \frac{2}{3\left(44+54B+6\sqrt{54+132B+81B^2}\right)^{1/3}} - \frac{4}{3}\right\} R_n$$

Equation 4.5[1]

where

$$B = \frac{c_0^m - c_{eq}^{TiC}}{c_{eq}^m - c_0^m}$$

Equation 4.6

The Gibbs-Thomson effect is accounted for by expressing the Ti concentration at the interface of the growing precipitate according to[43]:

$$c_{eq,r}^m = c_{eq}^m exp\left(\frac{2\sigma v_{at}^{TiC}}{c_{eq}^{TiC} R(t) kT}\right),$$

Equation 4.7

where σ is the surface tension (approx. 0.3J/m^2) [21, 44-45].

The numerical calculation of the TiC-precipitate radius is done according to:

$$R_n = R_{n-1} + \left(\frac{dR}{dt}\right)_{t=t_{n-1}+1/2\Delta t} \cdot \Delta t,$$

Equation 4.8

where R_{n-1} is the radius in the previous time step t_{n-1} and $\Delta t=(t_n-t_{n-1})$. The equilibrium concentration of titanium in the matrix and in TiC at 550°C, c_{eq}^m and c_{eq}^{TiC}, are calculated using ThermoCalc. $c_0^m(t=0)$ is calculated from the initial steel composition, after removing the equilibrium volume fraction of cementite at 550°C (as calculated by ThermoCalc). $\langle D_{Ti}\rangle$ is set to be the lattice diffusion coefficient of Ti in martensite, $D_L^{Ti/M}$.

---

[1] Correction of typing error in the original publication, from $\frac{3}{4}$ to $\frac{4}{3}$

4.4.2.2 Dislocation assisted growth

We model dislocation assisted growth according to two mechanisms. The first mechanism is developed by Wang and Shiflet [46]. This model describes how the growth rate of a precipitate is affected by the diffusion of solute atoms along a *single* dislocation attached to the precipitate, and was successfully applied to the growth of precipitates in a well annealed binary alloy of Al-Li. The second mechanism describes dislocation assisted growth of a precipitate by the diffusion of solute atoms along multiple dislocations that are in close proximity to the precipitate. The effective diffusivity of the solute atoms is described as a net diffusivity of solute atoms through the lattice and along dislocations.

4.4.2.2.1 Single dislocations model

The single-dislocation-assisted growth of spherical precipitates is given by [46]:

$$\frac{dR}{dt}\bigg|_{total} = \frac{dR}{dt}\bigg|_{Lattice} + \frac{dR}{dt}\bigg|_{Pipe},$$

Equation 4.9

where $\frac{dR}{dt}\Big|_{Lattice}$ is expressed via Eq. 4.3-4.8. The growth rate of the TiC-precipitate due to pipe diffusion is expressed as:

$$\frac{dR}{dt}\bigg|_{pipe} = \frac{c_{eq}^{m}-c_{0}^{m}}{c_{eq}^{m}-c_{eq}^{TiC}}\frac{\sqrt{2}r_0}{\pi R^2}\sqrt{D_L^{Ti/M}D_P^{Ti/M}}\sqrt{f(t')}$$

Equation 4.10

$D_P^{Ti/M}$ is the pipe diffusivity of Ti in martensite, r_0 is radius of the cylindrical dislocation pipe, $t' = D_L^{Ti/M}t/r_0^2$ and $f(t')$ is the integral:

$$f(t') = \int_0^{\infty} \frac{\exp(-t'x^2)}{x[J_0^2(x)+Y_0^2(x)]}dx,$$

Equation 4.11

where $J_0(x)$ and $Y_0(x)$ are the zeroth order Bessel functions of the first and second kind respectively. For r_0 we use the Burgers vector in α-iron.

4.4.2.2.2 Multiple dislocations model

The multiple dislocation assisted growth of TiC-precipitates is expressed according to Eq. 4.3-4.8, where $\langle D_{Ti}\rangle$ in Eq. 4.3 is replaced by an expression of the effective diffusivity according to [47]:

$$\frac{\langle D_{Ti} \rangle}{D_L{}^{Ti/M}} = 1 + g\frac{D_p^{Ti/M}}{D_L^{Ti/M}}$$ **Equation 4.12**

where g is the cross sectional area of dislocation pipe per unit area of matrix. We express the ratio of pipe diffusivity to lattice diffusivity, $\frac{D_p^{Ti/M}}{D_L^{Ti/M}}$ for Ti diffusion in martensite via the ratio of pipe diffusivity to lattice diffusivity of iron in iron and a scale factor according to the ratio of diffusivities for Ti and Fe in iron ($D_L^{Ti/Fe}$ and $D_L^{Fe/Fe}$).

$$\frac{D_p^{Ti/M}}{D_L^{Ti/M}} = \frac{D_L^{Ti/Fe}}{D_L^{Fe/Fe}} \cdot \frac{D_p^{Fe/Fe}}{D_L^{Fe/Fe}}$$ **Equation 4.13**

The scale factor, $\frac{D_L^{Ti/Fe}}{D_L^{Fe/Fe}}$ accounts for the different atom radius of Ti and Fe, which is believed to affect pipe diffusion of Ti in iron, according to the same proportion as lattice diffusion of Ti in iron is affected.

The effective pipe radius of a dislocation is set equal to the burgers vector in α-iron, *b*, and we express the cross sectional area of dislocation per unit area of martensite in Eq. 4.12 as:

$$g = \rho \pi b^2,$$ **Equation 4.14**

where ρ is the dislocation density. We extend Eq. 4.12 to include the recovery during isothermal annealing by expressing g as a function of time:

$$g(t) = \rho_{AsQ}\pi b^2 - F(t)\left[\rho_{AsQ}\pi b^2 - \rho_R \pi b^2\right] ,$$ **Equation 4.15**

where ρ_{AsQ} is the dislocation density in the as-quenched state, ρ_R is the dislocation density after recovery and $F(t)$ is a function that describes the evolution of the recovery process. We use the same dislocation densities as in section 4.4.2.1. $F(t)$ is modelled to follow the evolution of dislocation recovery as measured by EBSD (Fig 4.7(b)).

The ratio $\frac{D_p^{Fe/Fe}}{D_L^{Fe/Fe}} = 57100$ at 550°C [48] and $\frac{D_L^{Ti/Fe}}{D_L^{Fe/Fe}}$ is calculated to be 0.30 at 550°C [49].

4.4.3 Comparison of TiC growth models

Table 4.2 shows the calculated average precipitate sizes after 60 min of annealing at 550 °C in boundary and matrix regions for all three models and the APT measurements. We assume that the precipitates measured in the lath boundary is representative for boundary regions due to the high dislocation density of martensite laths. The volume diffusion model predicts too small precipitate sizes, and we therefore conclude that pipe diffusion strongly contributes to the growth of TiC in martensite.

Table 4.2 *Precipitate size (number of Ti atoms)*

Kinetics	Volume diffusion	Diffusion along single dislocation	Diffusion along multiple dislocations	Measured by APT (Standard deviation)	Number of measurements (APT)
Boundary	21	252	91	76±48	5
Matrix	17-20	168-236	68-85	35	1

Table 4.2 furthermore shows that the single dislocation model overestimates the precipitate size. The reason for the overestimated precipitate size by the single-dislocation model is that the size of the TiC-precipitates within this research is so small that pipe diffusion becomes dominant in the model (small values for the radii results in high values of the term $\frac{\mathrm{r}_0}{\mathrm{R}^2}$ in Eq. 4.8). The single dislocation model does also not take into account the reduction in the dislocation density due to recovery. Moreover, as Wang and Shiflet [46] point out, the model does not take into account the competition for Ti atoms between neighbouring TiC precipitates along the same dislocation line, which would slow down precipitate growth.

The multiple dislocation-assisted growth model predict TiC-precipitate sizes which are in agreement with the APT measurement. The model takes into account the recovery, which means that the model takes into account a reduction in the overall diffusivity of Ti-atoms due to the reduction in dislocation density.

4.5 Conclusions

Two martensitic steels with and without the addition of 0.042 wt.% of Ti are compared at annealing temperatures of 300 °C and 550 °C. The macroscopic hardness in both steels and at both temperatures reduces quickly during the first 5 min of tempering, due to the redistribution of interstitially dissolved carbon into cementite and due to rapid recovery. The macroscopic hardness remains more or less the same during continued annealing, except for the Ti-containing steel that is tempered at 550 °C. This is related to the formation of TiC-precipitates at 550 °C. Nucleation of TiC-precipitates starts first in the regions close to the martensite block boundaries (between 5-10 min) and thereafter in the block matrix (between 10-30 min) during annealing at 550°C, due to the higher dislocation density in the regions close to the block boundaries. The formation of TiC-precipitates has the following effects on the evolution of the microstructure and the hardness:

1. TiC-precipitates slow down the recovery in the regions close to the martensite block boundaries compared to the alloy without TiC-precipitates.
2. The TiC-precipitates increase the macroscopic hardness of the steel after 30 min annealing at 550 °C.

The growth of TiC-precipitates in martensite is simulated with three models: 1) a model taking into account capillarity effects and the overlap of the titanium diffusion fields, 2) a model that takes into account the above effects plus the effect of the diffusion of titanium atoms along a single dislocation attached to the precipitate, and 3) a model that takes into account the effects of the first model and the effect of pipe diffusion of titanium atoms via multiple dislocations. The third model predicts a TiC-precipitate size that correspond the closest to the experimentally observed TiC-precipitate sizes.

4.6 References

[1] ISO898-1, Mechanical properties of fasteners made of carbon steel and alloy steel-Part 1. Fifth edition, Switzerland, 2013
[2] EG. Dere, H. Sharma, RH. Petrov, J. Sietsma and SE. Offerman: Scr. Mater., 68(2013), 651
[3] LS. Kremnev: Metal. Sci. Heat. Treat., 33(1991), 428
[4] RF. Buck and WMJr. Garrison: Adv. Mater. Process. 150(1996), 27
[5] RL. Klueh, N. Hashimoto, RF. Buck and MA. Sokolov: J Nucl Mater., 283-287(2000), 697
[6] F. Abe, M. Taneike and K. Sawada: K,: Int. J. Press. Vessel Pip., 87(2007), 3
[7] M. Taneike, M. Fujitsuna and F. Abe: Mater. Sci. Technol., 20(2004), 1455
[8] F-G. Wei, T Hara, T. Tsuchida and K Tsuzaki: ISIJ Int. 43(2003), 539
[9] F-G. Wei, T. Hara and K. Tsuzaki: Metall Mater. Trans. B., 35b(2004), 587
[10] J. Takahashi, K. Kawakami, Y. Kobayashi and T. Tarui: Scr. Mater., 63(2010), 261
[11] CEIC. Ohlund, SE. Offerman and E. Schlangen: Mater. Sci. Eng. A., 560(2013), 351
[12] T. Ohmura, M. Hayakawa, K. Miyahara, S. Matsuoka, K. Tsuzaki and T. Takahashi: Proc. of 20th Riso Int. Symp. on Materials Science, Roskilde, Denmark,(1999), 433
[13] T. Ohmura, T. Hara and K. Tsuzaki: Scr. Mater., 49(2003), 1157
[14] T. Ohmura, AM. Minor, EA. Stach and JWJr. Morris: .J Mater. Res. 19(2004), 3626
[15] DM. Barnett: Scr. Metall., 5(1971), 261
[16] W. Kesternich: Philos. Mag. A., 52(1985), 533
[17] SQ. Xiao and P Haasen: Scr. Metall., 23(1989), 365
[18] P. Gopalan, R. Rajarman, B. Viswanathan, KP. Gopinathan and S. Venkadesan: J. Nuc. Mat., 256(1998), 229
[19] SY. Hu, and LQ. Chen: Acta Mater., 49(2001), 463
[20] Z. Wang, X. Mao, Z. Yang, X. Sun, Q. Yong, Z. Li and Y. Weng: Mater. Sci. Eng. A., 529(2011), 459
[21] M. Sawahata, M. Enomoto, K. Okuda and T. Yamashita: Tetsu-to-Hagane., 94(2008), 21
[22] MHF. Overwijk, FC. Van den Heuvel and CWT.Bulle-Lieuwma: J. Vac. Sci. Technol. B., 11(1993), 2021
[23] DJ. Larson, DT. Foord, AK. Petford-Long, TC. Anthony, IM. Rozdilsky, A Cerezo and GWD. Smith: Ultramicrosc., 75(1998), 147
[24] M. Thuvander, J. Weidow, J. Angseryd, LK. Falk, M. Sonestedt, K. Stiller and HO. Andre’n: Ultramicrosc., 111(2011), 604
[25] WC. Oliver and GM Pharr: J. Mater. Res., 7(1992), 1564
[26] SI. Wright and MM. Nowell: Microsc. Microanal., 17(2011), 316
[27] S. Morito, H. Tanaka, R. Konishi, T. Furuhara and T. Maki: Acta Mater., 51(2003), 1789
[28] S. Morito, X. Huang, T. Furuhara, T. Maki and N. Hansen: Acta Mater., 54(2006), 5323

[29] D. Hutchinson, J. Hagstrom, O. Karlsson, D. Lindell, M. Tornberg, F. Lindberg and M. Thuvander: Acta Mater., 59(2011), 5845
[30] T. Gladman: Mat. Sci. Tech., 15(1999), 30
[31] LA. Nordstrom: Scand. J. Metall., 5(1976), 159
[32] E. Hornbogen, EA. Starke Jr. : Acta Metall., 45(1993), 1.[33] Y. Han, J. Shi, L. Xu, WQ. Cao and H. Dong: Mater. Sci. Eng. A., A530(2011), 643
[34] G. Thomas, J. Washburn: Electron Microscopy and Strength of Crystals, Interscience Publ, New York, USA, 1963
[35] S. Morito, J. Nishikawa and T. Maki: ISIJ Int., 43(2003), 1475
[36] S. Takebayashi, T. Kunieda, N. Yoshinaga, K. Ushioda and S. Ogata: ISIJ Int., 50(2010), 875
[37] CK. Ande and MHF. Sluiter: Acta Mater., 58(2010), 6276
[38] P. Klugkist and C. Herzig: Phys. Status. Solidi. (a)., 148(1995), 413
[39] SH. Moll and RE. Ogilvie: Trans MS AIME., 215(1959), 613
[40] A. Borgenstam, A. Engstrom, L. Hoglund and J. Agren: J. Phase Equilibria., 21(2000), 269
[41] SGE. Te Velthuis, NH. Van Dijk, MTH. Rekveldt, J. Sietsma and S. Van der Zwaag: Mater. Sci. Eng. A., 277(2000), 218
[42] SE. Offerman, NH. Van Dijk, J. Sietsma, EM. Lauridsen, L. Margulies, S. Grigull, HF. Poulsen and S. Van der Zwaag: Acta mater., 52(2004), 4757
[43] M. Perez M: Scr. Mater., 52(2005), 709
[44] JH. Jang, CH. Lee, YU. Heo and DW. Suh: , Acta Mater., 60(2012), 208
[45] DHR. Fors and G. Wahnstrom: Phys. Rev., 82(2010), 195410-1
[46] ZM. Wang and GJ. Shiflet: Metall. Mater. Trans., 29A(1998), 2073
[47] DA. Porter and KE. Easterling: Phase transformations in metals and alloys, Van Norstrand Reinhold, New York, USA (1981)
[48] Y. Shima, Y. Ishikawa, H. Nitta, Y. Yamazaki, K. Mimura, M. Isshiki and Y. Iijima: Mater. Trans. 43(2002), 173
[49] FF. Buffington, K. Hirano and M. Cohen: Acta Metall., 9(1961), 434

5 Modelling the evolution of multiple hardening mechanisms during tempering of Fe-C-Mn-Ti martensite

C. Emmy I. C. Ohlund, Dennis den Ouden, Jonathan Weidow, Mattias Thuvander and S. Erik Offerman

ISIJ International, Vol. 55 (2015), No. 4, pp. 883-892

Abstract

We model the hardness evolution of martensite during tempering as a linear addition of multiple hardening mechanisms that is combined with a microstructural Kampmann-Wagner-Numerical (KWN) model to simulate the nucleation and growth of TiC-precipitates during tempering. The combined model is fitted to the measured hardness evolution during tempering at 300°C and 550°C of the martensitic steels with and without the addition of titanium. The model predicts TiC-precipitate sizes in agreement with experimental observations and generates fitting parameters in good agreement with literature. The microstructural components that give the highest contribution to the overall hardness are Fe_3C precipitates (88 HV) and dislocations (54 HV). Both Fe_3C- and dislocation-strengthening decreases rapidly during the initial stage and stabilise after 10 minutes of tempering. The model shows that the decrease in dislocation density due to recovery is slowed down due to the presence of TiC-precipitates. Titanium atoms in solid solution give a stable hardness contribution (25 HV) throughout the tempering process. TiC-precipitate strengthening generates a minor contribution (3.5 HV). The model shows that less than 1% of the equilibrium volume fraction of TiC-precipitates forms during isothermal tempering at 550 °C due to the large misfit strain (1.34 GJ/m^3) and a limited density of potential nucleation sites in the martensite. The model shows that the hardness of tempered martensitic steels could potentially be increased by increasing the TiC-precipitate density by reducing the misfit strain.

5.1 Introduction

Tempered martensitic steel is the most commonly used material for high-strength fasteners in mass-produced car engines today [1]. These steels fulfil the typical requirements for the service conditions of fasteners used in current passenger cars: ultimate tensile strengths up to 1200 MPa and a recommended service temperature of max 300 °C. However, the ongoing trend of engine down-sizing in order to reduce weight and CO_2-emmissions results in higher mechanical and thermal loading of the engines. Stronger and yet tough steels are now required for engine fasteners. An important boundary condition for fastener steels is a low concentration of alloying elements that are abundantly available in order to assure cost efficiency and suitability of the steel for cold forging.

The strength of martensite originates from multiple strengthening mechanisms: 1) elements in solid solution, 2) grain boundaries, 3) dislocations, and 4) precipitates [2]. The strength of martensite is therefore a complicated function of the martensite microstructure as this evolves during tempering of the martensite. The microstructure of martensite consists of the parent austenite grain structure which is sub-divided into packets. Each packet is divided into blocks and each block consists of parallel laths which are divided by walls of dislocations (lath boundaries) [3]. Moreover, the microstructure of martensite consists of free dislocations, carbides, carbon atoms and other alloy atoms in solution. The carbon atoms are present in solid solution, as atoms segregated into lattice defects such as dislocations and/or as part of the different carbides. Substitutional alloying elements such as Ti are present in solid solution or in carbides.

The traditional fastener steels with strength levels up to 1200 MPa, such as 33B2 and 34Cr4, are essentially based on the first three strengthening mechanisms mentioned above. New steels for stronger fasteners have now been developed with additional strengthening from precipitates according to similar principles as used in HSLA steels [4]. Precipitates of V- and Ti-carbides are used to increase the strength to levels higher than 1200 MPa [5].The tempering temperature which is required for the nucleation and growth of secondary V or Ti-containing precipitates is above 500 °C, which fits with the requirements of the fastener standard ISO 898-1 [1] and the low alloy additions enable the steel to be suitable for cold forming. More importantly, TiC-precipitates have the potential to act as hydrogen traps and improve the resistance to hydrogen-induced damage [6] during processing and service of the fastener. In addition to enhancing strength, thermally stable precipitates are also known to improve the temperature resistance of steels, by acting as pinning points for movement of dislocations [7]. The high thermal stability of TiC precipitates [8] therefore makes medium-carbon steel with a small addition of Ti an interesting candidate for high-strength engine fasteners intended for service temperatures which exceed the current limit of 300 °C. The mechanical properties of such fasteners will be directly related to the martensite microstructure with precipitates. Fundamental understanding of the evolution of the microstructure and the resulting hardness during tempering of martensite with small additions of Ti is required to optimise the heat treatment process and the mechanical properties of the fastener.

The aim of this study is to model the evolution of the multiple hardening mechanisms during tempering of Fe-C-Mn-Ti martensite. We simulate the hardness evolution of martensite via linear addition of the hardening mechanisms. This hardness model is combined with a microstructural multi-component and multi-phase Kampmann-Wagner-Numerical (KWN) model as developed by Den Ouden et al. [9], for the simulation of TiC-precipitate nucleation and growth during tempering. The KWN-model takes into account the distribution of carbon atoms between phase fractions of TiC- and Fe_3C-precipitates. Moreover, the model simulates the evolution of recovery in order to estimate the effective diffusivity of Ti-atoms and in order to estimate the number of available nucleation sites for TiC-precipitates. The combined models are fitted to the experimental work of Öhlund et al. presented in ref [10].

5.2 Modelling the evolution of multiple hardness components during tempering

We assume that the separate hardening mechanisms of grain size (gb), solid solution (ss), precipitates (P) and dislocations (d) can be added linearly, in agreement with [2]:

$$\sigma_{tot} = \Delta\sigma_{gb} + \Delta\sigma_{ss} + \Delta\sigma_P + \Delta\sigma_d, \qquad \textbf{Equation 5.1}$$

where $\Delta\sigma_{gb}$ is the hardness contribution from grain boundaries, $\Delta\sigma_{ss}$ is the hardness contribution form elements in solid solution, $\Delta\sigma_p$ is the hardness contribution from precipitates and $\Delta\sigma_d$ is the hardness contribution from dislocations.

The increase of strength due to grain size is simulated by the Hall-Petch relationship is [11]:

$$\Delta\sigma_{gb} = \sigma_l + k_D {d_d}^{-1/2}, \qquad \textbf{Equation 5.2}$$

where σ_l is the lattice friction, k_D the Hall-Petch factor and d_g the average diameter of the martensite grains. d_g is a function of time if grain coarsening takes place.

The effective grain size of martensite is reported to be the block size [12]. A Hall-Petch term has also been suggested for the lath sub-structure within the block, but we choose to include this effect in the term for dislocation density contribution [13], because a lath boundary can be described by a stack of dislocations.

The increase in yield strength due to elements in solid solution, i.e. C, Ti and Mn, is simulated by the general form [14]:

$$\Delta\sigma_{ss,i} = K_i C_i^{n_{s,i}}, \qquad \textbf{Equation 5.3}$$

where K_i is a constant for alloy element i, C_i is the concentration of element i and $n_{s,i}$ is a constant that can vary from 0.5 to 2 depending on the alloying element [14]. The concentrations of C, Ti and Mn in the matrix are functions of time, due to redistribution into TiC and/or Fe_3C.

We set $n_{s,Mn} = 1$ in agreement with [13] and we assume that $n_{s,Ti}$= 1 due to that both Mn and Ti are substitutional atoms.

We do not include the effect of carbon atoms in solid solution in Eq. 5.3. Literature reports that that the well-known square root effect of carbon concentration on martensite yield strength is associated with the dislocation density of the martensite, rather than the solid solution effect of carbon atoms [13, 15]. An increased carbon content of the steel generates a linear increase of the dislocation density of the quenched martensite. Carbon atoms diffuse to the Cottrell atmospheres of dislocation during quenching of the martensite and thereby maintain a higher dislocation density of the martensite, as recovery is hindered via pinning of dislocations by segregated carbon atoms. The dislocation density of martensite also generates a square root contribution to the martensite yield strength (see Eq. 5.5) and the effect of increased carbon concentration on martensite therefore follows the well-established square-root dependency.

The increase in strength due to precipitates is calculated according to the Orowan-Ashby equation [16]:

$$\Delta\sigma_{P,j} = \left(\frac{0.538 G b f_j^{1/2}}{2 r_{p,j}}\right) \cdot \ln\left(\frac{r_{p,j}}{b}\right), \qquad \textbf{Equation 5.4}$$

where G is the shear modulus of the matrix (calculated to be 80.4 GPa by a linear interpolation between the systems of Fe and Fe-1C at as concentration of 0.4 wt.%C [17]), b is the length of the Burgers vector (0.248 nm [18]), f_j is the volume fraction of precipitate phase j and $r_{p,j}$ is the average precipitate radius of phase j (TiC and Fe_3C). f_j and $r_{p,j}$ are functions of time due to the nucleation and growth of Fe_3C- and TiC-precipitates.

The increase in yield strength by dislocations is calculated according to [19]:

$$\Delta\sigma_d = M\alpha Gb\rho^{1/2},$$ **Equation 5.5**

where M = 2.733 (the Taylor factor) [20] and α (an empirical parameter) are constants. The dislocation density, ρ, is a function of time due to recovery. Recovery is in turn affected by the number of precipitates present in the material, as precipitates pin dislocations. The effect of precipitates on the recovery kinetics can be described according to [19] by

$$\frac{d(\Delta\sigma_d)}{dt} = \left[-\frac{64\left(\Delta\sigma_\rho\right)^2\nu_d}{9M^3\alpha^2E}\exp\left(-\frac{U_a}{k_BT}\right)\sinh\left(\frac{\Delta\sigma_\rho V_a}{k_BT}\right)\right]\left(1-\frac{N(t)}{N_c(t)}\right) \text{ for } N<N_c \text{ and}$$

$$\frac{d(\Delta\sigma_d)}{dt} = 0 \text{ for } N\geq N_c,$$ **Equation 5.6**

where ν_d and E are the Debye frequency and Youngs modulus respectively and α has the same meaning as in Eq. 5.5, U_a and V_a are the activation energy and activation volume for recovery respectively, k_B is the Boltzmanns constant, $N(t)$ is the number density of TiC precipitates and $N_c(t)$ is the total number density of dislocation nodes and T is the temperature. We use the same approximation as [19] for the number of dislocation nodes: $0.5\rho(t)^{1.5}$. Similar to [19], we also approximate ν_d and U_a using the self-diffusivity of iron in martensite [21] and the lattice parameter of martensite [22]. V_a is assumed to be temperature independent. The parameters α and V_a are assumed unknown and will be fitted to the experimental data.
We use Eq. 5.6 to model the evolution of $\Delta\sigma_d$ as a function of time, and we thereafter calculate $\rho(t)$ via Eq. 5.5. We assume that microstructure in the as-quenched state corresponds to 0 % recovery and the dislocation density ρ_{AsQ} in the as-quenched state is 14.2×10^{14} m^{-2}, as found in the literature [23].

The total yield strength of each strengthening mechanism can thereafter be converted to hardness according to [24]:

$$HV = \sigma_{tot}/3.$$ **Equation 5.7**

The unknown parameters in the hardness model are $\sigma_0, K_{Mn}, K_{Ti}, \alpha$ and V_a. The values for f_{Fe_3C} and r_{p,Fe_3C} are obtained from the experimental measurements presented in later sections. The values for f_{TiC} and $r_{p,TiC}$ are obtained from simulations with the multicomponent KWN model which is discussed in the next section. The concentrations of C, Ti and Mn in solid solution can be obtained from the measured and simulated data.

5.3 Modelling the nucleation and growth of TiC-precipitates during tempering

Literature reports that TiC precipitates in steel nucleate near dislocations [25] and that the nucleation rate of TiC is high, followed by slower growth and coarsening [26]. Studies have furthermore shown that both TiC nucleation and growth is enhanced by the presence of dislocations [10]. Literature furthermore reports that the presence of TiC precipitates in martensite affects the evolution of the dislocation density in steel during the heat treatment [10, 18]. The modelling of TiC nucleation and growth in martensite must therefore be linked to dislocation density and recovery in martensite during tempering.

5.3.1 Nucleation of TiC

We assume that the nucleation barrier for TiC nucleation in martensite is lowered via interactions between the strain field surrounding the dislocation and the nuclei, without annihilation of the dislocation core, in agreement with [27-28]. We furthermore assume that at the moment of nucleation the TiC precipitates are coherent with the matrix in three dimensions, which implies a cubic nucleus shape.

The classical nucleation theory describes the change in Gibbs free energy associated with a nucleation event of one such cubic nucleus as:

$$\Delta G = l^3(\Delta g_v + \Delta g_s) + 6l^2\gamma_{eff}, \qquad \textbf{Equation 5.8}$$

where l is the edge of the cubic nuclei, Δg_v is the chemical free energy change per unit of volume due to the formation of the precipitate phase (also called the driving force for nucleation) which has a negative sign in case of an oversaturated matrix, Δg_s is the misfit strain energy due to the formation of the precipitate in the host lattice and γ_{eff} is the effective interface energy of a precipitate which interacts with a nearby dislocation strain field. The effective surface energy is calculated according to [29]:

$$\gamma_{eff} = \gamma - \sqrt[3]{\frac{\pi}{6}}\frac{Gb(1+\nu)}{3\pi(1-\nu)}e^T, \qquad \textbf{Equation 5.9}$$

where γ is the interface energy between TiC and ferrite (0.339 Jm^{-2}) [30], G is the shear modulus of the matrix, ν the Poisson's ratio of the matrix (calculated to be 0.286 by same approach as for the value of G [17]) and e^T is the relative lattice misfit (6% according to [30]).

The driving force for TiC-nucleation, Δg_v, is calculated by assuming a dilute solution approximation according to [9]:

$$\Delta g_v = -\frac{RT}{V_{TiC}^{mole}} \sum_i x_{TiC,i} \ln\left(\frac{x_{m,i}}{x_{m,i}^{TiC/m}}\right), \quad \textbf{Equation 5.10}$$

where V_{TiC}^{mole} is the molar volume of TiC, $x_{TiC,i}$ is the mole fraction of element i in the TiC precipitate, $x_{m,i}$ the mole fraction of element *i* in the matrix, $x_{m,i}^{TiC/m}$ the equilibrium mole fraction of element i in the matrix at the TiC/Matrix interface and R is the gas constant.

The smallest possible nucleus of TiC is assumed to consist of one unit cell of TiC. This correspond to 14 titanium atoms, when all titanium atoms on the surface are counted as whole atoms. The length of the cube-shaped nucleus is therefore:

$$l_{min} \geq \sqrt[3]{3.5} a_{TiC}, \quad \textbf{Equation 5.11}$$

where $a_{TiC} = 4.33\text{Å}$ [31] is the lattice parameter of TiC. The critical nucleus size l^* is thereafter expressed by differentiation of Eq. 5.8 with respect to l, equating to zero and solving for l:

$$l^* = \frac{-4\gamma_{eff}}{\Delta g_v + \Delta g_s}. \quad \textbf{Equation 5.12}$$

The time dependent nucleation rate of TiC precipitates, I_{TiC}, is expressed as [32]:

$$I_{TiC} = N_{v,TiC} Z \beta^* \exp\left[-\frac{\Delta G_{TiC}^*}{k_B T}\right] \exp\left[-\frac{\tau}{t}\right], \quad \textbf{Equation 5.13}$$

where, $N_{v,TiC}$ is the number density of potential nuclei sites for TiC, Z is the Zeldovich factor, β^* is the frequency of atomic attachment to the growing precipitate and τ is the incubation time.

The number density of possible nucleation sites is as assumed to be all substitutional atomic sites within the capture radius of the dislocation:

$$N_{v,TiC} = \pi r_c^2 \rho(t) N_{v,0}. \quad \textbf{Equation 5.14}$$

We use the same $\rho(t)$ as modelled according to Eq. 5.5-5.6. $N_{v,0}$ is the number density of substitutional atomic sites and r_c is the capture radius of each dislocation. The capture radius of the dislocations is calculated according to [33]:

$$r_c = e^{0.577} \frac{A}{4kT} \quad \text{with} \quad A = \frac{\mu b}{3\pi} \frac{(1+v)}{(1-v)} \Delta \mathbb{v}, \qquad \textbf{Equation 5.15}$$

where $\Delta \mathbb{v}$ is the volume difference between matrix and solute atoms [33]. We calculate the volume difference between matrix and solute atoms by comparing the volume of one single Fe atom in a BCC unit cell of iron with the volume of one single Ti atom in a BCC unit cell of Ti using the lattice parameters as reported by [34]. The capture radius as calculated from Eq. 5.15 is 8.7 Å at 550 °C.

The Zeldovich factor is described according to [9]:

$$Z = \frac{\sqrt{2}}{\sqrt{3}} \frac{V_{TiC}^{atom} \sqrt{\gamma_{eff}}}{\sqrt{k_B T}} \left(\frac{1}{l^*}\right)^2, \qquad \textbf{Equation 5.16}$$

where V_{TiC}^{atom} is the atomic volume of TiC. The frequency of atomic attachment to the growing sub-critical nucleus is expressed as [9]:

$$\beta^* = \frac{6(l^*)^2}{a_{TiC}^2} \lambda_{TiC}^m, \qquad \textbf{Equation 5.17}$$

where λ_{TiC}^m is the effective attachment frequency of a TiC molecule, modelled as in [9]. The incubation time τ_p is given by

$$\tau_p = \frac{1}{2Z^2\beta^*}. \qquad \textbf{Equipment 5.18}$$

5.3.2 Growth of TiC

The shape of the critical nucleus is converted from a cubical to a spherical nucleus, while keeping the precipitate volume and the total Gibbs free energy constant. This leads to a critical nucleus radius r^* and an effective spherical interface energy γ_r with equations:

$$r^* = \sqrt[3]{\frac{3}{4\pi}} l^* \quad \text{and} \quad \gamma_r = \sqrt[3]{6/\pi}\, \gamma_{eff}\ . \qquad \textbf{Equation 5.19}$$

The growth of all precipitates is thereafter modelled using a Zener approach for spherical precipitates, where the growth rate, υ_{TiC}, of each precipitate with radius *r* is expressed as [35]:

$$\upsilon_{TiC} = \frac{D_i}{r} \frac{c_{m,i} - c_{m,i}^{TiC/m,r}}{c_{TiC,i} - c_{m,i}^{TiC/m,r}}, \qquad \textbf{Equation 5.20}$$

where D_i is the effective diffusivity if element i in martensite, $c_{m,i}$ is the concentration of element i in the matrix, $c_{TiC,i}$ is the concentration of element i in the precipitate and $c_{m,i}^{TiC/m,r}$ is the concentration of element i in the matrix at the precipitate/matrix interface. All concentrations are in the units moles per m^3. The above equation must be true for each of the elements C, Ti and Mn, which leads to three equations with the four unknowns $v_{TiC}, c_{m,C}^{TiC/m,r}, c_{m,Ti}^{TiC/m,r}$ and $c_{m,Mn}^{TiC/m,r}$. The concentrations for iron are obtained by a mole balance.

The fourth equation needed to solve for the four unknowns is given by an adjusted form of the Gibbs-Thomson effect, which includes the effects of misfit strain energy:

$$\sum_{i\in\{Fe,C,Ti,Mn\}} x_{TiC,i} \ln\left(\frac{x_{m,i}^{TiC/m,r}}{x_{m,i}^{TiC/m,\infty}}\right) = \frac{V_{TiC}^{atom}\gamma_r}{k_B T}\frac{2}{r} + \frac{V_{TiC}^{atom}}{k_B T}\Delta g_s. \quad \textbf{Equation 5.21}$$

This equation can be derived similar to the procedure given in [36]. We adjust the Gibbs-Thomson effect to account for the misfit strain energy to obtain consistency between the nucleation part of the model and the growth part of the model: if the Gibbs-Thomson effect is not adjusted for the effect of the misfit strain energy, a precipitate with zero growth rate, i.e. $v_{TiC} = 0$, will have a radius unequal to r^*, which is physically incorrect.

Earlier studies have shown that the high dislocation density of martensite increases the diffusion rate in martensite [10]. The effective diffusivities of C, Ti and Mn in martensite, $\langle D_C\rangle, \langle D_{Ti}\rangle, \langle D_{Mn}\rangle$, are therefore taken as a balance between the lattice diffusivities, ${D_L}^{C/M}, {D_L}^{Ti/M}, {D_L}^{Mn/M}$, and the pipe diffusivities, ${D_p}^{C/M}, {D_p}^{Ti/M}, {D_p}^{Mn/M}$, on the format given by [37] where we remove the cross section area for pipe diffusivity from the area of lattice diffusivity:

$$\langle D_e\rangle = (1 - g(t)){D_L}^{e/M} + g_s(t){D_p}^{e/M}$$
$$\text{for } e = C, Ti, Mn. \qquad \textbf{Equation 5.22}$$

Here $g_s(t)$ is the cross sectional area of dislocation pipe per unit area of matrix. The pipe diffusivities for Ti and Mn are unknown, but under the assumption that the presence of a dislocation lowers the energy barrier for diffusion, it is reasonable to assume that the ratio between the bulk diffusivities and the pipe diffusivities of the elements C, Ti and Mn is equal to the ratio between the bulk diffusivity and pipe diffusivity of Fe:

$$\frac{{D_p}^{e/M}}{{D_L}^{e/M}} = \frac{{D_p}^{Fe/M}}{{D_L}^{Fe/M}} \qquad \text{for } e = C, Ti, M, \qquad \textbf{Equation 5.23}$$

where the ratio $\frac{D_p^{Fe/M}}{D_L^{Fe/M}}$ is found in [21].

The effective pipe radius of a dislocation is set equal to the Burgers vector, b, and the cross sectional area of dislocation per unit area of matrix is expressed as:

$$g_s(t) = \rho(t)\pi b^2. \qquad \textbf{Equation 5.24}$$

The number balance of precipitates in the model is described according to [9]

$$\frac{\partial \phi}{\partial t} = -\frac{\partial[v_{TiC}\phi]}{\partial r} + \delta\left(r - r^*_{k_BT}\right)I_{TiC}, \qquad \textbf{Equation 5.25}$$

in which $\phi \equiv \phi(r,t)$ in m^{-4} is the number density distribution of precipitates of radius r at time t and v_{TiC} in ms^{-1} represents the growth rate of precipitates of radius r at time t. The radius $r^*_{k_BT}$ is the radius for which the energy of nucleation is k_BT less than the energy for r^* ($r^*_{k_BT} > r^*$).

The key features of the model for TiC precipitation [9] are the inclusion of multi-component and multi-phase effects within the model. In [9] it has been shown that the model is capable of dealing with the multiple secondary phases which compete for the same solid solution elements. We choose a different numerical method than that from [9]. We use a combination of Strang splitting, first-order upwinding [38], Implicit and Explicit Euler time-integration and adaptive mesh techniques. The initial mesh contains 500 bins on a logarithmic scale, similar to [9]. The simulation is following the same temperature profile as applied directly after quenching during the experiments of Öhlund et al. [10].

5.4 Experimental

We have published the experimental methods and results elsewhere before [10]. The experimental results are now being used as input parameters and validation for the proposed model. Two high-purity Fe-C-Mn steels are investigated: one without Ti and one with the addition of 0.042 wt.% Ti. The compositions of the steels are given in table 5.1.

Table 5.1 *Chemical composition of the examined steels (wt.%)*

Steel	C	Mn	Si	P	S	Al	Ti	Cu	Cr	O	V
Ti-free	0,39	0,8700	0,0035	0,0010	0,0007	0,0050	-	0,0012	0,0018	0,0080	0,0023
Ti-containing	0,39	0,8700	0,0040	0,0011	0,0007	0,0047	0,0420	0,0012	0,0022	0,0046	0,0022

The Ti-free steel is austenitized at 940 ˚C for 40 min and the Ti-containing steel is homogenised and austenitized at 1350 ˚C for 30 min. The austenization temperature of 1350°C is chosen to assure that all Ti atoms are in solid solution. The different austenization times are chosen to obtain similar austenite grain sizes. Both steels are quenched to room temperature from their respective austenization temperature, using He-gas followed by tempering treatments performed at 300 ˚C and 550 °C for 5, 10, 30 and 60 min. The heating time up to the full tempering temperature is 138 seconds. The tempering temperature of 300 °C is chosen to assure that all Ti atoms remain in solid solution, as nucleation of TiC does not take place during tempering at 300°C6). The tempering level of 550 °C is chosen to assure that TiC nucleation and growth takes place during tempering, as literature report that TiC nucleation take place when tempering temperatures are in the range of 550°C [6].

Micro-Vickers hardness (HV0.5) is used to study the evolution of macroscopic hardness. Scanning electron microscopy (SEM, JEOL JSM-6500F with field emission gun) is used to study the evolution of Fe_3C-particle size volume fraction. Electron back-scatter diffraction (EBSD with a Nordlys detector) is used to study the coarsening of martensite blocks and to estimate the evolution of recovery in the martensite. We estimate the evolution of recovery from the crystallographic indexing results. Block boundaries, high surface roughness, high elastic strain and high strain levels due to e.g. dislocations reduces the band contrast of the Kikuchi patterns of the EBSD signal. If the degradation is high enough, the measurement point cannot be indexed. As no block coarsening takes place during annealing and the surface roughness and elastic strain is comparable for all specimens, we consider the improvement of the band contrast during annealing to be a result of recovery. However, since only regions close to block boundaries contain dislocation densities which are high enough to prevent indexing in the as quenched state, the results are only representative for regions adjacent to block boundaries. The indexing results for the as-quenched specimen is considered to be representative for martensite with no recovery and the indexing results for the specimens tempered for 60 min is considered to be representative for the fully recovered state. The dislocation density in the as quenched state is set to the value measured by Morito et al. [23] and the dislocation density in the fully recovered state after annealing is given by Takebayashi et al [39]. The indexing result is thereafter used to estimate the recovery evolution and the dislocation density during annealing.

Atom probe tomography (APT, Imago LEAP 3000X HR with laser pulsing) is used to measure the concentration of carbon and titanium atoms in solid solution and the TiC-precipitates in the Ti-containing martensite after 60 min of tempering at 550 °C.

5.5 Model fitting

5.5.1 Input parameters

The EBSD measurements in ref. [10] show that no grain coarsening takes place during tempering. Therefore, we take $\Delta\sigma_{gb}$ in Eq. 5.2 as a constant. The measured volume fraction of Fe_3C-particles as a function of annealing time and temperature is used as an input to the model. The SEM-measurements in ref. [10] are used to determine the Fe_3C-particle width, w, and length, l, which are used to calculate the volume fraction of Fe_3C precipitates. We calculate the volume of each Fe_3C-particle that is measured within a square area of SEM images using:

$$V = 4\pi\left(\frac{w}{2}\right)^2\left(\frac{l}{2}\right). \qquad \textbf{Equation 5.26}$$

The total volume of all particles is summarized within each sample. The volume fraction of Fe_3C-precipitates as a function of annealing time and temperature is determined, assuming a cubic measurement volume. We observe that the equilibrium volume fraction of Fe_3C-precipitates is 0.087 for the Ti-containing steel after 60 min of isothermal tempering at 550 °C. However, ThermoCalc simulations (TCFE6) for the Ti-containing steel show that the equilibrium volume fraction of Fe_3C is equal to 0.058 at 550 °C. The higher volume fraction we measure from SEM can be due to a slight overestimation of particle dimensions from SEM pictures and due to the assumption of oval particle shape (Eq. (26)).
We now use the APT measurements to estimate the volume fraction of Fe_3C in the Ti-containing steel after 60 min of tempering at 550 °C. The APT measurement show that the concentration of carbon atoms in solid solution is $35 \cdot 10^{-3}$ at% C. This is higher than the simulated equilibrium concentration of C atoms in solid solution in ferrite at 550 °C ($1.8 \cdot 10^{-3}$at% according to ThermoCalc). From the APT results we can also estimate the fraction of carbon atoms that is used for the formation of TiC-precipitates. We assume that carbon is distributed between TiC, Fe_3C and C in solid solution and derive that the volume fraction of Fe_3C is 0.057 (98% of the equilibrium volume fraction) after 60 min of isothermal tempering at 550 °C.
We therefore create a scale factor from the relationship we find between the SEM and APT volume fractions for the Ti-containing steel after 60 minutes of tempering at 550°C. The volume fraction of Fe_3C, as determined by SEM, is thereafter scaled for each examined specimen. The effective radius of the Fe_3C-particles is also used as an input parameter to the model. The effective radius of the Fe_3C-particles in each specimen is calculated from the scaled SEM volume fraction of Fe_3C by assuming spherical particles.

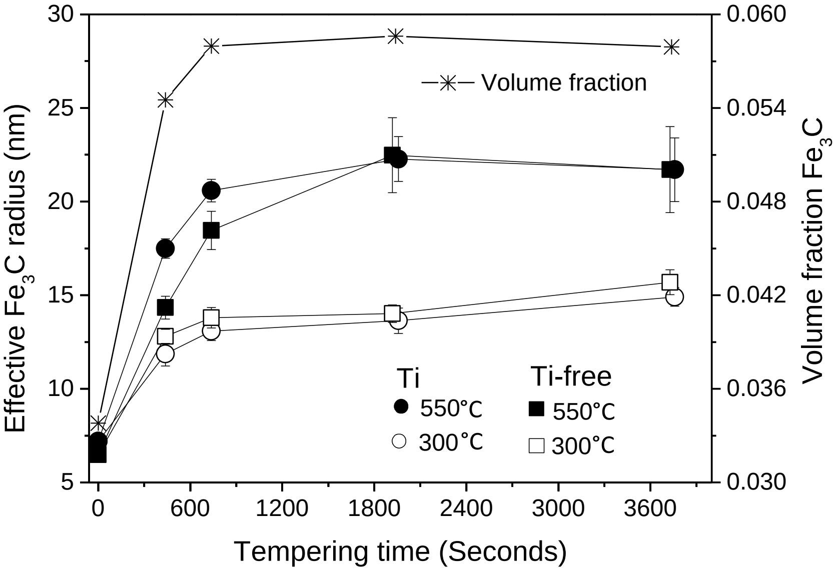

Figure 5.1 *Effective Fe_3C radius [nm] of Ti-free and Ti-containing martensite during annealing at 300°C and 550°C as a function of annealing time and the volume fraction of Fe_3C in the Ti-containing steel after annealing at 550°C. Error bars represent 95% confidence interval.*

Fig. 5.1 shows the effective Fe_3C radius and volume fraction of Fe_3C, as a function of tempering time, that are used as input parameters in the model. The four curves for volume fraction of Fe_3C are overlapping, and we therefore show only the Ti-containing steel at 550 °C. Both the effective precipitate size and the volume fraction of Fe_3C grow rapidly during the first 5 min of isothermal tempering. After 5 min of isothermal tempering the growth continues at a lower rate, and after 10 min the values stabilises. We note that the spread in cementite particle size increases with tempering time, during tempering at 550 °C, which is reflected by the increase in the size of error bar for the average cementite particle size.

The small carbides which are observed in the as-quenched state could correspond to ε-carbides, based on their size and that they are present directly after quenching. In the present model, all the iron-carbides are modelled as Fe_3C-particles. The volume fraction of Fe_3C is used to calculate the input parameter of carbon concentration in solid solution to the model, as only one data point for the carbon concentration in solid-solution was measured by APT (at 60 min of isothermal tempering at 550 °C for the Ti-containing steel).

5.5.2 Fitting approach

The parameters $\sigma_{gb}, K_{Mn}, K_{Ti}, \alpha$ and V_a of the hardness model are currently unknown. Two of these parameters, α and V_a, are also used within the KWN TiC precipitation model, together with the misfit strain energy Δg_s for the TiC precipitates. We will use the following approach to obtain estimates of these parameters:

1. $\sigma_{gb}, K_C, K_{Mn}, K_{Ti}, \alpha$ and V_a are fitted using least-squares techniques by minimising the residual between the simulated hardness given by Eqs. 5.1 and 5.7 of the model and the measured hardness from experiments. We simultaneously fit the model to the experimental data from the Ti containing steel at 300 °C and the Ti free steel at 300 °C and 550 °C at 0, 5, 10, 30 and 60 min of tempering. The Ti-containing steel heat-treated at 550 °C is excluded from the fitting of the above parameters in order to avoid the influence of TiC precipitates.
2. Δg_s is obtained by using a least-squares techniques by minimising again the residual between the predicted hardness and the measured hardness, where the values for the parameters $\sigma_{gb}, K_{Mn}, K_{Ti}, \alpha$ and V_a from the previous step are used within the hardness model and the TiC precipitation model. Only the data for the Ti-containing steel during tempering at 550 °C after 0, 5, 10, 30 and 60 min is used to obtain the value of Δg_s.

5.6 Results and discussion

5.6.1 Fitting parameters

Fig. 5.2 shows the measured hardness (symbols) and the fitted (lines) hardness as a function of annealing time of (a) the Ti-free steel at 300°C and 550°C and the Ti-containing steel at 300°C and (b) the Ti-containing steel at 550°C.

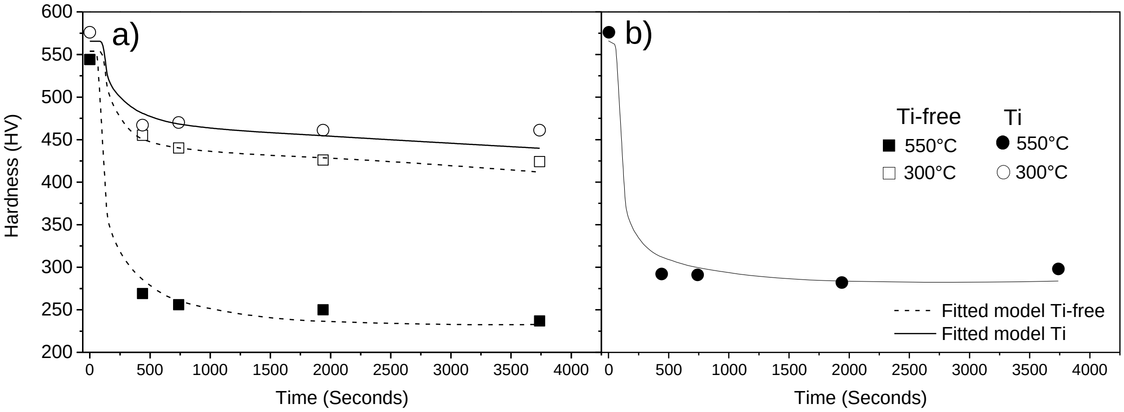

Figure 5.2 *The measured hardness (symbols) and the fitted model (lines) of a) the Ti-free steel at 300°C and 550°C and the Ti-containing steel at 300°C as a function of annealing time and b) the Ti containing steel at 550°C. 95% confidence intervals are covered by the symbols. The error bars (representing 95% confidence intervals) are smaller than the symbols size.*

The comparison between the experiment and the model in Fig. 5.2(a) is used obtain values for the fitting parameters $\sigma_{gb}, K_{Mn}, K_{Ti}, \alpha$ and V_a. The comparison between the experiment and the model in Fig. 2(b) is used to fit a value for the strain energy. From Fig. 5.2(a) & (b). it can be seen that the fitted model correctly describes the evolution of the hardness during tempering. The fitted parameters $\sigma_{gb}, K_{Mn}, K_{Ti}, \alpha, V_a$, and Δg_s are given in Table 5.2.

Parameter	Value
σ_{gb} (MPa)	340
K_C (MPa(wt%)$^{-1/2}$)	0
K_{Mn} (MPa(wt%)$^{-1}$)	0
K_{Ti} (MPa(wt%)$^{-1}$)	1679
α	0.401
V_a (m^3)	$16.99b^3$
Δg_s (GJ/m^3)	1.34

Table 5.2 *Results from least-squares fitting of Eqs. 5.7-5.8 to the measured hardness.*

In the following section we compare the values of the fitted parameters to the values reported in literature. The σ_{gb} of our model is the combination of lattice friction and the hardness contribution of the martensite block structure (grain size hardening). The model predicts $\Delta\sigma_{gb} = 340\ MPa\ (113\ HV)$. This calculated value is lower than the value of 413 MPa which is given in literature [2]. This difference can be due to the difference in grain size that we use and the grain size that is used in literature. The literature value of 413 MPa is based on the grain size the average lath width of 0.25 µm. This is smaller than the effective grain size (determined by the block boundaries) that we used in our model. The value that we find for $\alpha = 0.401$ is in good agreement with the literature reports ranging from 0.24 to 1 [18, 40]. We note that the experimental work of [10] shows that the concentration of carbon atoms in true solid solution (between laths) and the concentration of carbon atoms segregated to lath boundaries (high dislocation density) are 0.005 wt% and 0.045 wt% respectively, after 60 min of tempering at 550°C. This indicates that the majority of carbon atoms in the martensite have segregated to dislocations and that Eq. 5.3 therefore cover the major influence of carbon atoms in solid solution on the martensite strength. The activation volume of the recovery process in martensite, V_a, is compared to the literature value for the activation volume of the recovery process in BCC iron. Our model predicts a value of 17b^3 or 0.26 nm^3, which is in good agreement with the reported value of 0.1 to 0.6 nm [3, 41]. The fitted values of the K_{Mn}-parameter is zero, whereas literature reports a value of K_{Mn} = 35 MPa(wt%)$^{-1}$ [13].

The difference between our fitted value of K_{Mn}=0 and the literature value of K_{Mn}=35 MPa(wt%)$^{-1}$, falls within the uncertainties of our experiments and the uncertainties of the experiments reported in literature. We estimate that Mn in solid solution contributes with maximum 10 HV to the total hardness in our system. Here we assume that the Mn-atoms do not have time to redistribute during the formation of cementite so that the overall manganese concentration in the matrix corresponds to the overall concentration of 0.87 wt% Mn in the steel. The strengthening effect of Mn in solid solution in the as-quenched martensite is therefore approx. 30 MPa (or 10 HV), in case we use the literature value for K_{Mn} =35 MPa(wt%)$^{-1}$ and Eq. 9.3. In case the Mn-atoms would redistribute into cementite, the Mn-concentration in the matrix would be even lower and subsequently the added strength. The error in our hardness measurements is approx. ±5 HV. The steels used by [13] contain sulphur, which may form MnS precipitates. The formation of MnS can influence the hardness by precipitate strengthening and the literature value of 35 MPa(wt%)$^{-1}$ for K_{Mn} may therefore be biased.

There are not many reports in the literature about the strain energy if TiC-precipitates in martensite. Jang et al [30] have used first principles calculations to estimate a value of 4.10kJ/mol or 1.16 GJ/m^3. This value corresponds well to our fitted value of 1.34 GJ/m^3 or 4.74 kJ/mol.

5.6.2 TiC-precipitates and recovery

Fig. 5.3 shows the calculated TiC precipitate size distribution together with the TiC precipitate sizes measured by Öhlund et al.[10]. The precipitate size as measured by APT is based on the APT atom count for each precipitate[2].

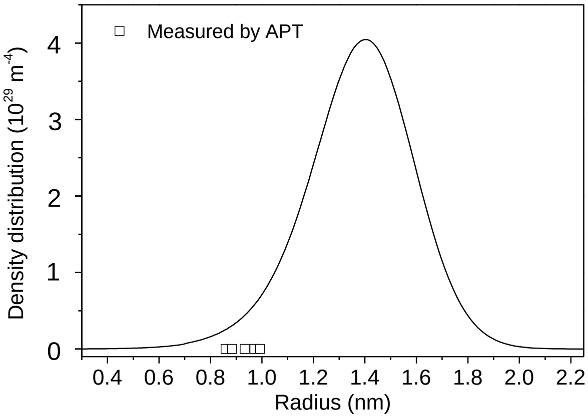

Figure 5.3 *The simulated TiC precipitate size distribution (line) and the experimental precipitate sizes (symbols) as measured by APT in the Ti-containing martensite after 60 minutes of tempering at 550°C.*

---

[2] We convert the atom count to a radius, assuming spherical precipitates, by the volume estimated from the lattice parameter of TiC. We add the distance of one Ti atom radius to the calculated radius as the volume estimated by the lattice parameters only measure to the centre of the outer atoms.

The KWN model predicts that 0.27 % of the equilibrium volume fraction of TiC forms and that the average TiC precipitate radius is 1.38 nm after 60 min of isothermal tempering at 550 °C. Furthermore, the model predicts that nucleation of TiC precipitates starts during the heating stage, 10 seconds before reaching the isothermal temperature of 550 °C and that the peak in number density of TiC-precipitates is reached after 385 seconds of heating and tempering (after 4 min and 7 seconds of isothermal tempering). The predicted average radius and size distribution from the KWN model are slightly higher than the values measured by APT. However, the measured precipitates sizes fall within the nonzero part of the predicted distribution and is therefore in agreement with the model. The predicted volume fraction of formed TiC-precipitates is lower than what is measured by APT. This could be due to the small sample size inherent to APT.

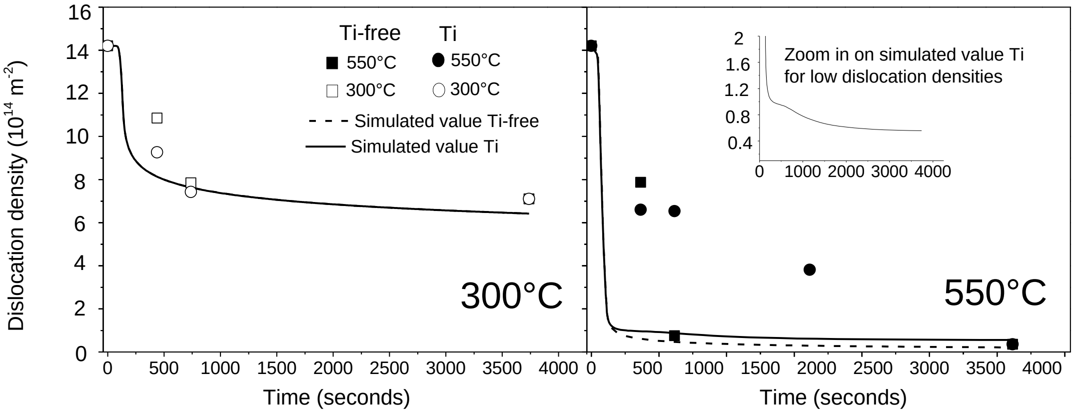

Figure 5.4 *The measured (symbols) and the simulated (lines) dislocation density in Ti-free and Ti-containing steel as a function of annealing time during annealing at 300°C and 550°C. The simulated value of Ti-containing and Ti-free steel overlap at 300°C.*

Fig. 5.4 shows the dislocation density as a function of tempering time for Ti-free (precipitate free) and Ti-containing steel at different temperatures, as simulated via Eqs. 5.5-5.6 and as measured by EBSD experiments [10].

We use the simulated dislocation density as input to our model. The simulation of the evolution of the dislocation density does not take into consideration the pinning of dislocations by small iron carbides and cementite particles. We observe that these type of particles are present in the steels after quenching and at all annealing times. The pinning of dislocations by iron carbides is therefore expected to be approximately constant throughout the annealing of the steels and our simulation might overestimate the amount of recovery which has occurred at times between 5 to 60 minutes of isothermal tempering.

Fig. 5.4(a) shows the dislocation density of Ti-free and Ti-containing martensite during tempering at 300 °C (where no TiC precipitates are present). We observe that the evolution of the recovery is slightly faster in the simulated values than in the experimental values and that the simulation results in a higher degree of recovery. Figure 4b shows the dislocation density of Ti-free and Ti-containing martensite during tempering at 550 °C. We observe that the simulated and the experimental values do not correlate. The simulation of recovery in the Ti-containing steel shows faster recovery and a much higher degree of recovery than the experimental values. However, we observe a recovery delay in the simulated values, with a maximum delay effect between 200 and 550 seconds of tempering. We note that the recovery delay of the simulated dislocation density and the recovery delay observed by experiments show a similar evolution in time (see the zoomed in panel). The recovery delay of the simulations of the Ti-containing steel at 550°C results in a slightly higher dislocation density in the Ti-containing steel than in the Ti-free steel during isothermal annealing at 550 °C.

The recovery delay of the simulated dislocation density is a result of the high number of TiC-precipitates which are present at that time. The KWN model predicts that the highest number of TiC precipitates, which can act as pinning points for dislocations, appears after 385 seconds of tempering. The large disagreement between simulated and experimentally estimated values at 550°C is a result of that the experimentally established recovery is representative for regions close to block boundaries. Nucleation of TiC is faster in the regions close to block boundaries, which reduces the rate of recovery in these regions [10]. The experimentally estimated dislocation density therefore becomes too high.

5.6.3 Evolution of multiple hardening components during tempering

Fig 5.5 shows the evolution of the hardness contribution from different microstructural components of the martensite as a function of time during tempering at 550 °C.

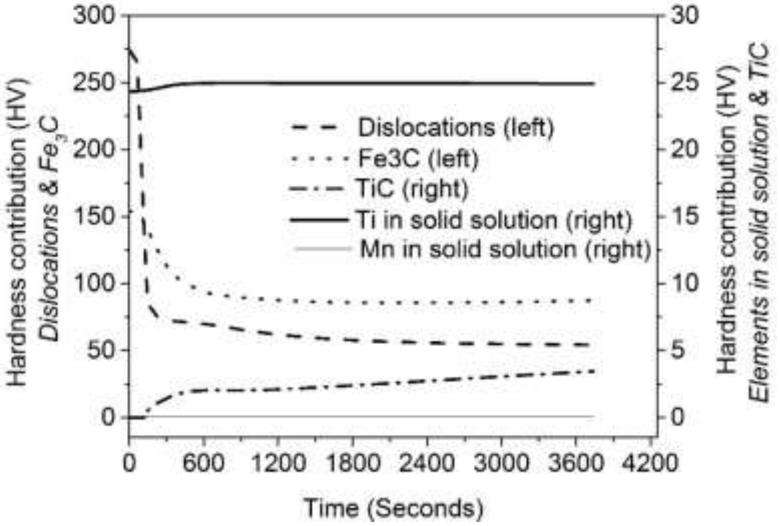

Figure 5.5 *The evolution of the contribution of multiple hardness components to the overall hardness of martensite as a function of time during tempering at 550°C.*

The microstructural components which give the largest direct contributions to the overall hardness of martensite during tempering are 1) Fe_3C precipitates and 2) dislocations.

The strengthening effect of Fe_3C precipitates is decreasing by 50 HV during heating to 550°C and the first 8 min of isothermal tempering at 550°C. This rapid decrease takes place due to the fast coarsening of Fe_3C particles during the same time period, as presented in Fig 5.1. After 8 min of isothermal tempering the strengthening effect stabilises and our hardness model predicts that the hardness contribution of Fe_3C is approx. 88 HV, which remains stable from 8 to 60 min of isothermal annealing at 550 °C. The high hardness contribution of Fe_3C by precipitation strengthening is supported by the literature: ε-carbides that form during low temperature annealing or during auto-tempering, have been measured to significantly increase the hardness of lath martensite [42]. Small iron-carbides can therefore be a very effective way of increasing the strength and hardness of martensite. However, the strengthening effect of iron carbides could be sensitive to long time service at elevated temperatures due to rapid diffusion of carbon atoms, which could enable cementite coarsening via Ostwald ripening. As coarsening proceeds, the spread in particle size will increase (but the average size might remain constant). At a certain critical point, all small precipitates are consumed and the average precipitate size increases, while the number density decreases. This change in precipitate size and number of precipitates will lead to a reduction in the precipitation strengthening effect of Fe_3C. The experimental results show that the spread in cementite particle size increases with annealing time (see Fig. 5.1). The strengthening effect of dislocations decreases very rapidly by approx. 200 HV during the 138 seconds of heating to the isothermal annealing temperature. This rapid decrease is a result of the rapid recovery which is shown in Fig 5.4(b). The strengthening effect of dislocations stabilises during tempering. Our hardness model predicts that the hardness contribution of dislocations is approximately stable at 54 HV from 10 to 60 minutes of isothermal tempering at 550 °C.

The microstructural components which give minor direct contributions to the overall hardness of martensite are 1) Ti atoms in solid solution and 2) TiC, as shown in Fig. 5.5. The strengthening due to Ti in solid solution increases slightly during heating up and the first minutes of isothermal tempering at 550°C and is thereafter stable. The hardness increases slightly due to a slight increase in the concentration of Ti atoms in the matrix as a result of formation of Fe_3C which redistributes a high number of Fe and C atoms from the matrix to Fe_3C. ThermoCalc simulations show that Ti does not dissolve in Fe_3C and is therefore remaining in the matrix. Our hardness model predict that the hardness contribution due to Ti in solid solution is approx. 25 HV after 60 min of isothermal tempering at 550 °C. The strengthening effect of TiC precipitates is zero during the majority of the heating up of the steel, and is thereafter increasing rapidly during the first 7 min of isothermal tempering at 550 °C. After 8 min of isothermal tempering the hardness increases slowly. The hardness model predicts that the strengthening effect due to precipitation strengthening of TiC is approximately 3.5 HV after 60 min of isothermal tempering at 550 °C. We note that the theoretical maximum precipitation strengthening effect of TiC is 42 HV. The direct strengthening effect of Mn atoms in solid solution is zero during the entire process of tempering, as shown in Fig. 5.5.

The microstructural components which give combined contributions to the overall hardness of martensite are TiC precipitates combined with dislocations.

Our model predicts that the recovery process in the Ti containing steel is delayed during isothermal tempering at 550 °C as a result of TiC precipitates which pin dislocations (see Fig. 5.4(b)). The resulting dislocation density of the Ti containing steel is therefore higher than the dislocation density of the Ti-free steel. This higher dislocation density contributes to a 20 HV higher hardness contribution in the Ti-containing steel after 60 min of isothermal tempering at 550 °C, as compared to the Ti-free steel. The total strength contribution due to formation of TiC in martensite is therefore the sum of the TiC precipitation strengthening effect, and the extra dislocation strengthening effect due to less recovery. Our hardness model predicts that this combined strengthening effect is 23.5 HV after 60 min of isothermal tempering at 550 °C. The low strengthening effect of TiC-precipitates is a result of the low volume fraction of TiC-precipitates that is predicted by our model. We note that when the model is run for longer holding times at 550 °C, there is only a slight increase in the volume fraction of formed TiC-precipitates. The resulting hardness increase is small: 5.9 HV after three hours of isothermal annealing at 550 °C. An extended heat-treatment time will therefore not improve the properties of the martensite by much. The low volume fraction of TiC-precipitates is related to the large misfit strain (1.34 GJ/m^3) that we find during fitting and the low density of potential nucleation sites (Eq. (14)) that we use as input parameter to the model. Both factors reduce the nucleation rate. The low density of potential nucleation sites is a result of the rapid recovery of the simulated dislocation density which is used as an input to our model, and the calculated capture radius.

We investigate the influence of a higher number of available nucleation sites by repeating the fitting of our model to the measured hardness at 550°C, using 1) an increased capture radius of $2 \cdot r_c$, as calculated by Eq. 5.15 and 2) a higher dislocation density of the martensite. To increase the dislocation density we use the experimental dislocation density as input to the model, instead of simulating the dislocation density according to Eqs. 5.5-5.6 within the model.

We investigate the effect of lower mis-fit strain by setting a fixed value of the mis-fit strain (75% of the value predicted by our fit to the measured hardness) as input parameter to the model. We investigate the effect of a lower mis-fit strain energy combined with a higher number of available nucleation sites, by setting the mis-fit strain energy to 1.3359 GJ/m^3 and using the experimental dislocation density as input parameters to the KWN model. The results from the repeated fit of our model and the accuracy of the simulated values to the measured hardness (given as the sum of squared errors) are given in table 5.3, together with the values from our original fitting.

Table 5.3 *Results from least-squares fitting of model after 60 minutes of tempering at 550°C, using modified input parameters*

Modified input parameter	$\boldsymbol{f_{TiC}}$	**Accuracy of model**	$\Delta \boldsymbol{g_s}$
Original model (no modification)	0.27%	793	1.3359 GJ/m^3
Capture radius $\mathbf{2 \cdot r_c}$	0.28%	788	1.3347 GJ/m^3
Higher Dislocation density (experimental)	0%	41638	2.3189 GJ/m^3
$\Delta \boldsymbol{g_s}$=1.0019 GJ/m^3	17%	973	
Higher dislocation density & $\Delta \boldsymbol{g_s}$=1.3359 GJ/m^3	44.9%	1.336x10^9	

An increased capture radius does not generate a higher volume fraction of TiC-precipitates, but it slightly improves the accuracy of the fitting of the model. Increasing the dislocation density alone results in a considerably higher value for the misfit strain energy after fitting, which does not correspond anymore to first-principles calculations[30]. Moreover, in this case the model predicts that no nucleation of TiC-precipitates takes place. A reduction of the misfit strain energy results in a higher volume fraction of formed

TiC, and a slight reduction of the accuracy of the fit. A reduction of the mis-fit strain energy and a higher dislocation density results in a significantly increased volume fraction of TiC-precipitates and a smaller precipitate size. The latter results are more in agreement with the APT measurement. However, the model is no longer capable of fitting to the measured hardness.

5.7 Conclusions

We quantify the evolution of the multiple hardness contributions to the overall hardness of martensite containing TiC-precipitates during isothermal annealing. We simulate the hardness of martensite as a linear addition of multiple hardening mechanisms. This hardness model is combined with a microstructural model based on the Kampmann-Wagner-Numerical (KWN) approach for a multi-component and multi-phase system to simulate the nucleation and growth of TiC-precipitates.

The two microstructural components which contribute most to the overall hardness of the investigated Fe-C-Mn-Ti steel are Fe_3C precipitates (88 HV) and dislocations (54 HV). Both contributions decrease rapidly during initial stages of annealing and stabilise after 10 minutes of annealing. The addition of titanium to the steel gives a minor hardness contribution via Ti-atoms in solid solution and TiC precipitates. Ti atoms in solid solution give a hardness contribution which increases slightly during the first minutes of annealing and thereafter remains stable (at 25 HV). The direct contribution of TiC precipitates to the overall hardness is limited (3.5 HV). However, TiC-precipitates also contribute to the overall hardness by pinning of dislocations during the recovery that takes place during the tempering. The model predicts that only a small volume fraction of TiC-precipitates forms during isothermal annealing at 550 °C due to the large misfit strain (1.34 GJ/m^3) and the low density of potential nucleation sites.

5.8 References

[1] ISO898-1, Mechanical properties of fasteners made of carbon steel and alloy steel-Part 1. Fifth edition, Switzerland, 2013
[2] G. Krauss: Mater Sci Eng A., 273-275(1999), 40
[3] S. Morito, X. Huang, T. Furuhara, T. Maki and N. Hansen: Acta. Mater., 54(2006), 5323
[4] T. N. Baker: Mater Sci. Technol: 25(2009), 1083
[5] Y. Namimura, N. Ibaraki, W. Urushihara and T. Nakayama: Wire J. Int., 36(2003), 62
[6] F.G. Wei, T. Hara, T. Tsuchida and K. Tsuzaki: ISIJ Int., 43(2003), 539
[7] F. Abe, M. Taneike and K. Sawada: Int. J. Press. Vessel Pip., 87(2007), 3
[8] M. Taneike, M. Fujitsuna and F. Abe: Mater. Sci. Technol., 20(2004), 1455
[9] D. den Ouden, L. Zhao, C. Vuik, J. Sietsma and F. J. Vermolen: Comp. Mater. Sci., 79(2013), 933
[10] C. E. I. C. Ohlund, J. Weidow, M. Thuvander and S. E. Offerman, ISIJ Int., 54(2014), 2890-2899
[11] L. H. Friedman and D. C. Chrzan: Phys. Rev. Lett., 81(1998), 2715.
[12] T. Ohmura, K. Tsuzaki and S. Matsuoka: Scripta Mater., 45(2001), 889.
[13] L. A. Nordstrom: Scand. J. Metall., 5(1976), 159.
[14] Martensite, ed. By G. B. Olsen and W. S. Owen, ASM International Materials Park, Ohio, (1992)
[15] M. Kehoe and P. M. Kelley: Scripta Metall, 4(1970), 473
[16] T. Gladman: The physical metallurgy of microalloyed steels, The University press, London, UK, (1997)
[17] G. R. Speich, A. J. Schwoeble and W. C. Leslie: Metall. Trans., 3(1972), 2031
[18] Y. Han, J. Shi, L. Xu, W. Q. Cao and H. Dong: Mater. Sci. Eng. A., A530(2011), 643
[19] H. S. Zurob, C. R. Hutchinson, Y. Brechet and G. Purdy: Acta Mater., 50(2002), 3075
[20] J. M. Rosenberg and H. R. Piehler: Metall. Trans., 2(1971), 257
[21] Y. Shima, Y. Ishikawa, H. Nitta, Y. Yamazaki, K. Mimura, M. Isshiki and Y. Iijima: Mater. Trans., 43(2002), 173
[22] L. Cheng, C. M. Brakman, B. M. Korevaar and E.J. Mittemeijer: Metall. Trans. A., 19(1988), 2415
[23] S. Morito, J. Nishikawa and T. Maki: ISIJ Int., 43(2003), 1475
[24] B. Huthcinson, J. Hagstrom, O. Karlsson, D. Lindell, M. Tornberg, F. Lindberg and M. Thuvander: Acta Mater., 59(2011), 5845
[25] Z. Wang, X. Mao, Z. Yang, X. Sun, Q. Yong, Z. Li and Y. Weng: Mater. Sci. Eng. A., A529(2011), 459
[26] M. Sawahata, M. Enomoto, K. Okuda and T. Yamashita: Tetsu-to-Hagane., 94(2008), 21
[27] S. Q. Xiao and P. Haasen: Scripta Metall., 23(1989), 365
[28] S. Y. Hu and L. Q. Chen: Acta Mater., 49(2001), 463
[29] H.I. Aaronsons, M. Enomoto and JK. Lee: Mechanisms of diffusion phase transformations in metals and alloys, CRC Press, Boca Raton, (2010)

[30] J. H. Jang, C. H. Lee, Y. U. Heo and D. W. Suh: Acta Mater., 60(2012), 208
[31] A. Teresiak and H. Kubsch: NanoStructured Mater., 6(1995), 671
[32] J. W. Cahn: Acta Metall., 4(1956), 449
[33] Z. M. Wang and G. J. Shiflet: Metall. Mater. Trans. A., 29A(1998), 2073
[34] D. S. Rickerby: Metall Science., 16(1982), 495
[35] C. Zener: J. Applied Phys., 20(1949), 950
[36] M. Perez: Scripta Mater., 52(2005), 709
[37] D. A. Porter and K. E. Easterling: Phase transformations in metals and alloys, Van Norstrand Reinhold, New York, USA, (1981)
[38] R. LeVeque: Finite Volume Methods for Hyperbolic Problems, Camebridge Univeristy Press, New York, (2002)
[39] S. Takebayashi, T. Kunieda, N. Yoshinaga, K. Ushioda and S. Ogata: ISIJ Int., 50(2010), 875
[40] R. Lagneborg and B. Bergman: Metal. Sci., January(1976), 20
[41] A. Smith, H. Luo, D. Hanlon, J. Sietsma and S. Van der Zwaag: ISIJ Int., 44(2004), 1188
[42] R. N. Caron and G. Krauss: Metall. Trans., 3(1972), 2381.

6 A comparison between ultra-high-strength and conventional high-strength fastener steels: mechanical properties at elevated temperature and microstructural mechanisms

C.Emmy I.C. Ohlund, Mladena Lucovic, Jonathan Weidow, Mattias Thuvander and S.Erik Offerman

To be Submitted

Abstract

The ongoing trend of engine down-sizing has resulted in the need for stronger automotive fasteners at more elevated temperatures. A comparison is made between the mechanical properties of the ultrahigh-strength steel KNDS4 of fastener grade 14.9 and of conventional, high-strength steels 34Cr4 of fastener grade 12.9 and 33B2 of grade 10.9. The results show that the ratio of the yield strength at elevated temperatures to the yield strength at room temperatures is much higher for the ultra-high-strength steel than for both conventional high-strength steels, especially at 500°C. Moreover, the results show a trend in which the nano-indentation creep rate is lower as the strength of the steels is higher. The better mechanical properties of the KNDS4 steel are related to the smaller size of the alloy carbides in the KNDS4 steel. In order to further improve the properties of the steel, we investigated the effect of an alternative (industrial) heat-treatment on the evolution of the microstructure and hardness of the KNDS4 steel. Changing the industrial heat treatment can increase the hardness of KNDS4 by 8%, since more alloy carbides can nucleate and grow. However, the standard industrial heat treatment results in a smaller martensite block size, which might be more beneficial for the toughness of the steel. Independent of the heat treatment, we find that the mechanical performance of KNDS4 fasteners at elevated temperature and the low nano-indentation creep rates are two strong indicators that fasteners made from KNDS4 steel might be used at higher service temperatures than traditional high strength fasteners.

6.1 Introduction

The trend of engine down-sizing has led to smaller engines with higher mechanical and thermal loading of the components inside the engine. High strength engine fasteners must therefore be able to maintain a high yield strength at elevated temperatures and to withstand creep at elevated temperatures. Martensitic low and medium carbon steels, alloyed with mainly Mn and B or Mn and Cr, are the work-horse materials for current high strength engine fasteners [1]. These fasteners have a tensile strength up to maximum tensile strength of 1200 MPa and yield strength of 0.9 times the tensile strength (grade 12.9), according to international fastener standards [2]. Higher strength fasteners are not yet listed in the fastener standards, because the susceptibility to hydrogen embrittlement increases in traditional fastener steels in case the strength exceeds 1200 MPa [3]. The fastener standards furthermore list a recommended service temperature of maximum 150°C [2]. The reason behind the latter restriction is related to the fact that the traditional fastener steels can lose strength and/or experience creep at elevated temperatures.

New fastener steels have already been developed, based on the need for higher strength and improved resistance to hydrogen embrittlement [4]. The improvement in strength at room temperature of these fastener steels is achieved by a tempered martensite matrix and the addition of carbide-forming elements such as titanium (Ti), vanadium (V) and molybdenum (Mo) [5-11]. The potential improvements of the mechanical properties of fastener steel at elevated temperatures due to the formation of alloy carbides was not taken into account during the development of novel ultra-high-strength steels for fasteners. However, literature shows that the creep properties of martensitic steel are improved by the presence of alloy carbides [12-14]. Moreover, a report demonstrates the combined improvement of the room temperature and high temperature tensile strengths of martensite due to a fine dispersion of alloy carbides [15]. Creep measurements are very time consuming. In this study we aim to obtain more insight into the mechanical properties of ultra-high-strength steels for fasteners at elevated temperatures without performing time-consuming creep measurements by applying a nano-indentation technique.

The aim of the present study is 1) to compare the mechanical properties of the ultrahigh-strength steel KNDS4 of fastener grade 14.9 and of conventional high-strength steels 34Cr4 of fastener grade 12.9 and 33B2 of grade 10.9 at room temperature and at elevated temperatures, 2) to characterize the alloy carbides in the steels in order to investigate the underlying microstructural mechanisms that give rise to the different properties of the three fastener steels and 3) to optimize the thermal processing of the ultra-high-strength KNDS4 steel for fasteners. KNDS4 contains the strong carbide-forming elements V, Ti and

Mo. These elements form complex alloy carbides during heat treatment and we therefore expect that KNDS4 can have better mechanical properties at elevated temperatures than conventional high-strength steels for fasteners.

6.2 Experimental

The following three experiments are carried out: 1) mechanical testing of fasteners made of KNDS4, 34Cr4 and 33B2 steel to compare room temperature and elevated temperature mechanical properties, 2) characterization of the alloy carbides to investigate the underlying microstructural mechanisms that give rise to the different properties of the three fastener steels and 3) optimizing the thermal processing of KNDS4 in order to further improve the mechanical properties of the steel. The chemical composition of the investigated steels are shown in table 6.1. The Fe-C-Mn-Ti steel was examined in an earlier investigation [16-17] and is now used as a reference during the microstructure study of KNDS4 steel for the optimization of the thermal processing of KNDS4 steel**.**

Table 6.1, *Main elements of the examined steels [wt%]*

Steel	C	Mn	Si	P	S	Al	Cr	Mo	Ni	Ti	V	B
KNDS4	0.39	0.45	0.05	0.004	0.006	0.033	1.07	1.09	0.60	0.042	0.085	-
34Cr4	0.36	0.85	0.10	0.006	0.007	0.036	1.09	0.050	0.05	0.001	0.003	-
33B2	0.32	0.72	0.09	0.010	0.010	0.031	0.23	0.008	0.04	0.051	0.004	0.002
Fe-C-Mn-Ti	0.39	0.87	0.004	0.001	0.001	0.005	0.00	-	-	0.042	0.002	-

6.2.1 Mechanical testing of KNDS4, 34Cr4 and 33B2 fasteners

We compare the performance of the different fastener steels at elevated temperature by measuring the yield strength as a function of temperature and by the nano-indentation creep rate of the three steels. Due to the time consuming measurement of creep parameters during traditional creep testing we choose to estimate the relative creep behaviour of the three steels by comparing the tendency of the steels to deform in constant-load nano-indentation experiments. We perform these experiments at room temperature, based on literature reports that a large number of metallic materials exhibit indentation creep at temperatures down to room temperature [18].

We prepare the test specimens from traditionally cold-formed M14 fasteners made from KNDS4, 33B2 and 34Cr4 steel. The fasteners are industrially heat treated in continuous belt furnaces with oil quenching. The heat treatment parameters of the three steels are given in Table 6.2.

Table 6.2, *Heat treatment parameters of industrial steels*

Steel	Austenitization	Tempering
33B2	890°C, 45 minutes	460°C, 50-55 minutes
34Cr4	890°C, 45 minutes	460°C, 50-55 minutes
KNDS4	930°C, 60 minutes	560°C, 90 minutes

The temperature accuracy of the furnace is ±5°C. The total time that the steel is in the furnace includes heating of the steel. The heating time is between 20-30 minutes for both austenitization and tempering. The longer heat treatment times for industrial heat treatment of KNDS4 are a recommendation from the steel producer. A separate batch of specimens received an additional heat treatment for 100 hours at 200°C, 300°C, 400°C or 500°C. These are the same temperatures as the temperatures at which the mechanical properties are tested.

We perform tensile tests on bar-shaped specimens with diameter 12 mm and length 135 mm that are machined from heat treated fasteners. The specimens have a reduced diameter 4.00±0.02 mm over a length of 22±2 mm in the middle of the specimen. The radius of curvature of the transition region from the reduced to the full diameter is 30 mm. Tensile testing is performed at room temperature and at elevated temperatures, using a table top MTS 858 system (25 kN) equipped with model 793.00 system software in combination with Multiple Purpose Testware operated in displacement mode. Heating is performed using an induction coil surrounding the test specimen and an ultra-high frequency induction generator TruHeat HF 3005 of capacity 6 kW. The temperature of the specimens is measured using three K-type thermocouples. The ends of the thermocouples are welded together to a junction. This junction is thereafter flattened to create a ribbon type thermocouple [19]. The three thermocouple loops are separated by approx. 3 mm and stretched to make contact with the specimen, using small springs. The middle thermocouple is used for temperature control. The heating rate is 10°C/s, followed by 5 seconds soaking time at the test temperature, prior to axial loading. Axial loading is performed using a constant strain rate of 0.136 s^{-1} (cross head speed of 3 mm/minute) until fracture. Tensile tests are performed at room temperature, 200°C, 300°C, 400°C and at 500°C. Three specimens are examined for all tests.

The nano-indentation creep measurements are performed on electro-polished steel specimens (see section 6.2.3) using an Agilent G200 nano-indenter equipped with a Berkovich-indenter. The tip is calibrated using a reference specimen of fused silica. We perform 20 indentation experiments on each specimen, according to constant load principles [20]. The maximum load, F_{max}, is 16 mN for all specimens. The load is selected to assure an indentation depth of minimum 150 nm, in order to measure macroscopic behaviour of the material [21]. The indenter is loaded up to F_{max} during 20 seconds. The maximum load is thereafter maintained for 600 seconds, while measuring the indentation depth. After the constant load section is finalized the load is decreased to $0.2F_{max}$ and maintained for 20 seconds to investigate thermal drift. The experiments are evaluated according to the method proposed by Goodall et al. [20].

Goodall et al. propose the parameter P, the tendency of a material to deform under constant load indentation for comparing creep behaviour of different materials at a given temperature. The parameter P is defined by:

$$P(t^*, \sigma) = \Delta h \left(\frac{dh}{dt}\right)_t, \qquad \textbf{Equation 6.1}$$

where Δh is the distance the indenter have penetrated into the material between the start of the constant load section and the evaluation time t^*, $(dh/dt)_t$ is the gradient of the depth-time curve at the evaluation time t^* and σ is the applied stress.

During indentation experiments the stresses in the metal, under the indenter, range from high in the vicinity of the indenter tip, to low values far from the indenter tip. Studies have shown that dislocation glide plasticity is the main mechanism for indentation creep due to the high stresses near the indenter tip. However, materials with small grain size may be dominated by Coble creep as well [18]. Since our investigated materials contain grains that are smaller 0.4 µm, we expect that diffusional creep may be involved.

Goodall et al. [20] suggest that different materials should be compared at the same time, t^*, and load, F_{max}, during indentation experiments. We therefore evaluate the parameter P for the three steels at $t^* = 570\ s$. However, since the three investigated steels have different hardness, the evaluation at $t^* = 570\ s$ will result in different indent depths. This will result in different contact pressures between the indenter and the steels, since all experiments are done at similar load. High contact pressures are expected to generate a higher degree of dislocation glide plasticity. We therefore also evaluate the parameter P for the three steels at the same depth; i.e. at the same σ but different t^*. Evaluation at similar depth allow us to compare the nano-indentation creep of the three steels at the same contact pressure, at similar sizes of the elastic/plastic hemisphere under the indenter and at the same distance from the indenter centre-line to the surface (diffusion paths are comparable and a similar free surface area is available for dislocation escape at the steel surface [22]). The evaluation at a similar depth is done at $\Delta h = 300 \mp 20\ nm$, since this indent depth is reached during the constant hold period, at a point where the depth-time curve has stabilized to a linear trend for all three steels.

6.2.2 Characterization of alloy carbides in KNDS4 and 34Cr4

The underlying microstructural mechanisms for the difference in mechanical properties of the three steels (see section 3.1) are examined by thermodynamic calculations and by measuring the size and composition of the alloy carbides in the microstructure of the steels after heat treatment using Atom Probe Tomography (APT).

Database TCFE06 is used for the thermodynamic calculations with the ThermoCalc software. We simulate the volume fractions of the stable phases in the three steels in the temperature range from room temperature up to 1350°C. The compositions of the stable phases are furthermore examined at the temperatures that are used during industrial heat treatment by APT observations after quenching of the specimens.

The specimens used for APT investigations are produced with an in-situ lift-out method [23] using the FEI Strata 235 DualBeal workstation. A wedge shaped strip (width 1 µm, maximum thickness 1 µm) is cut loose from the material surface and welded to a pre-sharpened silicon micro-tip using a Pt-rich gas. The specimen is sharpened by Ga+ sputtering using a pattern shaped as an annulus circle. APT is performed in an Imago LEAP 3000X HR atom probe tomography instrument. The analyses are performed using laser pulsing. The pulse frequency is set to 200 kHz, the laser energy to 0.25 nJ, the specimen temperature to 50 K and the evaporation rate to 0.5 %. The reconstruction and data evaluation is performed using the IVAS 3.6.1 software. The quantitative analysis is based on isotope distributions of different ions of relevant atom types [24]. The APT measurements are only performed for the KNDS4 and 34Cr4 steels, because the two conventional steels did not show a significant difference in mechanical behavior at elevated temperature (see section 6.3.1 and Fig. 6.1).

6.2.3 Optimization of the thermal processing of KNDS4

The investigation of different thermal processing of KNDS4 is performed on steel specimens that are machined to a cylindrical shape with a diameter of 4 mm and a length of 10 mm. The samples are heat treated in a Bähr 805 A/D dilatometer (Bähr-Thermoanayse GmbH, Hüllhorst Germany). We perform heat treatments at two different austenitization temperatures; 1) at 940°C to simulate industrial heat treatment equipment, which is limited to max. 940°C, and 2) at 1350°C to explore if it is possible to further improve the mechanical properties via optimal dissolution of alloying elements in order to maximize the volume fraction of alloy carbides during subsequent tempering. The soaking time of 30 minutes at 1350°C is chosen to compare the results to our earlier studies [16-17], in section 3.3. We note that ThermoCalc simulations show that a small volume fraction of $Ti_4C_2S_2$ phase can form in the temperature range of 1070°C to 1456°C. It may therefore not be possible to assure that all Ti-atoms are in solid solution. The KNDS4 steel that is quenched from 1350°C is from here on called KNDS4_1350 and the KNDS4 steel that is quenched from 940°C is called KNDS4_940. The austenitization treatment is followed by quenching to room temperature using He-gas, at a cooling rate of approx. 175-180°C/s from the start of quench to the martensite start (M_s) temperature and a cooling rate of approx. 45˚C/s below the M_s temperature. All specimens are subsequently isothermally tempered at 550°C for 5, 10, 30 or 60 minutes. The heating time to the isothermal tempering temperature is 138 s. The tempering temperature of 550°C is chosen because it correlates with industrial heat treatment of KNDS4 steel and in order to stay in line with our earlier investigations [16-17]. All heat-treated specimens are prepared by grinding and polishing to 1 µm diamond dispersion. Optical microscopy and Scanning electron microscopy SEM (JEOL JSM-6500F with a field emission gun) is performed on nital-etched (5%) surfaces. Electron back-scatter diffraction EBSD (using the SEM with a Nordlys detector) is performed on electro-polished surfaces, conducted in a solution of 8% perchloric, 10% butylcellosolve, 60% ethanol and 22% water. The EBSD data is acquired and post-processed with Channel 5 software. The beam diameter during EBSD mapping is approx. 16 nm, resulting in a spot dimension of 16 nm x35 nm. This spot dimension is combined with a step size of 100 nm. Conventional micro-Vickers hardness is measured at 20 locations using a load of 500 g.

6.3 Results and Discussion

6.3.1 Mechanical testing

Yield strength

The room temperature tensile strength and yield strength of industrially heat treated fasteners are shown in table 6.3.

Table 6. 3 *Tensile strength and yield strength of high strength fasteners at room temperature*

	33B2	**34Cr4**	**KNDS4**
R_m (MPa)	1094 ±12	1339±10	1504±16
Yield point (MPa)	989±4	1081±6	1267±17

Figure 6.1 shows the ratio of the yield strength at elevated temperature to the yield strength at room temperature of industrially heat treated 33B2, 34Cr4 and KNDS4 fastener steels as a function of test temperature after 5 seconds of soaking time and after 100 hours of soaking time. The yield strength reduces with increasing temperatures, for each of the three steels. However, the yield strength ratio at 500 °C is $\sigma/\sigma_0 \approx 0.65\pm0.06$ for the KNDS4 steel, which is much higher than the yield strength ratio at 500 °C of $\sigma/\sigma_0 \approx 0.40\pm0.04$ for the 34Cr4 and 33B2 steels.

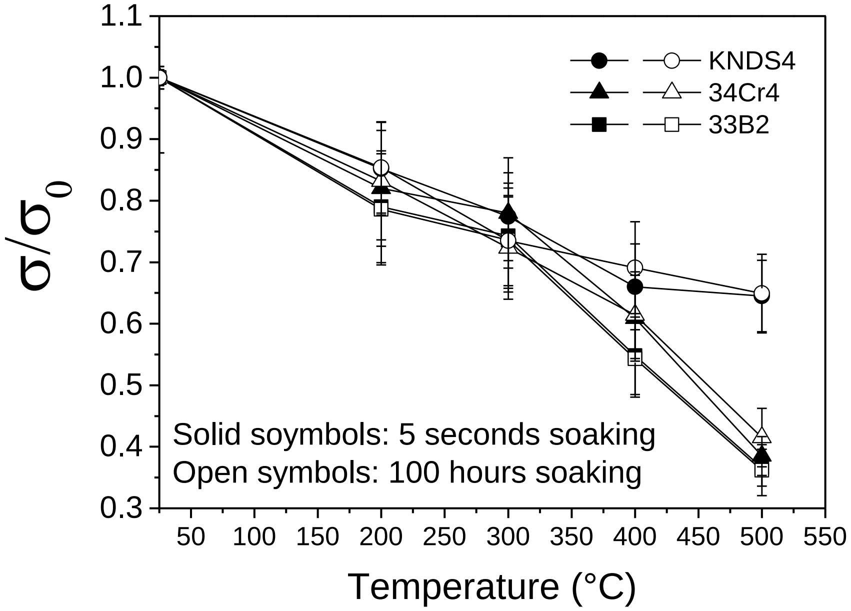

Figure 6.1 *Yield point strength ratio of industrially heat treated 33B2, 34Cr4 and KNDS4 steel as a function of test temperature after 5 seconds and 100 hours soaking time.*

Furthermore, the yield strength ratio of KNDS4 at 500°C is the same after 100 hours of soaking time as after 5 minutes of soaking time. The yield strength ratio of 34Cr4 and 33B2 is similar. The improved properties of the KNDS4 steel is believed to be a result of secondary alloy carbides, which form during the tempering of KNDS4. This is discussed in later sections.

Nano-indentation creep rate

Figure 6.2 shows the tendency of the metals to deform under constant load nano-indentation, P (Eq. 6.1), for fastener steels KNDS4, 34Cr4 and 33B2, as evaluated both at $t^* = 570\ s$ and at indent depth 300 ± 20 nm during nano-indentation creep testing.

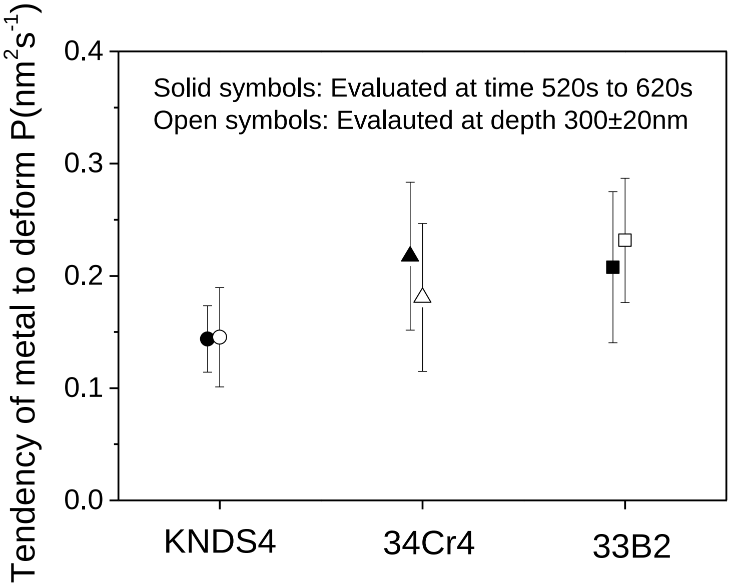

Figure 6.2, *Tendency of metal to deform under constant load nano-indentation for the three commercial steels KNDS4, 34Cr4 and 33B2, evaluated at the end of the constant load period (solid symbols) and at indent depth 300±20nm (open symbols).*

Figure 6.2 shows that at $t^* = 570\ s$ KNDS4 displays the smallest tendency to deform and 34Cr4 and 33B2 demonstrate similar values of P. Studies have suggested that harder materials creeps faster, since the indentation stress is higher [18]. The better performance of KNDS4 steel suggests that the microstructure of KNDS4 contains features which hinder dislocation glide plasticity.

Figure 6.2 furthermore shows that at similar depth, Δh=300 ± 20 nm the tendency to deform decreases with increasing tensile strength of the three steels; KNDS4 steel shows the smallest tendency to deform and steel 33B2 shows the highest tendency to deform. At similar indentation depth the contact stress is similar, and the driving force for dislocation glide plasticity in the three steels should be similar. We therefore expect that the resistance of the microstructure to dislocation glide plasticity in the three steels follow an inverse trend compared to parameter P; the microstructure of KNDS4 generates the highest resistance to dislocation glide plasticity and 33B2 the lowest. The better performance of the KNDS4 steel is believed to be a result of a higher density of small and stable alloy carbides in the KNDS4 steel as compared to the 34Cr4 and 33B2 steels. We emphasize that the parameter P does not represent fundamental creep characteristics, but is only used to compare the behavior of the three fastener materials to each other. Traditional axial creep testing is required in a subsequent study to fully establish the creep performance of KNDS4 in a subsequent study.

6.3.2 Characterization of the alloy carbides

ThermoCalc study

Figure 6.3 shows the stable alloy carbide phases in the KNDS4, 34Cr4 and 33B2 steels, as a function of temperature, in the temperature ranges of the tempering treatment. Phases with a mole of fraction less than 0.0005 are excluded from the pictures. The fractions of stable alloy carbide phases are significantly higher in the KNDS4 and 34Cr4 steel than in the 33B3 steel (note the scale) at the tempering temperature during the industrial heat treatment. The main equilibrium alloy carbides of KNDS4 steel are of M_7C_3-, TiC- and MC-type. The main equilibrium alloy carbide in steel 34Cr4 is of M_7C_3 type. The main alloy carbide type of 33B2 steel is of FCC-type consisting mainly of C, Ti and Cr.

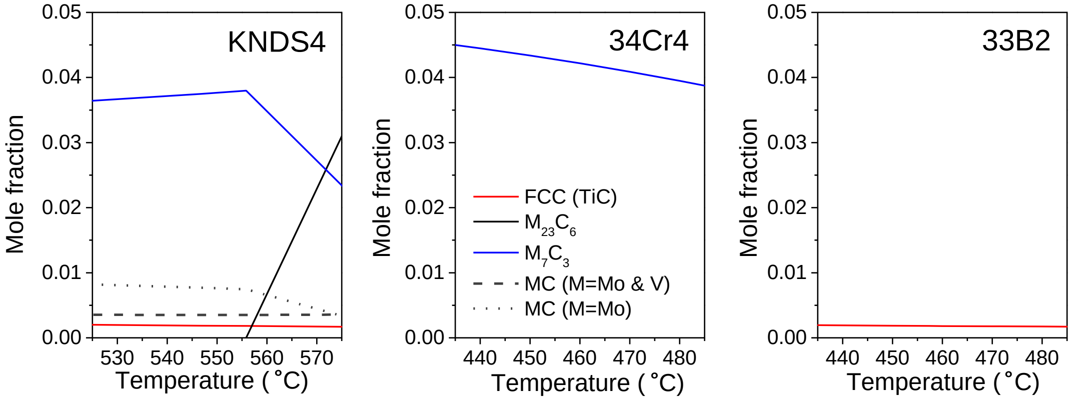

***Figure 6.3**, Stable alloy carbide phases in KNDS4, 34Cr4 and 33B2 steel as a function of temperature, in the temperature range surrounding the tempering temperature.*

The higher mole fractions of alloy carbides in KNDS4 and 34Cr4 can lead to increased precipitation strengthening. Small precipitates can pin dislocations and thereby prevent dislocation movement at both room temperature and elevated temperature. This can increase the yield strength ratio at elevated temperatures and reduce creep rates of KNDS4 and 34Cr4 steels. The ThermoCalc simulations furthermore show that the majority of Ti does not dissolve in the austenite of KNDS4 steel at 940°C, and we therefore expect that the formation of the TiC carbide in industrially heat treated KNDS4 is limited. Undissolved Ti is expected to be present as coarse primary TiC-carbides [25].

APT study of KNDS4 and 34Cr4

We exclude steel 33B2 from the APT study since ThermoCalc calculations show that the fraction of alloy carbide precipitates is very low in steel 33B2 and since the tensile-to-yield strength ratios of 34Cr4 and 33B2 are similar. Figure 6.4 shows APT images of industrially heat treated KNDS4 (a) and 34Cr4 (b) steel where carbon atoms are shown as red dots, cementite is shown as blue iso-concentration-surfaces and alloy carbides are shown as green iso-concentration-surfaces.

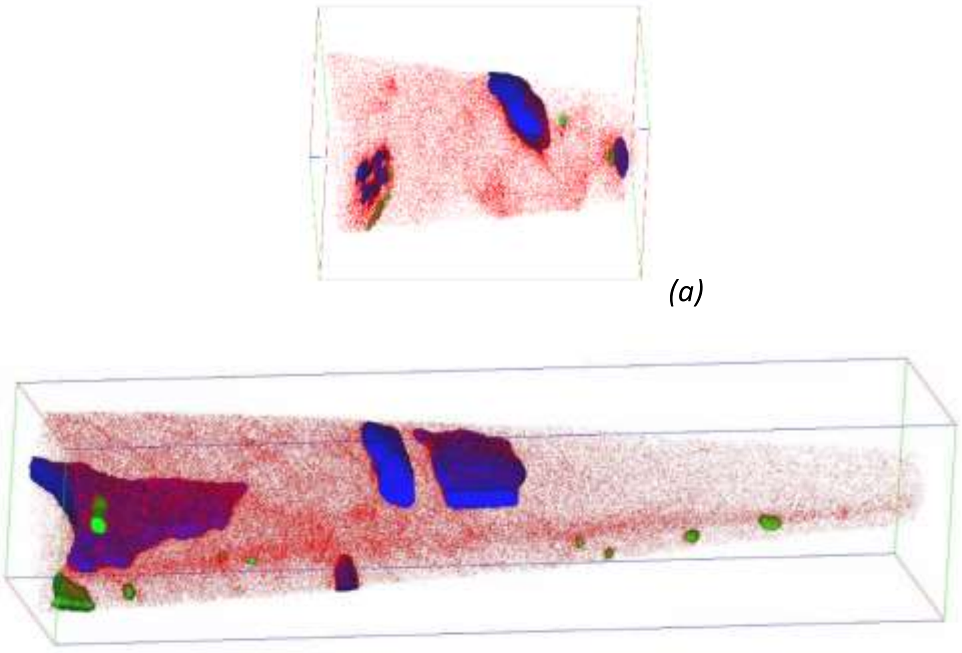

(a)

(b)

Figure 6.4 *APT images of as-quenched steels where carbon atoms are shown as red dots, cementite is shown as blue iso-surfaces and alloy carbides are shown as green iso-surfaces: (a) KNDS4, length 176 nm and (b) 34Cr4, length 469 nm.*

The cementite and alloy carbides are identified by the carbon concentration. The cementite and alloy carbides are thereafter separated by the Cr and Mn concentration. The atomic concentrations as measured by APT cannot be directly compared to the compositions as calculated by ThermoCalc since the overall detection rate of APT is 37% and since especially carbon atoms might not be detected due to surface migration of carbon atoms [26]. For small carbides the APT measurement will furthermore include some matrix atoms in the voxels that encapsulate the surface of the carbide. This is especially the case for small particles.

The measured concentration of carbon atoms in the matrix of KNDS4 and 34Cr4 is approx. 0.3 at% and the measured carbon concentration in cementite and alloy carbides exceeds 15 at%. The concentration of Cr and Mn in the cementite is measured to 1.7 at% and 1.3 at% in KNDS4 and 1.5 at% and 0.9 at% in 34Cr4.

The concentration of Cr and Mn in the alloy carbides is approx. 3 at% and 0.7-3.3 at% in KNS4 and 5% and 3% in 34Cr4. In 34Cr4 there are two large carbides which show a composition with 1.5 at% Mn and 2.2 at% Cr. These two carbides are believed to be alloy carbides based on that their carbon concentration is similar to the values measured in the smaller alloy carbides. None of the alloy carbides have a composition that correlates to a MC type of carbide. The alloy carbides in KNDS4 steel are therefore of M_7C_3, $M_{23}C_6$ or a mix of M_7C_3 and $M_{23}C_6$. According to ThermoCalc the concentration of Mn in M_7C_3 and $M_{23}C_6$ is 6.0 at% and 0.8 at% respectively. The range of measured Mn concentration in the alloy carbides of KNDS4 therefore indicates that the carbides are of M_7C_3 type and a mix of M_7C_3 and $M_{23}C_6$. The alloy carbides in 34Cr4 are identified to be of type M_7C_3.

The average number of atoms measured in the alloy carbides are 2000 atoms in KNDS4 and 39000 atoms in 34Cr4. We calculate the average sizes of the alloy carbides by assuming spherical shape and alloy carbides of M_7C_3 type. M_7C_3 carbides have an orthorhombic crystal structure with lattice parameters a =0.4526 nm, c =0.7010 nm and d =1.2142 nm and 40 atoms per unit cell [27]). We calculate that the average alloy carbide diameter is 3.3 nm in KNDS4 steel and 8.9 nm in 34Cr4.

The strengthening effect of the alloy carbides, $\Delta\sigma_P$ is thereafter calculated according to the Orowan-Ashby equation:

$$\Delta\sigma_P = \left(\frac{0.538 G b f^{1/2}}{d}\right) \cdot \ln\left(\frac{d}{2b}\right), \qquad \textbf{Equation 6.1}$$

where d is the average precipitate diameter, G is the shear modulus of the matrix (calculated to be 80.4 GPa by a linear interpolation between the systems of Fe and Fe-1C at as concentration of 0.4 wt.%C[17]), b is the length of the Burgers vector (0.248 nm [11]) and f is the volume fraction of precipitates. We use the ThermoCalc simulation values of mole fractions at the respective tempering temperature of KNDS4 and 34Cr4 as input for f. We thereafter convert the strength to hardness HV using $HV = \sigma_P/3$ [28].

The strengthening effect of the alloy carbides in KNDS4 contributes to 395 HV hardness and the alloy carbides in 34Cr4 contribute 238 HV hardness. We note that this calculation represent the strengthening effect of the equilibrium volume fraction of alloy carbides in the two steels, and therefore is an over-estimation. The calculation indicates that pinning of dislocations by alloy carbides is more efficient in KNDS4 steel, due to the size of the carbides. The better yield strength ratio of KNDS4 at elevated temperatures is therefore considered to be a result of the smaller alloy carbide precipitate size in KNDS4, as compared to 34Cr4. The small alloy carbide precipitates of KNDS4 will act to pin dislocations and prevent dislocation movement, which furthermore reduces the nano-indentation creep rate of KNDS4.

Table 6.4 shows the APT measurements of the concentration of alloy elements in the matrix (excluding cementite and alloy carbides) of KNDS4 and 34Cr4 steel, after heat treatment.

Table 6.4*, Alloy elements in the matrix (excluding cementite and alloy carbides) after heat treatment [wt%] determined by APT*

Steel	Mn	Cr	Mo	Ni	V
KNDS4	0.52	0.97	0.55	0.77	0.068
34Cr4	0.79	1.07	0.09	0.16	0.001

The APT measurements show that the concentration of alloy elements in the matrix of KNDS4 and 34Cr4 steel is similar to the overall composition of the steel, as given in table 6.1, after heat treatment. We therefore conclude that the redistribution of alloy atoms into both cementite and alloy carbides does not significantly affect the average composition of the matrix during tempering up to 60 minutes. After 60 minutes of tempering the martensite matrix is still supersaturated with alloying elements. Further growth, and possible nucleation, of alloy carbides is therefore likely to take place during prolonged tempering of both steels. No Ti-atoms were detected by APT in the KNDS4 specimen. ThermoCalc simulations show that at 940°C the mole fraction of stable TiC is 0.002 and that only $9 \cdot 10^{-6}$ wt% Ti is in solid solution. The lack of detected Ti atoms can be a result of the distribution of the stable, primary TiC carbides, and a concentration of Ti atoms in solid solution that is below the resolution of the APT detection level (37%).

6.3.3 Optimizing the thermal processing of KNDS4

We compare the microstructure and hardness evolution during tempering of KNDS4 after different austenization temperatures with the results of earlier investigations that we performed on a model alloy of Fe-C-Mn-Ti steel, which has similar concentrations of carbon and titanium [16-17]. This helps to unravel the microstructural mechanisms that lead to the hardness evolution during tempering of the KNDS4 steel.

Microscopy

The former austenite grain size is estimated from the length and orientation of the martensite structures, as revealed by nital etching on as-quenched specimens. The visible martensite arrays are measured using the line intercept method. The former austenite grain size of KNDS4_1350 is 750 ± 179 µm whereas the former austenite grain size of KNDS4_940 is 8 ± 1.5 µm (95% confidence interval). The smaller grain size KNDS4_940 is a result of stable TiC and MnS -phases which pin austenite grain boundaries during austenitization treatment at 940°C (calculated by ThermoCalc study). These phases are not present at 1350°C, which allow the austenite grains to grow rapidly in KNDS4_1350.

Figure 6.5 shows SEM images of a) KNDS4_1350, b) KNDS4_940 and c) Fe-C-Mn-Ti steel at low magnification in the as-quenched state and d) the average radius of the cementite particles of the three steels as a function of tempering time. The auto-tempered regions in the SEM images (Fig 10.5(a)-(c) appear as white regions due to the small iron carbides. We note from the SEM images that the degree of auto-tempering is higher in the KNDS4 steels than in Fe-C-Mn-Ti steel. The area fraction of auto-tempered regions is estimated to 80-90% in KNDS4 and 40-50% in Fe-C-Mn-Ti steel. The study of individual cementite particle sizes was performed at higher magnification SEM images presented in Figure 6.6

The average cementite radius, R, is calculated according to:

$$R = \sqrt{\left(\frac{w}{2}\right)\left(\frac{l}{2}\right)}, \qquad \textbf{Equation 6.2}$$

where *w* and *l* are the average width and length of cementite particles in the SEM images. The cementite particles grow rapidly during the first 5-10 minutes of annealing, and are thereafter stabilizing.

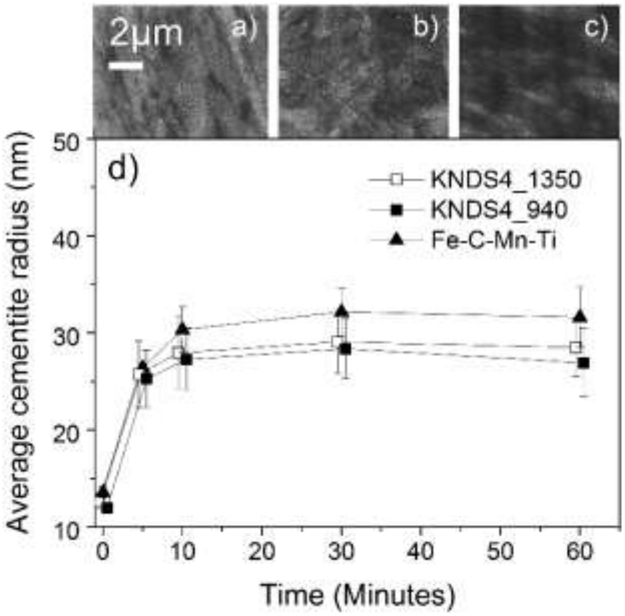

Figure 6.5 *SEM images of the as-quenched microstructure in a) KNDS4_1350, b) KNDS4_940 and c) Fe-C-Mn-Ti steel [16] and d) the average radius of the cementite particles of the three steels as a function of tempering time at 550°C.*

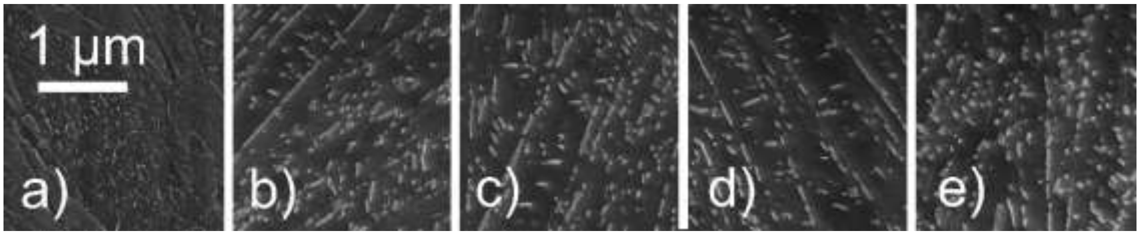

Figure 6.6 *SEM images of the cementite particles in KNDS4_1350 in a) the as-quenched state and b) after 5 minutes, c) after 10 minutes, d) after 30 minutes and e) after 60 minutes of tempering at 550°C.*

6.3.3.1 EBSD

We define the martensite block boundaries as boundaries between two neighboring pixels with a misorientation that exceeds 10˚ [29]. The average block size is measured from Inverse Pole Figure maps of the martensite. The average martensite block size after quenching is 4.1 µm^2 in KNDS4_1350 and 2.4 µm^2 in KNDS4_940. The spread in grain size is large in both KNDS4 steels. The largest and the smallest grain we measure in KNDS_1350 are 30.0 µm^2 and 0.1 µm^2 respectively and the largest and smallest grain we measure in KNDS4_940 and 19.6 µm^2 and 0.1 µm^2 respectively. We observe that no block coarsening takes place during tempering at 550°C by comparing the measured block size after 60 minutes of annealing, which is 4.4 µm^2 and 2.2 µm^2 for KNDS4_1350 and KNDS4_940, respectively.

If identification of the Kikuchi pattern during EBSD measurement is not possible, the measurement point cannot be indexed. Kikuchi patterns are typically degraded by surface roughness, grain boundaries, dislocations or precipitates which induce strain in the measured lattice [30]. In our earlier studies we showed that the regions adjacent to block boundaries in martensite cannot be indexed because these regions contain high dislocation densities. The EBSD results in the present study show that no block coarsening takes place in KNDS4_1350 and KNDS4_940 during tempering at 550°C. We therefore conclude that the relative changes in the number of non-indexed points during tempering are a result of changes in the strain level of the steel, e.g. via recovery of dislocations and nucleation of precipitates. Recovery leads to a reduction of non-indexed points whereas nucleation of precipitates leads to an increase of non-indexed points since precipitates are too small to be indexed (the beam spot size will cover both matrix and precipitate) and induce strains in the surrounding lattice. Small carbides will furthermore prevent recovery (by pinning of dislocations). We use the width of the non-indexed regions of the martensite block boundaries to study the evolution of strain in the martensite during tempering.

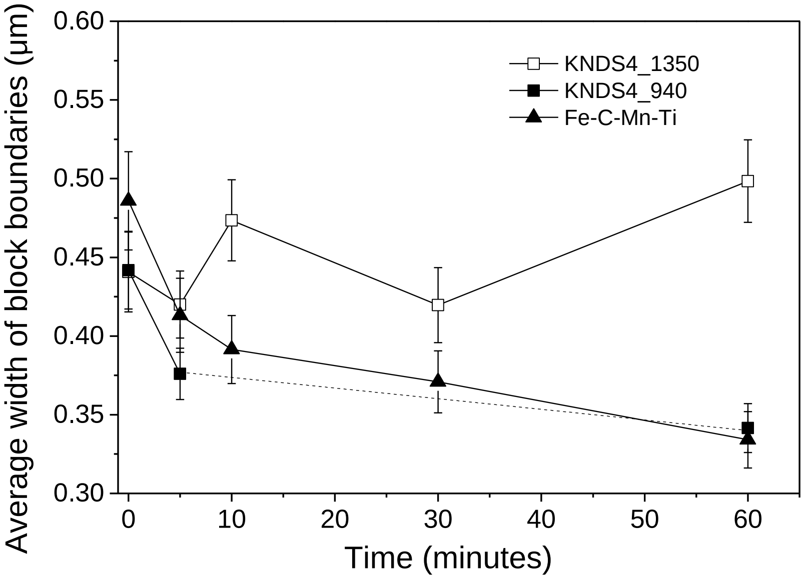

Figure 6.7 *Width of non-indexed martensite block boundaries in KNDS4_1350, KNDS4_940 and Fe-C-Mn-Ti steel [16] as a function of tempering time at 550°C.*

Figure 6.7 shows the average width of the non-indexed martensite block boundaries in the KNDS4_1350, KNDS4_940 and Fe-C-Mn-Ti steels, as a function of tempering time at

550°C. The width of the non-indexed block boundaries in the two KNDS4 steels is similar, and a little lower than the width of the non-indexed block boundaries in the Fe-C-Mn-Ti steel, in the as-quenched state.

During the first 5 minutes of tempering the width of the non-indexed regions decreases at a high rate in KNDS4_940 and Fe-C-Mn-Ti steel and with a slightly lower rate in KNDS4_1350. The rapid decrease of the non-indexed boundary width in Fe-C-Mn-Ti steel during the first 5 minutes of tempering was shown to be a result of recovery in the martensite in [16-17].

During tempering from 5 to 10 minutes the width of the non-indexed boundary regions continue to decrease in Fe-C-Mn-Ti, whereas KNDS4_1350 shows a significant increase of the non-indexed boundary width. The increase of non-indexed boundary width of KNDS4_1350 is a result of rapid nucleation and growth of precipitates. The earlier studies of Fe-C-Mn-Ti steel indicate that TiC-precipitate nucleation and growth takes place between 5 and 10 minutes. The increase of non-indexed points at the block boundaries of KNDS4_1350 steel therefore indicates that a higher density of precipitates nucleate and grow in KNDS4_1350, as compared to Fe-C-Mn-Ti steel. The data points for 10 minutes and 30 minutes are missing for KNDS4_940.

During tempering from 10 minutes to 30 minutes, the width of the non-indexed boundaries decreases slightly in KNDS4_1350 and Fe-C-Mn-Ti. The slight decrease indicates that recovery takes place parallel to nucleation and growth of alloy carbides.

During tempering from 30 minutes to 60 minutes the width of the non-indexed boundaries in KNDS4_1350 continues to increase again whereas the width of the non-indexed block boundaries continues to decrease in Fe-C-Mn-Ti. The increase observed for KNDS4_1350 indicates that ally carbide precipitates in KNDS4_1350 have grown into a size which induces strain in the lattice and distorts the Kikuchi pattern enough to prevent indexing. Since no increase of the width of the non-indexed block boundaries is observed in Fe-C-Mn-Ti we conclude that the alloy carbides in Fe-C-Mn-Ti are of smaller size and possibly have a lower number density.

Both Fe-C-Mn-Ti and KNDS4_940 show a decreasing width of non-indexed boundaries from 5 minutes of tempering to 60 minutes of tempering. The overall decrease of non-indexed block boundary width in KNDS4_940, from 5 minutes to 60 minutes, indicates that the density of alloy carbides that nucleate and grow during tempering is lower in KNDS4_940 than in KNDS4_1350.

Conventional MicroVickers

Figure 6.8 shows the hardness of KNDS4_1350, KNDS4_940 and Fe-C-Mn-Ti steel as a function of time during tempering at 550°C.

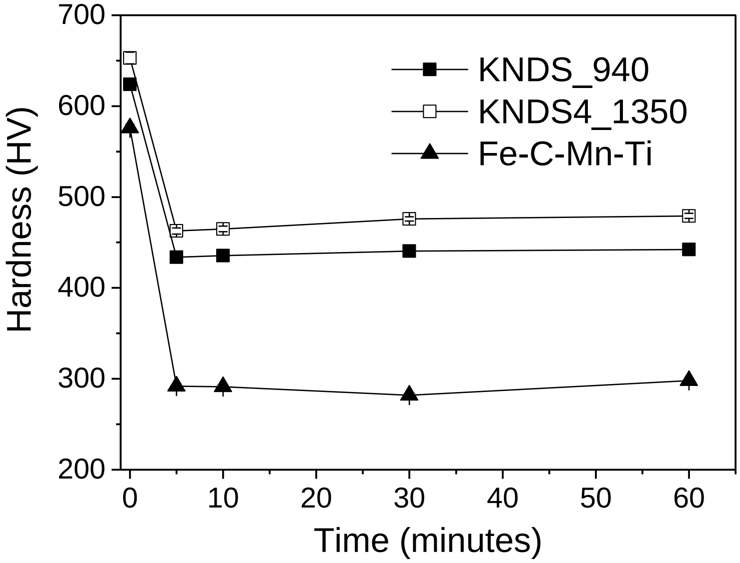

Figure 6.8, *MicroVickers hardness of KNDS4_1450, KNDS4_940 and Fe-C-Mn-Ti [16] steel, as a function of time during tempering at 550°C.*

KNDS4_1350 is harder than KNDS4_940, after all tempering times. The hardness difference is 29 HV in the as-quenched state and during the first 10 minutes of tempering. After 30 minutes of tempering the hardness difference increases to 35 HV and after increases to 37 HV after 60 minutes of tempering. This hardness difference can be caused by (i) different dislocation density, (ii) different concentrations of elements in solid solution, (iii) differences in grain boundary strengthening and/or (iv) different densities of small precipitates. We investigate the root cause to the hardness difference between KNDS4_1350 and KNDS4_940 in the as quenched state via a review of (i) to (iv).

The EBSD studies showed that the width of the non-indexed block boundary regions of the two KNDS4 steels is similar in the as-quenched state (Fig. 6.7). We therefore expect that the dislocation density is similar in the two steels.

We calculate the difference in the strengthening effect of elements in solid solution of KNDS4_1350 and KNDS4_940 in the as-quenched state using according to [31]:

$$\Delta\sigma_{ss} = \sum_i K_i c_i, \qquad \textbf{Equation 6.3}$$

where K_i is a constant for alloy element i, and c_i is the concentration of element i in weight percent. We assume that all elements which are in solid solution during austenitization treatment remain in solid solution in the as quenched state. The calculations can therefore lead to differences only for the elements that are present in stable phases at the respective austenitization temperature since both KNDS4 steels have the same overall composition. ThermoCalc simulations show that TiC-phase and MnS-phase are stable at 940°C and that $Ti_4C_2S_2$ is stable at 1350°C. The concentration of Ti atoms in solid solution of the austenite is $9 \cdot 10^{-6}$ wt% at 940°C and 0.03wt% at 1350°C and the concentration of Mn atoms in solid solution of the austenite at 940°C is 0.0044 wt%. ThermoCalc furthermore shows that the concentration of S-atoms is similar at 940°C and at 1350°C where S redistributes to MnS at 940°C and to $Ti_4C_2S_2$ at 1350°C. The calculation is therefore performed only for elements Ti and Mn. The concentration of Ti atoms in solid solution of the austenite is $9 \cdot 10^{-6}$wt% at 940°C and 0.03wt% at 1350°C and the concentration of Mn atoms in solid solution of the austenite at 940°C is 0.0044 wt%. We use K_{Mn}=35 MPa%$^{-1}$ [32] and K_{Ti}=1680 MPa^2%$^{-1}$ [17]. The calculated hardness difference of KNDS4_1350 and KNDS4_940, due to Mn and Ti is 22 HV, with KNDS4_1350 the harder microstructure.

We calculate the different strength contribution due to different block size of the martensite, σ_{gb}, in KNDS4_1350 and KNDS4_940 using the Hall-Petch equation [33]:

$$\sigma_{gb} = k_{gb} D^{-1/2}, \qquad \textbf{Equation 6.4}$$

where k_{gb} is the Hall-Petch factor and D the average diameter of the martensite blocks. We assume round block and use the average block diameter as measured by EBSD. We use $k_{gb} = 17.4\, MPa\, mm^{1/2}$ according to [11]. The strengthening effect of the martensite block is 138.7 HV in KNDS4_940 and 121.3 HV in KNDS4_1350. The hardness difference between KNDS4_1350 and KNDS4_940 is 17.4 HV, with KNDS4_940 the harder microstructure.

Taking (i), (ii) and (iii) into account, we expect that precipitates generate a hardness increase of 24.4 HV in KNDS4_1350, in order for our calculations to correlate with the measured hardness difference of 29 HV between KNDS4_1350 and KNDS4_940 in the as quenched state. There are several precipitate types which can generate precipitation strengthening in KNDS4_1350: M_7C_3- alloy carbides which form during quenching, $Ti_4C_2S_2$

which can form during the austenitization and possibly small iron carbides from auto-tempering.

According to Eq. 6.1, the smallest precipitate size (diameter) that can generate precipitation strengthening is 0.5 nm. The lattice parameters for M_7C_3 alloy carbides (see section 3.2) show that approx. 7 atoms are needed to form a M_7C_3 precipitate of diameter 0.5 nm. Nucleation of alloy carbides of the type M_7C_3 can therefore rapidly generate precipitation strengthening to the steel. In order to generate 24.4 HV, these small precipitates do however require a volume fraction close to 0.18 and we therefore consider precipitates which form during quenching an unlikely root cause to the measured hardness difference. ThermoCalc shows that $Ti_4C_2S_2$ is stable in austenite at temperatures higher than 1070 °C. It is therefore possible that $Ti_4C_2S_2$ nucleates as small precipitates during austenitization of KNDS4_1350. The equilibrium volume fraction of $Ti_4C_2S_2$ in KNDS4_1350 is $3.77 \cdot 10^{-4}$ at 1350°C. This volume fraction of precipitates in size 0.62 nm can generate a hardness increase of 25 HV. The hardness that difference different degrees of auto-tempering can generate in KNDS4_940 and KNDS4_1350, within the tolerance of the measured degree of auto-tempering with the area fraction of auto-tempering of 80% in KNDS4_1350 and 90% in KNDS4_1350 is 12.5 HV, for the average iron carbide precipitate size of 12.5 nm. We conclude that the hardness difference of 24.4 HV can be generated by a combination of different precipitate types in KNDS4_1350.

The increase of the hardness difference between KNDS4_1350 and KNDS4_940, from 29 HV in the as-quenched state, to 35 HV after 30 minutes of tempering confirm the EBSD result that a higher number density of precipitates nucleate and grow in KNDS4_1350 than in KNDS4_940, since no other hardening mechanism leads to increased strengthening in these two steels during tempering (no grain refinement is observed by EBSD, the number of dislocations does not increase and the APT study of section 3.2 confirmed that the concentration of alloy elements in the matrix of the martensite of KNDS4 is not increased during tempering.

Figure 6.8 furthermore shows that the hardness evolution of the two KNDS4 steels is similar during tempering at 550°C. The hardness decreases by 190 HV during the first 5 minutes of tempering and is thereafter showing an increasing trend. Earlier studies have shown that the hardness decrease of the Fe-C-Mn-Ti steel during the first 5 minutes of tempering at 550°C mainly originate from recovery (approx. 210 HV) and coarsening of Fe_3C (approx. 60 HV) [17].

We use Eq. 6.1 to calculate the strengthening effect of the cementite precipitates of KNDS4 steel, similar to [17]. The hardness contribution due to small cementite particles in the two KNDS4 steels is 191 HV in the as-quenched state. The hardness decrease due to coarsening of cementite during the first 5 minutes of tempering is thereafter calculated to 98 HV for both KNDS4 steels, since there is no significant difference in the cementite particles of the two KNDS4 steels (Fig. 5). The root cause for the high hardness decrease of KNDS4 steel is that KNDS4 contains a higher volume fraction of small iron carbides in the as-quenched state due to auto-tempering (the auto-tempered regions cover 40-50% of the area in Fe-C-Mn-Ti steel and 80-90% of the area in KNDS4 steel). The coarsening of the iron carbides during early stages of tempering therefore generates a large hardness loss in KNDS4.

The remaining 92.6 HV hardness decrease of KNDS4 steel during the first 5 minutes of tempering (from the total 190 HV measured hardness decrease) is generated by a reduction of the strengthening effect from a combination of solid solution, precipitates and dislocations (recovery). The combined effect of solid solution, precipitates and dislocations is complex. When new precipitates nucleate and grow, they can pin dislocations and reduce recovery. Formation of precipitates will furthermore redistribute alloy atoms from solid solution to the precipitates, which will result in a reduction of solid solution strengthening.

Dislocation strengthening in martensite can contribute to very high levels of hardness in the as quenched state (up to 274 HV) [17], whereas precipitation strengthening gives lower hardness contribution since the precipitates need to grow in size before they generate a hardness contribution. As precipitates nucleate and grow, alloying elements will be redistributed from solid solution to the precipitates. Our APT measurements of the matrix composition of the industrially heat treated KNDS4 steel (table 6.4) do however show that the concentration of the alloying elements appear to remain stable in the matrix during tempering. The unaccounted hardness loss of 92.6 HV is therefore expected to be a result of recovery only. Recovery reduces the number of non-indexed points in EBSD whereas carbide nucleation and growth can increase the number of non-indexed points. It is therefore possible that we do not observe any changes in number of non-indexed points during early stages of tempering of KNDS4.

We conclude that the strength and hardness of KNDS4 can be improved by applying a higher austentization temperature than the current industrial heat treatment. However, the higher temperature generates an austenite grain size which is more than 10 times higher than the one resulting from the industrial heat treatment, which can reduce the toughness of the KNDS4 steel [34] and is therefore not suitable for engine fasteners. We furthermore conclude that nucleation of complex alloy carbides in martensitic steel that contains several carbide forming elements is more rapid than nucleation of alloy carbides in a steel that contains only one carbide forming element. This observation is supported by literature studies which have shown that nucleation of vanadium and titan carbides in steel is promoted by Mo addition to the steel [35-37].

6.4 Conclusions

We compare the properties of the ultra-high tensile strength fastener steel KNDS4 and the conventional high strength fasteners steels 34Cr4 and 33B2 at room temperature and at elevated temperatures. We thereafter explain the difference in properties based on a study of the underlying microstructural mechanisms. Finally we perform a heat treatment study of KNDS4 steel to investigate if the microstructure and properties can be further improved.

KNDS4 steel has a higher yield strength ratio than both conventional high strength steels at 500°C, which have similar yield strength ratios at 500°C. Increased soaking time at elevated temperatures does not influence the yield strength ratio. The nano-indentation creep rate shows a weak trend in which the nano-indentation creep rate is lower as the strength of the different steel grades is higher; KNDS4 shows the lowest nano-indentation creep rate, followed by 34Cr4 and 33B2. The better mechanical properties of the KNDS4 steel are related to alloy carbides in the microstructure. The alloy carbides in KNDS4 are smaller than the alloy carbides in 34Cr4 steel, and the properties are therefore better. The heat treatment study of the KNDS4 steel shows that changing the standard industrial heat treatment to an austenitization temperature of 1350°C can increase the hardness of KNDS4 by 8%. The increase stems from a more effective dissolution of alloying elements during the austenitization treatment, which increases the volume fraction of alloy carbides that form during subsequent tempering and thereby pin dislocations and generate precipitation strengthening. However, the standard industrial heat-treatment results in smaller martensite block sizes, which might be more beneficial for the toughness of the steel. Independent of the heat treatment, we find that the mechanical performance of KNDS4 fasteners at elevated temperature and the low nano-indentation creep rates are two strong indicators that fasteners made from KNDS4 steel might be used at higher service temperatures than traditional high strength fasteners.

6.5 References

[1] Current production materials used within Nedschroef
[2] ISO898-1, Mechanical properties of fasteners made of carbon steel and alloy steel-Part 1. Fifth edition, Switzerland, 2013
[3] T. Seguchi, C. Hanai, O. Nakano and Y. Namimura: JSAE paper 20037061, 255-260
[4] Y. Namimura, N. Ibaraki, W. Urushihara and T. Nakayama: Wire J. Int., January(2003), 62-67
[5] S. Freeman and RWK Honeycombe: Metal Science., Feb (1977), 59-64
[6] T. Gladman: Mater. Sci. Tech., 15(1999), 30-36
[7] M. Charleux, WJ. Poole, M. Militzer and A. Deschamps: Metall. Mater. Trans. A., 32A(2001), 1635-1647
[8] CY. Chen, HW. Yen, FH. Kao, WC. Li, CY. Huang, JR. Yang and SH. Wang: Mater. Sci. Eng., 499(2009), 162-166
[9] S. Shanmugam, M. Tanniru, RDK. Misra, D. Panda and S. Jansto: Mater. Sci. Tech., 21(2005), 883-892
[10] L. Xu, J. Shi, WQ. Cao, MQ. Want, WJ. Hui and H. Dong: J. Mater. Sci., 46(2011), 3653-3658
[11] Y. Han, J. Shi, L. Xu, W.Q. Cao and H. Dong: Mater. Sci. Eng., A530(2011), 643-651
[12] RL. Klueh, N. Hashimoto and PJ. Maziasz: J. Nuclear Mater., 367-370(2007), 48-53
[13] K. Maruyama, K. Sawada and JI. Koike: ISIJ Int. 41(2001), 641-653
[14] M. Taneike, N. Fujitsuna and F. Abe: Mater. Sci. Tech., 20(2004), 1455-1461
[15] P. Michaud, D. Delagnes, P. Lamesle, MH. Masthon and C. Levaillant: Acta Mater., 55(2007), 4877-4889
[16] CEIC. Ohlund, J. Weidow, M. Thuvander and SE. Offerman: ISIJ Int., 54(2014), 2890-2899
[17] CEIC. Ohlund, D. den Ouden, J. Weidow, M. Thuvander and SE. Offerman: ISIJ Int., 55(2015), 883-892
[18] WB. Li, JL. Henshall, RM. Hopper and KE. Easterling: Acta Metall. Mater., 39(1991), 3099-3110
[19] S. Ghodrat: Thermo-Mechanical Fatigue of compacted graphite iron in diesel engine components, TU Delft, Delft, 2013
[20] R. Goodall and TW Clyne: Acta Mater., 54(2006), 5489-5499
[21] CEIC. Ohlund, SE. Offerman and E. Schlangen: Mater. Sci. Eng. A., 560(2013), 351-357
[22] L. Zhang, N. Sekido and T. Ohmura: Mater. Sci. Eng. A., 611(2014), 188-193
[23] DJ. Larson, DT. Foord, AK. Petford-Long, TC. Anthony, IM. Rozdilsky, A. Cerezo and GWD. Smith: Ultramicrosc., 75(1998), 147-159
[24] M. Thuvander, J. Weidow, J. Angseryd, LK. Falk, M. Sonestedt, K. Stiller and HO. Andre'n: Ultramicrosc., 111(2011), 604-608
[25] F-G. Wei, T. Hara, T. Tsuchida and K. Tsuzaki: ISIJ Int., 43(2003), 539-547

[26] B. Gault, F. Danoix, K. Hoummada, D. Mangelinck and H. Leitner: Ultramicroscopy., 113(2012), 182-191
[27] B. Xiao, JD. Xing, J. Feng, CT. Zhou, YF. Li, XJ. Xie and YH. Cheng: J. App.Phys., 42(2009), 5415
[28] B. Huthcinson, J. Hagstrom, O. Karlsson, D. Lindell, M. Tornberg, F. Lindberg and M. Thuvander: Acta Mater., 59(2011), 5845-5858.
[29] T. Ohmura, K. Tsuzaki and S. Matsuoka: Philos. Mag., A 82(2002), 1903–1910
[30] SI. Wright, MM. Nowell and DP. Field: Microsc. Microanal., 17(2011), 316–329
[31] T. Gladman: The physical metallurgy of microalloyed steels, The University press, London, 1997.
[32] LA. Nordstrom: Scand. J. Metall., 5(1976), 159-165
[33] LH. Friedman and DC. Chrzan: Phys. Rev. Lett., 81 (1998), 2715-2718
[34] C. Want, M. Wang, J. Shi, W. Hui and H. Dong: Scripta Mater., 58(2008), 492-495
[35] A. Vyrostakove, A. Kroupa, J. Janovec and M. Svoboda: Acta Mater., 46(1998), 31-38
[36] A. Vyrostakove, A. Kroupa, J. Janovec and M. Svoboda: Acta Mater., 46(1998), 39-41
[37] JH. Jang, YU. Heo, CH. Lee, HKDH. Bhadeshia and DW. Suh: Mater. Sci. Tech, 29(2013) 309-313

7 Conclusions

The trend of engine down-sizing of passenger cars has led to higher mechanical and thermal loading of the components inside the engine. This has driven a need for *stronger* and yet tough steels for engine fasteners, that can be used at *higher temperatures*.

New, ultra-high strength, fastener steels have already been developed, based on the need for higher strength and improved resistance to hydrogen embrittlement. The improvement in strength at room temperature of these fastener steels is achieved by creating a steel with a microstructure that consists of a tempered martensite matrix that is strengthened by the addition of small amounts of carbide-forming elements such as titanium (Ti), vanadium (V) and molybdenum (Mo). These elements react with carbon atoms to form nanometer-sized carbides, e.g. titanium carbide (TiC), vanadium carbide (VC), and molybdenum carbide (Mo_2C). Titanium is a particularly interesting micro-alloying element, because TiC-precipitates are also known to improve the resistance to hydrogen embrittlement of the steel. However, the novel, ultra-high strength steels for fasteners have not been designed for use at elevated temperatures.

From the literature, it is known that thermally stable carbides/precipitates are also known to improve the temperature or fire-resistance resistance of other steels that are used high-rise buildings and in power plants, by acting as pinning points for movement of dislocations. In theory, the ultra-high strength steels for fasteners could potentially also be processed in such a way that they could be used at higher temperatures than the current limit of 150°C.

In order to find out the optimal processing parameters, a deeper understanding of the effects of micro-alloying elements on the evolution of the microstructure and mechanical properties is needed during the tempering of martensitic steel. Tempering of martensite is a process in which the martensitic steel is heated to a temperature between 150 and 700°C for some time to make the initially hard and brittle steel tougher.

In this thesis high-purity, model alloys are investigated with and without the carbide-forming element Ti, to study the effect of Ti on the mechanisms underlying the microstructure and hardness evolution of martensitic steel during tempering. Thereafter, industrial fastener steels are studied, where the results from the model alloys are used to better understand the origins of the mechanical properties of the industrial steels at room and elevated temperatures.

The results from the research of the high purity model alloys led to the conclusions that the hardness of martensite block boundaries is significantly higher than the hardness inside the block matrix, due to a higher dislocation density in the regions adjacent to the block boundaries.

The softening kinetics during tempering of martensite that does not contain alloy carbides can be described by three stages, which are related to the evolution of the microstructure: Stage I (0-5 min) is characterized by fast macroscopic softening kinetics that is strongly related to: (a) fast and simultaneous softening and reduction in area fraction of boundaries regions that contain a high dislocation density and (b) fast reduction in area fraction of non-tempered matrix regions. Stage II (5-10 min) is characterized by slow macroscopic softening kinetics that is related to slow softening and reduction in area fraction of the boundaries regions that contain a high dislocation density. Stage III (10-60 min) is characterized by very slow softening kinetics that is related to very slow softening and reduction in area fraction of boundary regions.

An addition of 0.042 wt.% Ti to the model steel results in a slight hardness increase. The microstructure and hardness evolution during tempering at 300 °C remain similar as before the Ti-addition, but when tempering is done at 550°C the hardness starts to increase after 30 minutes of tempering. The hardness increase is related to the formation of TiC-precipitates at 550°C. Nucleation of TiC-precipitates starts in the regions close to the martensite block boundaries (between 5-10 minutes) and subsequently nucleates in the block matrix (between 10-30 minutes) due to the higher dislocation density in the regions close to the block boundaries. The formation of TiC-precipitates slows down the recovery in the regions close to the martensite block boundaries, especially between 5 and 10 minutes of annealing. Pipe diffusion of titanium atoms in the martensite contributes to the growth of the TiC-precipitates.

Simulations of the hardness evolution and the nucleation and growth of TiC precipitates in the model alloy show that the two microstructural components which contribute most to the overall hardness are Fe_3C precipitates (88 HV) and dislocations (54 HV). Both contributions decrease rapidly during the initial stages of annealing and stabilise after 10 minutes of annealing. The addition of titanium to the steel gives a minor hardness contribution via Ti-atoms in solid solution and TiC precipitates. Ti atoms in solid solution give a hardness contribution which increases slightly during the first few minutes of annealing and then remains stable (at 25 HV). The direct contribution of TiC precipitates to the overall hardness is limited (3.5 HV). However, TiC-precipitates also contribute to the overall hardness of martensite by pinning of dislocations during the recovery that takes place during the tempering. The model predicts that only a small volume fraction of TiC-precipitates forms during isothermal annealing at 550 °C due to the large misfit strain (1.34 GJ/m^3) and the low density of potential nucleation sites.

The alloy carbides which form in the ultra-high strength KNDS4 steel are smaller than the alloy carbides that form in the conventional high-strength 34Cr4 steel during industrial heat treatment. This could be due to the higher concentration of molybdenum, which is known to reduce the coarsening of TiC- and VC-precipitates, in the KNDS4 steel. KNDS4 steel has a higher ratio of the yield strength at elevated to the yield strength at room temperature than conventional fastener steels 33B2 and 34Cr4 at 500°C. Increasing the soaking time from 5 seconds up to 100 hours at elevated temperatures does not have an impact on the yield strength ratio, which suggest that the microstructure is at least stable 100h at elevated temperature (500°C). The nano-indentation creep rate shows a weak trend in which the tendency for deformation during constant load nano-indentation is lower in KNDS4 than in the 34Cr4 and 33B2 steels. This is measured both at similar indent depths and at the same indent time. The improved mechanical properties of the KNDS4 steel compared to the conventional high-strength steels are related alloy carbides in the microstructure that hinder dislocation movement. Changing the standard industrial heat-treatment of KNDS4 from an austenitization temperature of 940 to 1350°C can increase the hardness of KNDS4 by 8%. The increase stems from more effective dissolution of mainly Ti-atoms during the austenitization treatment. Titanium in solid solution enables the nucleation and growth of precipitates, which generates precipitation strengthening during subsequent tempering. However, the standard industrial heat-treatment results in a smaller martensite block sizes, which might be more beneficial for the toughness of the steel. Independent of the heat-treatment, we find that the mechanical performance of KNDS4 fasteners at elevated temperature and the low nano-indentation creep rates are two strong indicators that fasteners made from KNDS4 steel might be used at higher service temperatures than traditional high strength fasteners due to the presence of small alloy carbides in the microstructure of KNDS4. More research, in particular conventional creep measurements that are very time consuming, are needed to provide evidence that the ultra-high strength KNDS4 steel can be used at higher temperature in real engine conditions.

Higher strength of a fastener steel enables for development of smaller, but stronger fasteners. These fasteners can be used in critical applications inside the engine, to down-size e.g. connecting rods, which will make it possible to significantly reduce the size and weight of modern combustion engines. Furthermore, the improved temperature resistance of new martensitic fastener steels will allow using the fastener at elevated service temperatures. These fasteners can therefore be used in applications where the temperature exceeds the recommended service temperature of 150 °C (with the maximum upper boundary of 300°C) as stated in ISO898-1. This make is possible to reduce the use of highly alloyed high temperature fasteners (which are designed for service temperatures of 500°C or more) that are used in engines today due to the lack of cost efficient, resource-efficient, micro-alloyed fastener steels suitable for service at 300-500°C.

Acknowledgements

It's easy to do anything in victory. It's in defeat that a man reveals himself

-Floyd Patterson

The most important thing that I learned during the time of my study at TU Delft was to fail. And that failures leads to extraordinary good results, if you let them.

To realize this has changed me as an engineer, as an athlete and as a person. I am forever grateful to the persons who taught me this lesson.

First of all I want to thank my daily supervisor Erik Offerman and my promotor Jilt Sietsma for their supervision, support and encouragement. Your efforts have transformed me from an industrial engineer to a scientist! Thank you for allowing me the freedom to split my time between Helmond and Delft, and for letting me design the study. Thank you for always expecting a lot, and for setting high standards. I would like to especially thank Erik Offerman for his fantastic patience! You let me to do things “my way”, even though (in many cases) it meant that things were going to fail. I am too stubborn to learn things in any other way!

I also want to thank company Nedschroef, for trusting me with this study, and for investing in me!

I am forever grateful to all the persons who gave me fantastic support during my experimental work. Some of you really stood out in your efforts to help me! Thank you Kees Kwakernaak, for spending so many hours helping me with the SEM and EBSD studies. Without the flexibility you allowed me for scheduling the equipment I would never have been able to finish in time. I want to thank Nico Geerlofs, who supported and worked with me on the dilatometer! Without your support I would never have been able to prepare all my samples. And I want to thank Ton Riemslag, who took the time to teach me how to perform the hot tensile testing, despite a full agenda and a fully occupied laboratory.

I would also like to thank the team of persons who were performing experiments for my research. Thank you Erik Schlangen, for introducing me to the field of nano-indentation, for your great enthusiasm and for keeping up with my tight schedule. I also want to thank Mladena Lukovic, in the team of Erik Schlangen, for performing so many of the indentation experiments.

I want to thank the team at Chalmers University of Technology in Sweden, Mattias Thuvander and Jonathan Weidow, for their APT measurements. Thank you for your patience in explaining the reconstruction analyze for me in detail, despite my limited knowledge within this field.

At Nedschroef I want to thank Ferrie Kersten, who believed in me and fought to get the budget to realize this study. IT would not have happened otherwise. I also want to thank all my colleagues at the Techno Centre in Helmond; Rene, Lianne, Rob, Frank, Erik and Max. Thank you for your support and for covering for me during the days I spent in Delft.

I also want to acknowledge the persons who gave me the energy to keep up with my schedule and provided the places where I could recover my (exhausted) brain and let my unconscious work on all failed experiments and rejected papers. I know for sure that, without the heavy physical training I did during these years, I would not have been able to finalize neither my work, nor my studies.

Charles and Niels Verschuren, with family; I am forever grateful for your training and support. The cross-fit box in Gemert have always felt like a second home to me. You have coached and trained me in a way that made me reach overall targets and set personal records that I never ever imagined I was able to.

Frans Bosman; the work you do and the commitment you have, to keep the gym of the basement in Delft open at all times is truly fantastic! Thank you!

Finally I want to thank my husband, Bosko Pavlovic. Your support is *the* most important support I have! Thank you for enduring life with someone who spends most of the time at the office (or school), the free time at the gym, and most time in-between in her own head. I am finished with my studies now. Whatever my next challenge will be, I promise to do it *together* with you!!!

About the author

Carin Emmy Ingrid Christersdotter Öhlund was born on the 7th of February 1980 in Sundsvall (Alnö), Sweden.

She acquired her master's degree in Chemical Engineering with Engineering Physics at Chalmers University of Technology in Sweden on the 13th of January 2004. Her master's thesis was done at Volvo Materials Technology department, on the topic of aluminum fasteners in Magnesium components. She currently work for Koninklijke Nedschroef Holding B.V, at their production plant in Kunshan, China, in the position as Nedschroef Group R&D director.

2015-Present	**Group R&D Director (temporary located in Kunshan)** Koninklijke Nedschroef Holding B.V, Helmond, The Netherlands
2010-2015:	**PhD Researcher at Materials Science and Engineering Dept.** Delft University of Technology, Delft, The Netherland
2014-2015:	**Manager Techno Centre Kunshan** Nedschroef Techno Centre, Kunshan, China
2009-2014:	**Manager Materials Development** Nedschroef Techno Centre, Helmond, The Netherlands
2007-2009:	**Technical Support and Project Manager** Nedschroef Fasteners AB, Billdal, Sweden
2004-2007:	**Development Engineer for Engine Fasteners** Volvo Powertrain, Gothenburg, Sweden

List of publications

- *The kinetics of softening and microstructure evolution of martensite in Fe-C-Mn steel during tempering at 300°C.*
  C.E.I.C. Öhlund, E. Schlangen and S.E. Offerman
  Mater. Sci Eng A. Vol. 560, pp, 351-357, 2013

- *Effect of Ti on evolution of microstructure and hardness of martensitic Fe-C-Mn steel during tempering*
  C.E.I.C. Öhlund, J. Weidow, M. Thuvander and S.E. Offerman
  ISIJ Int., Vol. 54, pp 2890-2899, 2014

- *Modelling the evolution of multiple hardening mechanisms during tempering of Fe-C-Mn-Ti martensite*
  C.E.I.C. Öhlund, D. den Ouden, J. Weidow, M. Thuvander and S.E. Offerman
  ISIJ Int., Vol. 55, pp 883-892, 2015

- *A comparison between ultra-high-strength and conventional high-strength fastener steels: mechanical properties at elevated temperature and microstructural mechanisms*
  C.E.I.C. Öhlund, M. Lucovic, J. Weidow, M. Thuvander and S.E. Offerman
  (To be submitted)